Fluctuations in Spin-1 Bose-Einstein Condensates

Luke Michael Symes

a thesis submitted for the degree of

Master of Science

at the University of Otago, Dunedin,

New Zealand.

June 30, 2014

Abstract

Ultra-cold spinor Bose gases present rich physics due to the special combination of superfluidity and magnetism in a quantum system. This system was first realized in 1998 by confining a Bose-Einstein condensate in an all-optical trap.

In this thesis, we consider the fluctuations of observable quantities in a spin-1 Bose gas. Understanding how fluctuations arise due to the spin excitations of the condensate is important because it offers an insight into how measurement noise reveals the many-body physics of the system.

To begin, we present the mean-field and Bogoliubov theory of a uniform spin-1 Bose gas subject to a constant magnetic field, describing the condensate and its low-energy collective excitations.

We then develop a formalism to describe the fluctuations in a general density-like observable. We start from the two-point correlation function and cast it in the form of a generalised static structure factor determined by the three Bogoliubov quasiparticle excitation branches. We derive analytic results for the fluctuation amplitudes and the temperature-dependent static structure factors for observables of total density and the three spin densities.

For all four magnetic phases, we analyse the spinor order parameter and quasiparticle spectra while numerically mapping out the fluctuation amplitudes and static structure factors for the total and spin density operators.

We describe the fluctuations in experimental measurements made within finite cells, which is an important step to making meaningful predictions for experiments. We consider cylindrical cells and gaussian cells as two limiting cases. We apply this analysis to an experimentally realisable system of a quasi-2D spinor gas in a harmonic trap, comparing extensive numeric results with analytic limits.

Acknowledgements

I would like to thank Prof. Blair Blakie for being a wonderful supervisor. Thank you, Blair, for your enthusiasm, encouragement, and appreciation of all my coding efforts. I wholeheartedly enjoy our discussions. While at times it feels like I don't know very much, I'm glad to be further along the way than when I began.

I am grateful for getting to go to the FINESSE 2013 conference in Queenstown as a newbie to the field, and then travelling further afield (with slightly more knowledge) to VSSUP 2014 in Melbourne.

Many thanks to Dr. Danny Baillie for all your help with the gritty details of quantum mechanics, wrangling Mathematica & LaTeX, and bearing with my pro-Python agenda. Thank you to everyone in the cold-atom group, and to all my colleagues for being great people to work with and talk to.

To my family & friends, thank you for all your support & encouragement. You're the ones who've helped me get to where I am today. Thank you for being willing to listen to me rant and rave about (meta)physics every so often. I may stand upon the shoulders of giants, but you're the ones who help me keep my balance.

Contents

Contents

Chapter 1

Introduction

Ultra cold atoms have been an important proving ground for quantum mechanics for almost 20 years. Starting in 1924 from Satyendra Bose's serendipitous discovery of what we now call Bose statistics [1], combined with the theoretical star-power of Einstein [2], we fast forward to the landmark experiments of the mid-90s where the early theory was brought to life and confirmed with the first cases of Bose-Einstein condensates (BECs) using ^{87}Rb [3], ^{23}Na [4] and ^{7}Li [5].

Over the last 15 years, cooling techniques have been refined and ever-tighter control achieved in manipulating atomic samples with electromagnetic fields. The range of atomic species that have been condensed has widened greatly, including atoms with large magnetic moments like ^{52}Cr [6], ^{164}Dy [7], ^{162}Dy [8] and ^{168}Er [9], opening the field to the study of the dipolar BECs with long-range anisotropic dipole-dipole interactions. Meanwhile, advancements in trap design have opened the door to fully optical traps, liberating the hyperfine spin levels and allowing the realization of multi-component spinor condensates with ^{23}Na [10, 11], ^{87}Rb [12, 13] and ^{52}Cr [14]. In Table 1.1 we provide a review of the experimental timeline thus far in producing different BECs.

Spinor condensates offer a wide variety of rich physics, as testified by recent comprehensive reviews of the field [28, 29]. The multiple condensate components interact with each other through the spin-dependent interaction, while the presence of a magnetic field splits the hyperfine degeneracy. There is overlap with dipolar BECs since spinor species also have magnetic moments. Symmetry considerations become essential, as the spinor order parameter accesses spin-space symmetries, which in scalar condensates were completely locked away. This new landscape of interactions and symmetries

Year	Scalar BEC	Spinor BEC		
		$F = 1$	$F = 2$	$F = 3$
1995	^{23}Na [4], ^{87}Rb [3], ^{7}Li [5]			
1998	H [15]	^{23}Na [10]		
2000	^{85}Rb [16]			
2001	^{4}He [17], ^{41}K [18]	^{87}Rb [12]		
2003	^{133}Cs [19], ^{174}Yb [20]		^{23}Na [11]	
2004			^{87}Rb [13]	
2005	^{52}Cr [6]			
2007	^{39}K [21], ^{170}Yb [22]			
2008				^{52}Cr [14]
2009	^{40}Ca [23], ^{84}Sr [24, 25]			
2010	^{86}Sr [26], ^{88}Sr [27]			
2011	^{164}Dy [7]			
2012	^{168}Er [9], ^{162}Dy [8]			

Table 1.1: Experimental time-line of achieving Bose-condensation for scalar and spinor systems, with reference to the first experiments.

unfolds a veritable zoo of exotic spin textures, phase transitions, topological defects, and spin excitations.

This new toolbox of magnetism and superfluidity is realizable in highly controllable atomic systems, and has opened up the study of quantum properties of matter that had previously been locked away inside bulky condensed matter systems.

1.1 BECs

1.1.1 Background

All particles can be divided into two types: bosons and fermions. The distinguishing feature lies in a fundamental quantum property of particles, called "spin". Spin is essentially the intrinsic angular momentum of a particle, with the classical analogy being a particle spinning on its own axis. Quantum mechanically there is no spinning, just the spin quantum number, F, which sets allowed states with spin components $m_F = \{-F, -F + 1, \cdots, F\}$ that follow the algebra of angular momentum.

Bosons are particles with integer spin; fermions are particles with half-integer spin. They each display very different statistical behaviour. Fermions have many-body wavefunctions which are anti-symmetric which leads to them obeying the Pauli exclusion principle - two identical fermions cannot occupy the same single-particle state simultaneously. Bosons have symmetric many-body wavefunctions and can thus occupy the same single-particle state simultaneously. This property of bosons is what allows the formation of a BEC.

The energy states for a dilute gas can be thought of as a ladder leading from the ground state energy to higher and higher energies which become spaced closer and closer together. If one takes a dilute gas of bosonic atoms and cools them, they will fall down this ladder. As the gas gets very cold, the statistical distribution of energy changes from the classical hot-gas Boltzmann distribution into the Bose-Einstein distribution. At a temperature much higher than would be expected classically, Bose statistics makes it favourable for atoms to drop into the ground state. In a large cloud of atoms, this leads to macroscopic occupation of the ground state - a phase transition to a BEC driven by quantum statistics. The ideal BEC is a spatially coherent matter-wave where all atoms are in a single mode, with the many-body wavefunction a product state of these single-particle states. Below the critical temperature, a BEC can be described by a macroscopic order parameter.

1.1.2 Spinor BECs

A spinor BEC consists of atoms with a spin degree of freedom. Fig. 1.1 shows the hyperfine splitting for ^{23}Na and ^{87}Rb, as was shown in Refs. [30] and [31] respectively.
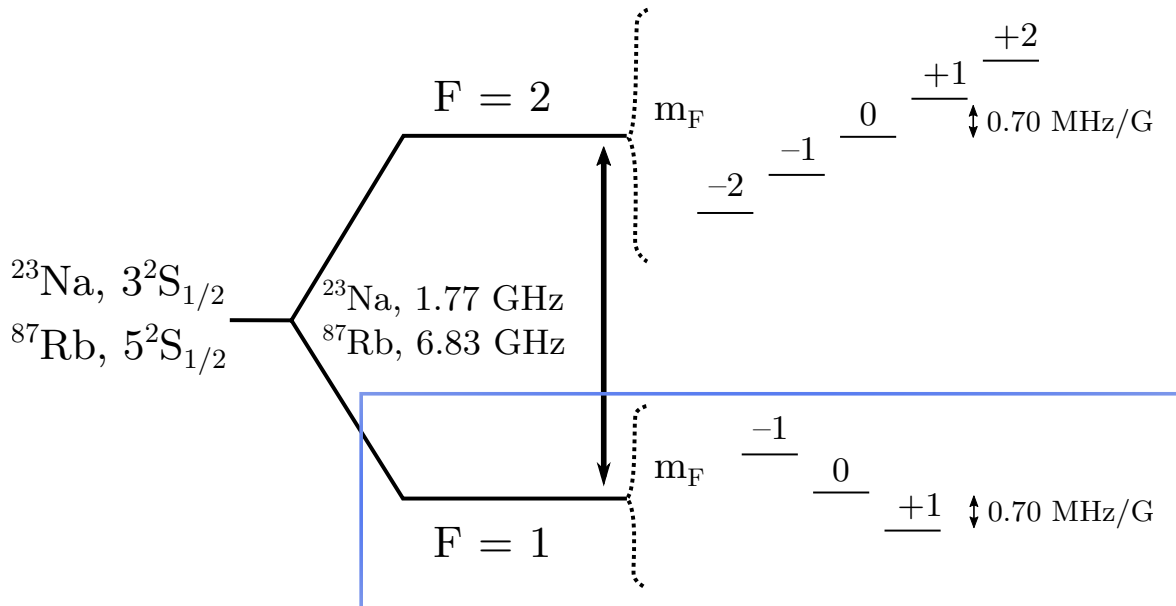
Figure 1.1: Hyperfine structure of ^{23}Na and ^{87}Rb ground states. In this thesis we focus on the $F = 1$ manifold with its three m_F sublevels.

The first spinor BEC to be realized experimentally was spin-1 ^{23}Na in 1998 [10], having been theoretically predicted by Ho, Ohmi and Machida [32, 33]. As detailed in Table 1.1, this was followed in subsequent years by BECs of spin-1 ^{87}Rb, spin-2 ^{23}Na and ^{87}Rb, and most recently by spin-3 ^{52}Cr.

In addition to exhibiting spatial coherence, a spinor condensate also displays a range of spin orders, determined by the interactions and externally applied magnetic field. Various aspects of the phase diagram and condensate dynamics have been explored in experiments, particularly for the case of spin-1 where the atoms can access three magnetic sublevels (e.g. see [34–42]). An important feature of this system is that it exhibits a rich excitation spectrum with phonon and magnon branches [28, 29, 32, 33]. Phonons are density excitations analogous to classical sound waves, and are ubiquitous in single-species scalar BECs. Magnons, however, are excitations of magnetization (i.e. spin). These so-called 'spin waves' are a distinguishing feature of multi-component BECs.

1.2 Spinor Fluctuations

The theory used to describe a BEC is mean-field theory. In this approach, we treat the Bose gas as if each atom experiences the average (mean) field of all the other atoms. When the system has macroscopic occupation of the ground state (i.e. a large number of atoms are condensate atoms), we can approximately describe the many-body system with an order parameter. At this level of theory, one can predict mean values of experimental measurements. In real experiments, each measurement follows the distribution of possible outcomes set by the full many-body wavefunction, which means that individual measurements display fluctuations, seen as 'noise' in experimental data. This noise might be seen as an impediment to confirming theoretical predictions, but it actually reveals useful information which is not captured by mean-field theory.

To make theoretical predictions which account for fluctuations, we need to consider the collective excitations about the condensate. These so-called 'quasiparticles' are the low energy excited states of the Bose gas above the ground state BEC. The theoretical framework that describes the collective excitations of the BEC is called Bogoliubov theory, and it provides a good description of a Bose gas for temperatures well below the condensation temperature.

For our fluctuation predictions to be relevant to experiments, we need to consider some practical details of making a measurement. In an experimental system, measurements are not point-like (i.e. with a definite position) but sample the volume contained by a finite cell. This is due to having finite imaging resolution: the smallest possible measurement cell is set by the point spread function of the imaging system and by the finite pixel size of the camera used to collect the light signal [43–45].

When making measurements with finite cells, position correlations (where neighbouring atoms are not independent) become important to consider, because typical cell sizes are comparable to the correlation lengths of the system (on the order of a few microns). To understand the correlations in the system, we introduce a two-point correlation function for an observable of interest. This function gives a measure of the independence of the fluctuations at two points in space. It is convenient for us to work with this correlation function in momentum space, so we take the Fourier transform and call this the static structure factor.

While the static structure factors are well characterised for the case of scalar condensates (e.g. see [46]), much less work has been done on multicomponent systems. There
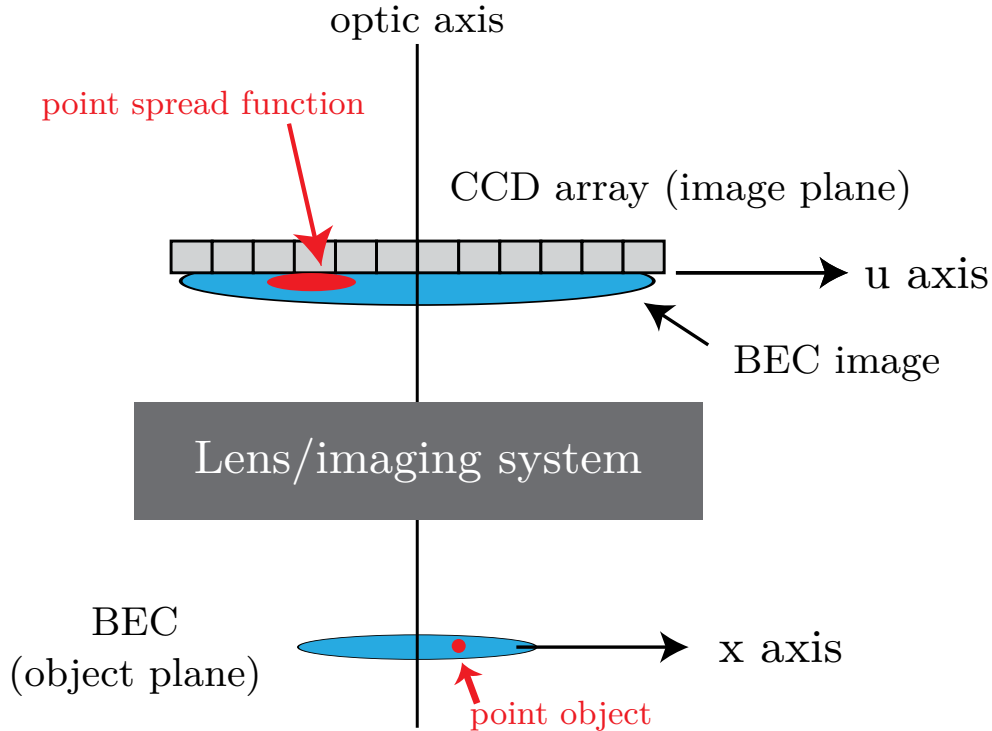
Figure 1.2: Here we show the experimental setup for imaging a BEC by shining light onto it in the object plane. A point source of resulting light intensity is transformed by the point spread function of the imaging system (lens etc.) to become a smeared out blob in the image plane. At the image plane, a CCD array collects light intensity within pixel cells. Measurements are thus of a finite volume of BEC in the image plane, having been spread out due to the imaging system and finite pixel resolution.

have been theoretical studies of binary condensates [47, 48], and a study of the finite-temperature transverse spin-density correlations in a quasi-2D ferromagnetic condensate (see Appendix B of Ref. [49]). Experimentally, several methods can determine the static structure directly, for example: fluctuation measurements (e.g. see [50, 51]), off-resonant light scattering [52] and Bragg spectroscopy [53, 54]. Notably, spin-dependent Bragg spectroscopy of a spin-$\frac{1}{2}$ Fermi gas was used to measure the z-spin density [55], and speckle imaging has been employed on a strongly interacting Fermi gas to measure the compressibility and magnetic susceptibility [56]. Along this path, a number of experiments with spin-1 condensates have made fluctuation measurements, particularly in application to dynamical regimes (e.g. [40, 57, 58]) and spin-squeezing [59]. We also note a recent proposal to probe the excitation spectrum of a spinor condensate using magnetic spectroscopy [60].

1.3 Our work

This is the first study of equilibrium fluctuations of a spinor BEC, and includes the important experimental consideration of finite imaging resolution. We develop a formalism that can be applied to describe the fluctuations of the total number density and the components of the spin density, motivated by the capability to measure these quantities directly in experiments (e.g. by Stern-Gerlach [58, 59, 61, 62] and dispersive [39, 42, 63–65] probing). We characterise these fluctuations by deriving generalized static structure factors, which arise from the collective excitation modes of the BEC and thus can be calculated using Bogoliubov theory.

We apply our general theory to the case of a non-dipolar spin-1 BEC in a uniform trap with a uniform magnetic field along z. For this system there are four distinct magnetic phases, and in each phase three Bogoliubov excitation branches contribute to the fluctuations. Of particular interest are the antiferromagnetic and broken-axisymmetric phases, in which a second continuous symmetry associated with the spin degree of freedom is broken [in addition to the $U(1)$ gauge symmetry]. This is revealed by the emergence of a second Nambu-Goldstone mode [66]. Nambu-Goldstone modes are gapless – their dispersion relation goes linearly to zero as the momentum goes to zero – and they act to restore spontaneously broken symmetries.

We apply our fluctuation formalism for the uniform spin-1 system to the experimentally realizable setup of a spin-1 BEC in a harmonic trap with a pancake geometry (tight in the z direction), and consider two limiting forms of the finite measurement cell: a disc-shaped cylindrical cell and a smooth Gaussian cell.

The analysis we undertake of the relationship between the quasiparticle excitations and the fluctuations in experimental measurements provides an exciting insight into the decidedly quantum nature of the spin-1 BEC and how it can be revealed through noise measurements.

1.4 Thesis Outline

This thesis is structured as follows. In Chapter 2, we review the mean-field theoretical framework of the spin-1 BEC, which gives rise to the condensate spinor and four magnetic ground state phases. In Chapter 3, we take the condensate spinor and analyse the

collective excitations about the ground state using Bogoliubov theory. From here, in Chapter 4 we develop a formalism which can describe fluctuations of any observable, which results in a generalized static structure factor. In Chapter 5 we apply this formalism to the total and spin density operators, and map out the excitation modes that contribute to fluctuations in their mean value. In Chapter 6, we apply our general fluctuation theory to a hypothetical experimental setup where fluctuations are measured within finite cells. After developing the further theory needed to describe this situation, we apply our knowledge to numerically calculate fluctuations and analytically calculate limiting expressions. This gives us theoretical predictions for experimentally realizable fluctuation measurements. Finally, we conclude in Chapter 7 by discussing the implications of our results.

1.5 Papers arising

The work in Chapters 4 and 5 has been published in Phys. Rev. A, Ref. [67]. The work in Chapter 6 has been accepted for publication in Phys. Rev. A, and is available on the arXiv, Ref. [68].

Chapter 2

Spin-1 Mean-Field Theory

In this chapter, we review the mean-field theory of a spin-1 condensate. First, we introduce the Hamiltonian that describes the cold-atom spinor gas. Then, taking a mean-field approach, we assume that we have a BEC and separate out the condensate spinor from the field operator. We explain how to calculate this spinor, before detailing the ground state phase diagram as a function of the spin-dependent interaction and magnetic field interactions. Finally, we conclude by detailing the spherical-harmonic representation and the nematic spin order, which reveal the symmetry properties of the spinor.

2.1 Hamiltonian

Here we consider a uniform three-dimensional spin-1 Bose gas subject to a uniform magnetic field along z. We assume that we are in a temperature regime where the only relevant atomic collisions are s-wave scattering. We also ignore the effects of the dipole-dipole interaction by considering species where the magnetic dipole moment is negligible compared to the other interaction energies.

The single particle description of the atoms is provided by the Hamiltonian

$$(h_0)_{ij} = \left[-\frac{\hbar^2 \nabla^2}{2M} - pi + qi^2 \right] \delta_{ij}, \tag{2.1}$$

where p and q are the coefficients of the linear [1] and quadratic Zeeman terms, re-

---

[1] The quantity p also serves as a Lagrange multiplier to constrain the z-component of magnetization.

spectively, and the subscripts $i, j = \{-, 0, +\}$ refer to the $m_F = \{-1, 0, 1\}$ magnetic sub-levels of the atoms. The value of q is tunable independently of p using AC electric fields, e.g. see Refs. [69, 70], and can be both positive and negative. The linear and quadratic Zeeman terms arising from a uniform magnetic field for ^{87}Rb are shown in Fig. 2.1.
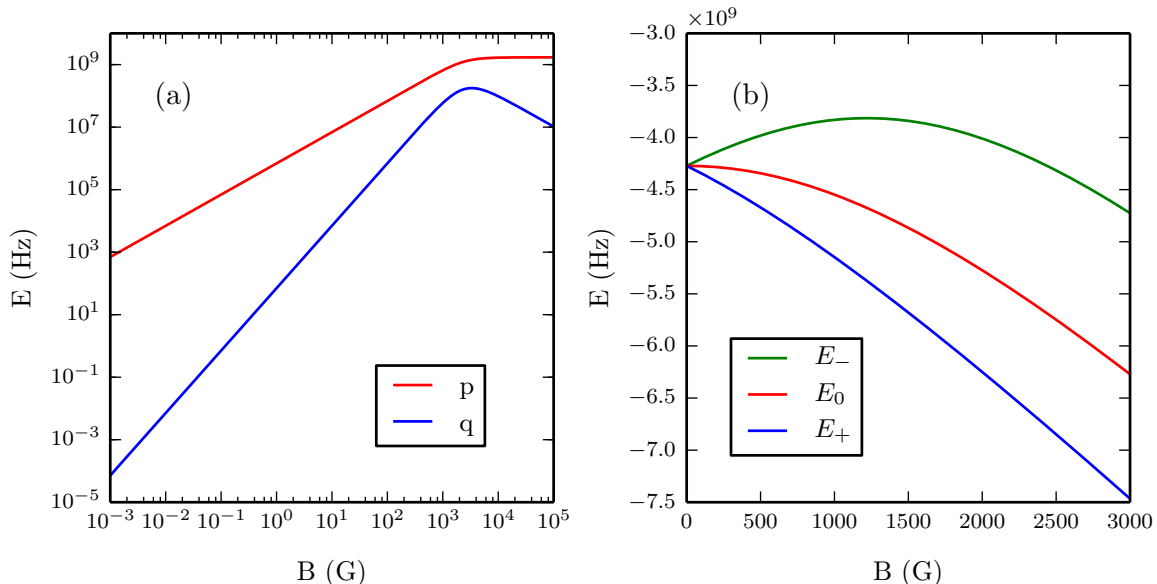

Figure 2.1: The Zeeman terms and $F = 1$ hyperfine splitting for ^{87}Rb in a uniform magnetic field B. The linear and quadratic terms are p and q respectively, and are shown in (a). They parameterize the shifts of the individual m_F levels shown in (b).

The cold-atom Hamiltonian, including interactions, is given by [32, 33]

$$\hat{H} = \int d\mathbf{x} \left[\hat{\boldsymbol{\psi}}^\dagger(\mathbf{x}) h_0 \hat{\boldsymbol{\psi}}(\mathbf{x}) + \frac{c_0}{2} : \hat{n}(\mathbf{x})\hat{n}(\mathbf{x}) : + \frac{c_1}{2} : \hat{\mathbf{f}}(\mathbf{x}) \cdot \hat{\mathbf{f}}(\mathbf{x}) : \right], \tag{2.2}$$

where :: indicates normal ordering, $\hat{\boldsymbol{\psi}} = [\hat{\psi}_+, \hat{\psi}_0, \hat{\psi}_-]^T$ is the spinor boson field operator, and the superscript T indicates the transpose operation. The interaction terms involve the total density $\hat{n}$ and the spin density $\hat{\mathbf{f}} = [\hat{f}_x, \hat{f}_y, \hat{f}_z]^T$ given by

$$\hat{n}(\mathbf{x}) = \hat{\boldsymbol{\psi}}^\dagger(\mathbf{x})\hat{\boldsymbol{\psi}}(\mathbf{x}), \tag{2.3}$$

$$\hat{f}_\alpha(\mathbf{x}) = \hat{\boldsymbol{\psi}}^\dagger(\mathbf{x})F_\alpha\hat{\boldsymbol{\psi}}(\mathbf{x}), \quad \alpha \in \{x, y, z\} \tag{2.4}$$

where $\{F_\alpha\}$ are the spin-1 matrices,

$$F_x = \frac{1}{\sqrt{2}} \begin{pmatrix} 0 & 1 & 0 \\ 1 & 0 & 1 \\ 0 & 1 & 0 \end{pmatrix}, \quad F_y = \frac{i}{\sqrt{2}} \begin{pmatrix} 0 & -1 & 0 \\ 1 & 0 & -1 \\ 0 & 1 & 0 \end{pmatrix}, \quad F_z = \begin{pmatrix} 1 & 0 & 0 \\ 0 & 0 & 0 \\ 0 & 0 & -1 \end{pmatrix}. \tag{2.5}$$

It is important to note that this Hamiltonian is number conserving and axially symmetric (along z) in spin space [71], i.e.

$$[\hat{H}, \hat{N}] = 0, \tag{2.6}$$

$$[\hat{H}, \hat{F}_z] = 0, \tag{2.7}$$

where the total number and z-magnetization operators are respectively defined as

$$\hat{N} \equiv \int d\mathbf{x} \, \hat{n}(\mathbf{x}), \tag{2.8}$$

$$\hat{F}_z \equiv \int d\mathbf{x} \, \hat{f}_z(\mathbf{x}). \tag{2.9}$$

The parameters c_0 and c_1 are the density and spin dependent interaction parameters, respectively, and are given by

$$c_0 = \frac{4\pi\hbar^2}{3M}(a_0 + 2a_2), \tag{2.10}$$

$$c_1 = \frac{4\pi\hbar^2}{3M}(a_2 - a_0), \tag{2.11}$$

with a_S ($S \in \{0, 2\}$) being the s-wave scattering length for the scattering channel of total spin S. We introduce the spin healing length

$$\xi_s \equiv \frac{\hbar}{\sqrt{M|c_1|n}}, \tag{2.12}$$

as a convenient length scale, in analogy to the density healing length,

$$\xi_n \equiv \frac{\hbar}{\sqrt{Mc_0n}}. \tag{2.13}$$

The healing lengths characterize the sizes of spatial structures comparable to the relevant interaction energy, e.g. $\hbar^2/M\xi_s^2 = |c_1|n$.

With reference to the Hamiltonian (2.2), we see that the sign of the spin-dependent interaction affects the magnetization of the ground state. For $c_1 > 0$, magnetization is energetically unfavourable, so the global ground state favours having $|\hat{\mathbf{f}}| \to 0$. We refer to this case as having *antiferromagnetic* interactions, and an experimental species that realizes it is ^{23}Na. Conversely, when $c_1 < 0$, magnetization reduces energy and the global ground state favours maximizing $|\hat{\mathbf{f}}|$. In this case, we describe this system as having *ferromagnetic* interactions, and it can be realized experimentally with ^{87}Rb.

In Table 2.1, we show current best estimates of c_0, c_1, and their ratio for antiferromagnetic ^{23}Na and ferromagnetic ^{87}Rb. These estimates are based on experimental

measurements of the scattering lengths a_2, a_0, and their difference $a_2 - a_0$. For our numerical work, we are interested in the ratio $c_0/|c_1|$, and for these two species the current experimental measurements have very large uncertainties. We note that the spin dependent interaction is difficult to measure due to being so much smaller than the spin independent interaction. This can be seen in that experiments which measure a_2 and a_0 separately are not fully in agreement with all experiments that measure $a_2 - a_0$ directly (see Table 2 of Ref. [28] for details).

Species	$\bar{c}_0$ (a.u.)	$\bar{c}_1$ (a.u.)	$c_0/|c_1|$
^{23}Na	153.32 ± 1.60	3.0 ± 1.8	51.4 ± 31.0
^{87}Rb	302.60 ± 0.30	-1.3 ± 0.4	240.2 ± 78.4

Table 2.1: Average experimental values of interaction parameters $\bar{c}_{0,1} \equiv c_{0,1} \times 3M/(4\pi\hbar^2)$ in units of the Bohr radius ($a_B = 0.0529$ nm), along with their ratio $c_0/|c_1|$, for ^{23}Na and ^{87}Rb, computed from experimental data listed in Table 2 of Ref. [28].

2.2   Mean-field description

Here we shall be interested in temperatures well below the condensation temperature where the field can be written as

$$\hat{\boldsymbol{\psi}}(\mathbf{x}) = \sqrt{n}\,\boldsymbol{\xi} + \hat{\boldsymbol{\delta}}(\mathbf{x}), \qquad (2.14)$$

where $\langle \hat{\boldsymbol{\psi}} \rangle = \sqrt{n}\,\boldsymbol{\xi}$ is the (uniform) mean-field that describes the condensate, $n = N/V$ is the condensate density, V is the volume, N is the number of condensate atoms, and $\boldsymbol{\xi} = [\xi_+, \xi_0, \xi_-]^T$ is the normalized condensate spinor. The operator $\hat{\boldsymbol{\delta}} = [\hat{\delta}_+, \hat{\delta}_0, \hat{\delta}_-]^T$ represents the non-condensate field, with expectation $\langle \hat{\boldsymbol{\delta}} \rangle = \mathbf{0}$.

2.2.1   Condensate

The condensate is obtained as the lowest energy solution of the time-independent Gross-Pitaevskii equation (GPE)

$$\mu\boldsymbol{\xi} = \left[h_0 + c_0 n \mathbb{1} + c_1 \sum_\alpha f_\alpha \mathrm{F}_\alpha\right] \boldsymbol{\xi}, \qquad (2.15)$$

where $\mathbb{1}$ is the 3×3 identity matrix and

$$f_\alpha = n\boldsymbol{\xi}^\dagger \mathrm{F}_\alpha \boldsymbol{\xi}, \tag{2.16}$$

is the α-component of the condensate spin density. We can write the matrix equation as three coupled GPEs in the form

$$\mu\xi_+ = \left[-\frac{\hbar^2\nabla^2}{2M} + (c_0 + c_1)n - p + q\right]\xi_+ + c_1(\xi_0^2 - 2\xi_+\xi_-)\xi_-^*, \tag{2.17}$$

$$\mu\,\xi_0 = \left[-\frac{\hbar^2\nabla^2}{2M} + (c_0 + c_1)n\right]\xi_0 - c_1(\xi_0^2 - 2\xi_+\xi_-)\xi_0^*, \tag{2.18}$$

$$\mu\xi_- = \left[-\frac{\hbar^2\nabla^2}{2M} + (c_0 + c_1)n + p + q\right]\xi_- + c_1(\xi_0^2 - 2\xi_+\xi_-)\xi_+^*. \tag{2.19}$$

2.2.2 Using a real spinor

In general, the condensate spinor has three complex components, giving six variables to solve for in Eq. (2.15). Using the fact that the spinor is equivalent under a global phase rotation $e^{-i\theta}$ and an arbitrary spin rotation around the z-axis $e^{-i\mathrm{F}_z\alpha}$ [see Eqs. (2.7) and 2.6)], we can rotate any complex spinor to a real one, reducing six coupled simultaneous equations down to three. To see this, write the general spinor in terms of real magnitudes and arbitrary phases as

$$\boldsymbol{\xi} = [|\xi_+|e^{i\theta_+}, |\xi_0|e^{i\theta_0}, |\xi_-|e^{i\theta_-}]^T. \tag{2.20}$$

When substituted into the energy functional $\langle\hat{H}\rangle$, only one phase-dependent term arises (from within the spin-dependent term):

$$2c_1n|\xi_0|^2|\xi_+||\xi_-|\cos\Delta, \tag{2.21}$$

where

$$\Delta \equiv \theta_+ + \theta_- - 2\theta_0. \tag{2.22}$$

To minimize energy, the ground state must have $\Delta = 0$ for $c_1 < 0$ and $\Delta = \pi$ for $c_1 > 0$. As summarized in Table 2.2, we can thus always rotate to a real spinor.

Parameters	θ_0	Transformation	Rotated Form
$c_1 < 0, \boldsymbol{\xi}$	$(\theta_+ + \theta_-)/2$	$e^{-i(\theta_+ + \theta_-)/2} e^{-iF_z(\theta_+ - \theta_-)/2}$	$[|\xi_+|, |\xi_0|, |\xi_-|]^T$
$c_1 > 0, \boldsymbol{\xi}$	$(\theta_+ + \theta_- - \pi)/2$	$e^{-i(\theta_+ + \theta_- - \pi)/2} e^{-iF_z(\theta_+ - \theta_- + \pi)/2}$	$[|\xi_+|, |\xi_0|, -|\xi_-|]^T$
$c_1 > 0, \boldsymbol{\xi}'$	-	$e^{-i(\theta_+ + \theta_-)/2} e^{-iF_z(\theta_+ - \theta_-)/2}$	$[|\xi_+|, 0, |\xi_-|]^T$

Table 2.2: Rotating arbitrary spinors to real spinors, where we have introduced the special case of $\boldsymbol{\xi}' \equiv [|\xi_+|e^{i\theta_+}, 0, |\xi_-|e^{i\theta_-}]^T$. For spinors with the m-th spin component fully occupied, just a global phase rotation $e^{-i\theta_m}$ is required.

2.2.3 Phase diagram

A variety of ground state phases emerge from the competition between the spin-dependent interaction (i.e. $c_1 n$) and the external magnetic field (i.e. p and q). For spin-1 there are four distinct phases distinguished by their magnetization, both the component of magnetization along the direction of the external field (f_z), and the component perpendicular to it,

$$f_\perp \equiv \sqrt{f_x^2 + f_y^2}. \tag{2.23}$$

The ground state order parameter is found by first finding the stationary solutions of the GPE, and from these the stable ground state solution is determined by which has the lowest energy. These properties are summarized in Table 2.3, and the parameter regions where each phase is the predicted ground state is shown in Fig. 2.2.

We note that in the AF and BA phases, the magnetization varies continuously. For AF, $0 \leq |f_z| < n$. In BA, the spinor is rotated away from the z-axis to develop $f_\perp > 0$. Rotating the spinor by an angle of $\pi/2$ into the $x - y$ plane puts the system along the $p = 0$ line. Here, the magnetization is

$$f_\perp = n\sqrt{1 - \tilde{q}^2}, \tag{2.24}$$

where we have defined

$$\tilde{q} \equiv \frac{q}{2|c_1|n} = \sqrt{1 - (f_\perp/n)^2}. \tag{2.25}$$

This shows that, along $p = 0$, the BA phase has $0 < f_x < n$. We define an analagous quantity to $\tilde{q}$ for the AF phase,

$$\alpha_z \equiv \sqrt{1 - (f_z/n)^2}. \tag{2.26}$$

The detailed derivation of the ground states and the phase diagram is too lengthy to present here, and we refer the reader to the excellent summary given in Sec. 3.3 of Ref. [28].
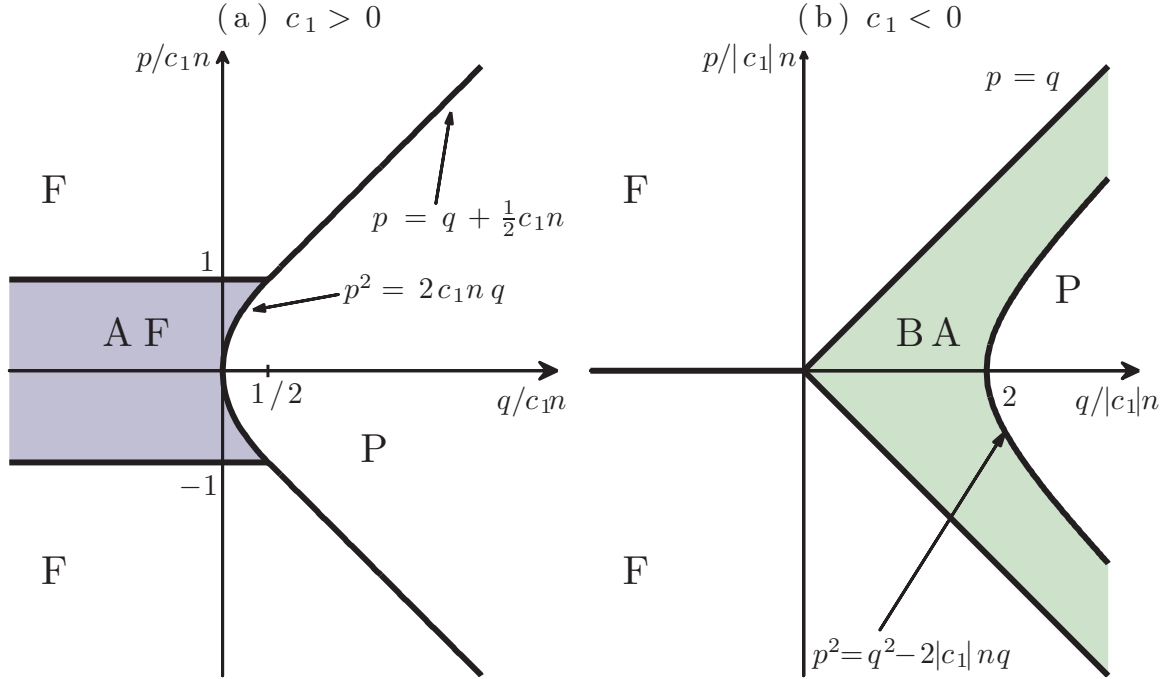
Figure 2.2: The zero temperature phase diagram of a spin-1 Bose gas in a constant magnetic field, for cases with (a) *antiferromagnetic* interactions (i.e. $c_1 > 0$), and (b) *ferromagnetic* interactions (i.e. $c_1 < 0$). The vertical and horizontal axes are the linear and quadratic Zeeman energies (see text) in units of $|c_1|n$, where n is the condensate number density. The phases shown are (F) ferromagnetic, (P) polar, (AF) antiferromagnetic, and broken-axisymmetric (BA) (see Refs. [28, 34]). The rotational symmetry about the direction of the applied field is spontaneously broken in the AF and BA phases.

Phase	Properties
Ferromagnetic (F)	Fully magnetized $|f_z| = n$, $|f_\perp| = 0$. $\boldsymbol{\xi} = [1, 0, 0]^T$ or $[0, 0, 1]^T$.
Polar (P)	Unmagnetized $|f_z| = |f_\perp| = 0$. $\boldsymbol{\xi} = [0, 1, 0]^T$
Antiferromagnetic (AF)	Partially magnetized $|f_z| \leq n$, $|f_\perp| = 0$. Condensate spinor has non-zero components in the $m_F = \pm 1$ sublevels.
Broken-axisymmetric (BA)	Partially magnetized, but tilts to the z axis giving $f_\perp > 0$. Condensate spinor has non-zero components in all sublevels.

Table 2.3: The phases of a spin-1 BEC in a constant magnetic field, as presented in Fig. 2.2, categorised according to their magnetization.

2.2.4 Symmetry

The symmetries of the condensate spinor are not easily seen by just looking at its components. To visualize these symmetries, it is helpful to use the spherical-harmonic representation

$$\Psi(\hat{\boldsymbol{s}}) = \sum_m \xi_m Y_F^m(\hat{\boldsymbol{s}}), \tag{2.27}$$

where $\hat{\boldsymbol{s}}$ is a unit vector in spin space, i.e. (f_x, f_y, f_z) space. For our system with $F = 1$, we use the three spherical harmonics

$$Y_1^0 = \frac{1}{2}\sqrt{\frac{3}{\pi}} \cos(\theta), \tag{2.28}$$

$$Y_1^{\pm 1} = \mp \frac{1}{2}\sqrt{\frac{3}{2\pi}} e^{\pm i\phi} \sin(\theta). \tag{2.29}$$

Using Eq. (2.27), we can generate a surface plot of $|\Psi(\hat{\boldsymbol{s}})|^2$ and colour it with $\arg \Psi(\hat{\boldsymbol{s}})$. This gives us a 3D representation of the spinor which can be used to compare the symmetry of the condensate within different phases. We can easily tell whether different order parameters have the same symmetry by seeing if they can be rotated onto each other. Throughout Chapter 5, we show the spherical-harmonic representation of the spinor in all four magnetic ground states. This reveals the symmetry of these phases and how they relate and transform between each other.

2.2.5 Nematic tensor

In addition to the spin density, an important characterization of the condensate order is provided by the nematic tensor

$$q_{\alpha\beta} = n\boldsymbol{\xi}^{\dagger} Q_{\alpha\beta} \boldsymbol{\xi}, \tag{2.30}$$

where $Q_{\alpha\beta} \equiv \frac{1}{2} (F_{\alpha} F_{\beta} + F_{\beta} F_{\alpha})$ is a 3×3 matrix for each pair of $\alpha, \beta \in \{x, y, z\}$. The nematic tensor is symmetric, and thus has six independent components.

$$Q_{xx} = \begin{pmatrix} \frac{1}{2} & 0 & \frac{1}{2} \\ 0 & 1 & 0 \\ \frac{1}{2} & 0 & \frac{1}{2} \end{pmatrix}, \qquad Q_{yy} = \begin{pmatrix} \frac{1}{2} & 0 & -\frac{1}{2} \\ 0 & 1 & 0 \\ -\frac{1}{2} & 0 & \frac{1}{2} \end{pmatrix}, \qquad Q_{zz} = \begin{pmatrix} 1 & 0 & 0 \\ 0 & 0 & 0 \\ 0 & 0 & 1 \end{pmatrix},$$

$$Q_{xy} = i \begin{pmatrix} 0 & 0 & -\frac{1}{2} \\ 0 & 0 & 0 \\ \frac{1}{2} & 0 & 0 \end{pmatrix}, \quad Q_{xz} = \frac{1}{\sqrt{2}} \begin{pmatrix} 0 & \frac{1}{2} & 0 \\ \frac{1}{2} & 0 & -\frac{1}{2} \\ 0 & -\frac{1}{2} & 0 \end{pmatrix}, \quad Q_{yz} = \frac{i}{\sqrt{2}} \begin{pmatrix} 0 & -\frac{1}{2} & 0 \\ \frac{1}{2} & 0 & \frac{1}{2} \\ 0 & -\frac{1}{2} & 0 \end{pmatrix}. \tag{2.31}$$

Chapter 3

Spin-1 Bogoliubov Theory

In this chapter we develop a framework for understanding the collective excitations that appear on top of the condensate. Our motivation for this is that we want to access information revealed by fluctuations about the mean values of measurable quantities. Firstly, we briefly review the derivation of the quasiparticle amplitudes by constructing the Bogoliubov Hamiltonian and diagonalizing it. The resulting solutions give three quasiparticle 'spin mode' branches, and we present analytic results for the four magnetic phases of the spinor BEC.

3.1 Constructing the Bogoliubov Hamiltonian

To construct the Bogoliubov Hamiltonian, we substitute the field operator decomposition given by Eq. (2.14) into the initial Hamiltonian in Eq. (2.2) and keep terms up to second order in $\hat{\delta}_m$ (i.e. up to terms with four field operators where two are non-condensate). Since we are considering the uniform system, it is helpful to expand each field operator in the plane wave basis as

$$\hat{\psi}_m(\mathbf{x}) = \frac{1}{\sqrt{V}} \sum_{\mathbf{k}} \hat{a}_{\mathbf{k}m} e^{i\mathbf{k}\cdot\mathbf{x}}. \tag{3.1}$$

The $\hat{a}_{\mathbf{k}m}$ operators satisfy the Bose commutation relations

$$[\hat{a}_{\mathbf{k}m}, \hat{a}^{\dagger}_{\mathbf{k}',m'}] = \delta_{\mathbf{k}\mathbf{k}'}\delta_{mm'}, \tag{3.2}$$

$$[\hat{a}_{\mathbf{k}m}, \hat{a}_{\mathbf{k}',m'}] = [\hat{a}^{\dagger}_{\mathbf{k}m}, \hat{a}^{\dagger}_{\mathbf{k}',m'}] = 0. \tag{3.3}$$

Assuming we have a BEC, we have macroscopic occupation of the $\mathbf{k} = \mathbf{0}$ mode, thus we make the substitutions:

$$\hat{a}^\dagger_{\mathbf{0},m}\hat{a}_{\mathbf{0},m'} \to \hat{N}_0\xi^*_m\xi_{m'}, \tag{3.4}$$

$$\hat{a}^\dagger_{\mathbf{0},m}\hat{a}^\dagger_{\mathbf{0},m'}\hat{a}_{\mathbf{0},n}\hat{a}_{\mathbf{0},n'} \to \hat{N}_0(\hat{N}_0 - 1)\xi^*_m\xi^*_{m'}\xi_n\xi_{n'}, \tag{3.5}$$

where, for a system with a fixed number of atoms N,

$$\hat{N}_0 \equiv N - \sum_{\mathbf{k}\neq\mathbf{0},m} \hat{a}^\dagger_{\mathbf{k}m}\hat{a}_{\mathbf{k}m}, \tag{3.6}$$

$$\hat{N}_0(\hat{N}_0 - 1) \approx N^2 - 2N \sum_{\mathbf{k}\neq\mathbf{0},m} \hat{a}^\dagger_{\mathbf{k}m}\hat{a}_{\mathbf{k}m}. \tag{3.7}$$

We keep only first order terms in these sums (higher ones are beyond quadratic order in operators). After further calculation, we get the Bogoliubov Hamiltonian,

$$\hat{H}^B = \frac{1}{2} \sum_{\mathbf{k}\neq\mathbf{0},m,m'} \begin{pmatrix} \hat{\mathbf{a}}^\dagger_{\mathbf{k}} & \hat{\mathbf{a}}_{-\mathbf{k}} \end{pmatrix} \begin{pmatrix} [\mathbf{H_k} + \mathbf{H}^{(1)}] & \mathbf{H}^{(2)} \\ [\mathbf{H}^{(2)}]^* & [\mathbf{H_k} + \mathbf{H}^{(1)}]^* \end{pmatrix} \begin{pmatrix} \hat{\mathbf{a}}_{\mathbf{k}} \\ \hat{\mathbf{a}}^\dagger_{-\mathbf{k}} \end{pmatrix}$$
$$+ E_0 - \frac{1}{2} \sum_{\mathbf{k}\neq\mathbf{0}} \mathrm{Tr}[\mathbf{H_k} + \mathbf{H}^{(1)}], \tag{3.8}$$

where

$$E_0 \equiv N \left\{ -pf_z/n + q\left[|\xi_+|^2 + |\xi_-|^2\right] + \frac{n}{2}\left[c_0 + c_1\left(1 - |\xi_0\xi_0 - 2\xi_+\xi_-|^2\right)\right] \right\}, \tag{3.9}$$

is the condensate energy-functional, and we have defined

$$\mathbf{H_k} \equiv \begin{pmatrix} (\epsilon_{\mathbf{k}} - \mu) - p + q & 0 & 0 \\ 0 & (\epsilon_{\mathbf{k}} - \mu) & 0 \\ 0 & 0 & (\epsilon_{\mathbf{k}} - \mu) + p + q \end{pmatrix}, \tag{3.10}$$

where

$$\mu = -pf_z/n + q(1 - |\xi_0|^2) + (c_0 + c_1)n - c_1 n|\xi_0^2 - 2\xi_+\xi_-|^2, \tag{3.11}$$

is the chemical potential of the condensate. We also define

$$\mathbf{H}^{(1)} \equiv n(c_0 + c_1)(\boldsymbol{\rho} + \mathbb{1}) - 2c_1 n \begin{pmatrix} |\xi_-|^2 & -\xi^*_-\xi_0 & \xi^*_-\xi_+ \\ -\xi^*_0\xi_- & |\xi_0|^2 & -\xi^*_0\xi_+ \\ \xi^*_+\xi_- & -\xi^*_+\xi_0 & |\xi_+|^2 \end{pmatrix}, \tag{3.12}$$

$$\mathbf{H}^{(2)} \equiv n(c_0 + c_1)\tilde{\boldsymbol{\rho}} + c_1 n(\xi_0^2 - 2\xi_+\xi_-) \begin{pmatrix} 0 & 0 & 1 \\ 0 & -1 & 0 \\ 1 & 0 & 0 \end{pmatrix}, \tag{3.13}$$

$$(\boldsymbol{\rho})_{mm'} \equiv \xi_m \xi_{m'}^*, \tag{3.14}$$

$$(\tilde{\boldsymbol{\rho}})_{mm'} \equiv \xi_m \xi_{m'}, \tag{3.15}$$

with the free particle energy $\epsilon_{\mathbf{k}}$ defined as

$$\epsilon_{\mathbf{k}} \equiv \hbar^2 k^2 / 2M. \tag{3.16}$$

3.2 Diagonalizing

We diagonalize the Bogoliubov Hamiltonian using the Bogoliubov transformation

$$\hat{a}_{\mathbf{k}m} = \sum_\nu U_{\mathbf{k}m\nu} \hat{\alpha}_{\mathbf{k}\nu} + V_{-\mathbf{k}m\nu}^* \hat{\alpha}_{-\mathbf{k}\nu}^\dagger, \tag{3.17}$$

$$\hat{a}_{-\mathbf{k}m}^\dagger = \sum_\nu U_{-\mathbf{k}m\nu}^* \hat{\alpha}_{-\mathbf{k}\nu}^\dagger + V_{\mathbf{k}m\nu} \hat{\alpha}_{\mathbf{k}\nu}, \tag{3.18}$$

where $\hat{\alpha}_{\mathbf{k}\nu}$ and $\hat{\alpha}_{-\mathbf{k}\nu}^\dagger$ are quasiparticle mode operators. We can write this in matrix form as

$$\begin{pmatrix} \hat{\mathbf{a}}_{\mathbf{k}} \\ \hat{\mathbf{a}}_{-\mathbf{k}}^\dagger \end{pmatrix} = \begin{pmatrix} U_{\mathbf{k}} & V_{-\mathbf{k}}^* \\ V_{\mathbf{k}} & U_{-\mathbf{k}}^* \end{pmatrix} \begin{pmatrix} \hat{\boldsymbol{\alpha}}_{\mathbf{k}} \\ \hat{\boldsymbol{\alpha}}_{-\mathbf{k}}^\dagger \end{pmatrix}. \tag{3.19}$$

It is convenient to use the columns of the U and V matrices, i.e. we write

$$U_{\mathbf{k}} = [\mathbf{u}_{\mathbf{k}\nu}], \tag{3.20}$$

$$V_{\mathbf{k}} = [\mathbf{v}_{\mathbf{k}\nu}], \tag{3.21}$$

where $\mathbf{u}_{\mathbf{k}\nu}$, $\mathbf{v}_{\mathbf{k}\nu}$ are 3×1 vectors, with $\nu \in \{0, 1, 2\}$ the spin-branch index. Enforcing Bose commutation relations on the quasiparticle operators, we can invert Eq. (3.19) to get

$$\hat{\alpha}_{\mathbf{k}\nu} = \mathbf{u}_{\mathbf{k}\nu}^\dagger \hat{\mathbf{a}}_{\mathbf{k}} - \mathbf{v}_{\mathbf{k}\nu}^\dagger \hat{\mathbf{a}}_{-\mathbf{k}}^\dagger, \tag{3.22}$$

$$\hat{\alpha}_{-\mathbf{k}\nu}^\dagger = \mathbf{v}_{-\mathbf{k}\nu}^T \hat{\mathbf{a}}_{\mathbf{k}} - \mathbf{u}_{-\mathbf{k}\nu}^T \hat{\mathbf{a}}_{-\mathbf{k}}^\dagger, \tag{3.23}$$

which shows that the quasiparticle excitation operators are linear combinations of the boson field operators. Using this transformation, we end up having to diagonalize the 6×6 matrix

$$\sigma_z M_{\mathbf{k}}^B \begin{pmatrix} \mathbf{u}_{\mathbf{k}\nu} \\ \mathbf{v}_{\mathbf{k}\nu} \end{pmatrix} = E_{\mathbf{k}\nu} \begin{pmatrix} \mathbf{u}_{\mathbf{k}\nu} \\ \mathbf{v}_{\mathbf{k}\nu} \end{pmatrix}, \tag{3.24}$$

where

$$\sigma_z = \begin{pmatrix} \mathbb{1} & 0 \\ 0 & -\mathbb{1} \end{pmatrix}, \tag{3.25}$$

and

$$M_{\mathbf{k}}^B = \begin{pmatrix} [\mathbf{H_k} + \mathbf{H}^{(1)}] & \mathbf{H}^{(2)} \\ [\mathbf{H}^{(2)}]^* & [\mathbf{H_k} + \mathbf{H}^{(1)}]^* \end{pmatrix}. \tag{3.26}$$

We get six solution branches, only half of which satisfy the orthonormalization condition imposed by the commutation relations. This gives us our three excitation branches (i.e. $\nu = 0, 1, 2$).

We note that, in general, the eigenvalues can be complex. If they are not real-valued, then this indicates that the mean-field condensate is not the true ground state and the system is dynamically unstable. In this situation, the quasiparticles with largest imaginary part undergo exponential growth and destroy the BEC. For our purposes, we are interested in the modes that have positive real-valued energies, which means we always calculate the correct ground state spinor for the phase we are in before we diagonalize to find the quasiparticle amplitudes.

3.3 Quasiparticles

Here we give an overview of the known analytic forms of the quasiparticle excitations for the four ground state phases of the condensate, following Ref. [28] but labelling the spin modes to be consistent with our analysis in Chapter 5. We have analytic forms for the F, P, AF, and BA phases, although only for the case of $p = 0$ in the BA phase [28]. For the F and P phases, we also have analytic forms for the amplitudes (see Ref. [28]). In general, for the AF and BA phases these are quite complicated and analytic forms have not been published to our knowledge, although the equations describing them are detailed in Ref. [66].

For the F, P, AF at $f_z = 0$ and BA at $p = 0$ phases, the quasiparticle amplitudes are given in Sec. 5.2 of [28], and in [66] for BA with $p \neq 0$.

For the AF phase, we have derived analytic low k limits for the quasiparticle amplitude differences that we need in subsequent chapters. For $0 < c_1 \ll c_0$, they are

$$[\mathbf{u}_{\mathbf{k}0} - \mathbf{v}_{\mathbf{k}0}]_{\pm} = \sqrt{1 \pm \frac{f_z}{n}} \left[1 \pm \frac{f_z}{n} \left(1 \mp \frac{5 f_z}{4n} \right) \frac{c_1}{c_0} \right] \frac{\sqrt{k \xi_n}}{2}, \tag{3.27}$$

$$[\mathbf{u}_{\mathbf{k}1} - \mathbf{v}_{\mathbf{k}1}]_{\pm} = \frac{\sqrt{1 \mp \frac{f_z}{n}}}{(1 - \frac{f_z^2}{n^2})^{1/4}} \left[\pm 1 - \frac{f_z}{n} \left(1 \pm \frac{3 f_z}{4n} \right) \frac{c_1}{c_0} \right] \frac{\sqrt{k \xi_s}}{2}, \tag{3.28}$$

where ξ_n and ξ_s are the density and spin healing lengths defined respectively in Eqs. (2.13) and (2.12). These expressions reduce to the result in [28] for $f_z = 0$ and small k.

For the analytic results in the BA phase (at $p = 0$), we have defined

$$\Omega \equiv 2(c_1 n)^2 (1 - \tilde{q}^2), \tag{3.29}$$

$$\Lambda_k \equiv \sqrt{[(c_0 n - 3|c_1|n)\epsilon_{\mathbf{k}} - \Omega]^2 + 4|c_1|n(c_0 n - 2|c_1|n)\tilde{q}^2(\epsilon_{\mathbf{k}})^2}. \tag{3.30}$$

We note that we have derived these results independently and verified them numerically, and as a result we have corrected some minor errors in the AF and BA results of Ref. [28].

Phase	ν	Energy spectrum $E_{\mathbf{k}\nu}$	$\mathbf{u}_{\mathbf{k}\nu}^T$	$\mathbf{v}_{\mathbf{k}\nu}^T$
F	0	$\sqrt{\epsilon_{\mathbf{k}}(\epsilon_{\mathbf{k}} + 2(c_0 + c_1)n)}$	$(u, 0, 0)$	$(v, 0, 0)$
	1	$\epsilon_{\mathbf{k}} + 2p - 2c_1 n$	$(0, 0, 1)$	$(0, 0, 0)$
	2	$\epsilon_{\mathbf{k}} + p - q$	$(0, 1, 0)$	$(0, 0, 0)$
P	0	$\sqrt{\epsilon_{\mathbf{k}}(\epsilon_{\mathbf{k}} + 2c_0 n)}$	$(0, u, 0)$	$(0, v, 0)$
	1	$\sqrt{(\epsilon_{\mathbf{k}} + q)(\epsilon_{\mathbf{k}} + q + 2c_1 n)} - p$	$(u, 0, 0)$	$(0, 0, v)$
	2	$\sqrt{(\epsilon_{\mathbf{k}} + q)(\epsilon_{\mathbf{k}} + q + 2c_1 n)} + p$	$(0, 0, u)$	$(v, 0, 0)$
AF	$\begin{array}{c}0 \to + \\ 1 \to -\end{array}$	$\sqrt{\epsilon_{\mathbf{k}}\left[\epsilon_{\mathbf{k}} + (c_0 + c_1)n \pm n\sqrt{(c_0 - c_1)^2 + 4c_0 c_1 f_z^2}\right]}$	$(u, 0, u')$	$(v, 0, v')$
	2	$\sqrt{(\epsilon_{\mathbf{k}} - q + c_1 n)^2 - (1 - f_z^2)(c_1 n)^2}$	$(0, u, 0)$	$(0, v, 0)$
BA $(p = 0)$	$0, 1$	$\sqrt{\epsilon_{\mathbf{k}}(\epsilon_{\mathbf{k}} + c_0 n + |c_1|n) + \Omega \pm \Lambda_k}$	(u, u', u)	(v, v', v)
	2	$\sqrt{\epsilon_{\mathbf{k}}(\epsilon_{\mathbf{k}} + q)}$	$(u, 0, -u)$	$(v, 0, -v)$

Table 3.1: Quasiparticle excitations, labelled by spin mode ν, showing their spectrum and the general form of their $\mathbf{u}_{\mathbf{k}\nu}$ and $\mathbf{v}_{\mathbf{k}\nu}$ amplitudes. We have dropped the ν subscript on the amplitude components u, v, u' and v' for brevity. Further details can be found in Sec. 5.2 of [28], and in Refs. [66, 72]. We have used $\tilde{q}$ as defined in Eq. (2.25) and the free particle energy $\epsilon_{\mathbf{k}}$ as defined in Eq. (3.16). The $\nu \in \{0, 1\}$ modes in the BA phase have an avoided crossing. For these energies: before the crossing, we take $0 \to -, 1 \to +$; after the crossing we switch to $0 \to +, 1 \to -$.

Chapter 4

Spin and Density correlations

In this chapter we look at generalized density correlation functions, creating a formalism to describe fluctuations in a general multicomponent spinor gas. We separate out the behaviour of the correlation function into coherent and incoherent parts, which each become dominant at certain length scales. We use this correlation function to define a generalized static structure factor, whose behaviour we shall explore in Chapter 5 and then use in Chapter 6 to characterize fluctuations within measurement cells.

4.1   Observable

Our interest lies in the fluctuations that occur in the total and spin densities of the system, as characterized by the observables given in Eqs. (2.3) and (2.4). We will generically represent these observables as

$$\hat{w}(\mathbf{x}) = \hat{\boldsymbol{\psi}}^{\dagger}(\mathbf{x}) \mathrm{W} \hat{\boldsymbol{\psi}}(\mathbf{x}), \tag{4.1}$$

where W is a 3×3 matrix.[1] In the low temperature regime of interest the mean value is determined by the condensate and is spatially constant, i.e.

$$w = \langle \hat{w}(\mathbf{x}) \rangle = n \boldsymbol{\xi}^{\dagger} \mathrm{W} \boldsymbol{\xi}, \tag{4.2}$$

and in what follows we consider the fluctuations about this mean value.

---

[1]In this thesis we will consider the cases of $\mathrm{W} \in \{\mathbb{1}, \mathrm{F}_x, \mathrm{F}_y, \mathrm{F}_z\}$, i.e. $\hat{w}(\mathbf{x})$ being the total density or a component of the spin density.

4.2 w density-density correlation function

The spatial fluctuations of $\hat{w}$ are characterized by the two-point correlation function

$$C_w(\mathbf{x} - \mathbf{x}') = \langle \delta\hat{w}(\mathbf{x})\delta\hat{w}(\mathbf{x}') \rangle, \tag{4.3}$$

where we have introduced the fluctuation operator

$$\delta\hat{w}(\mathbf{x}) = \hat{w}(\mathbf{x}) - w. \tag{4.4}$$

Because we consider a uniform system, C_w only depends on the relative separation of the two points.

It is convenient to use the Bose commutation relations to rewrite the correlation function in the form

$$C_w(\mathbf{x} - \mathbf{x}') = \langle : \delta\hat{w}(\mathbf{x})\delta\hat{w}(\mathbf{x}') : \rangle + \overline{w^2}\,\delta(\mathbf{x} - \mathbf{x}'), \tag{4.5}$$

where

$$\overline{w^2} \equiv \langle \hat{\boldsymbol{\psi}}^\dagger(\mathbf{x})\mathrm{W}^2\hat{\boldsymbol{\psi}}(\mathbf{x}) \rangle = n\boldsymbol{\xi}^\dagger\mathrm{W}^2\boldsymbol{\xi}. \tag{4.6}$$

The delta-function term in Eq. (4.5) represents the autocorrelation of individual atoms (shot noise), and a completely uncorrelated system is one in which $C_w(\mathbf{r}) = \overline{w^2}\,\delta(\mathbf{r})$. The normally ordered term in Eq. (4.5) thus represents the correlations arising from quantum degeneracy and interaction effects.

4.3 Static structure factor

The w static structure factor is defined as

$$S_w(\mathbf{k}) \equiv \frac{1}{N}\int d\mathbf{x}\, d\mathbf{x}'\, C_w(\mathbf{x} - \mathbf{x}')e^{-i\mathbf{k}(\mathbf{x} - \mathbf{x}')}, \tag{4.7}$$

$$= \frac{\langle \delta\hat{w}_\mathbf{k}\delta\hat{w}_{-\mathbf{k}} \rangle}{N}. \tag{4.8}$$

Here $\delta\hat{w}_\mathbf{k}$ is the Fourier transformed fluctuation operator

$$\delta\hat{w}_\mathbf{k} \equiv \int d\mathbf{x}\, e^{-i\mathbf{k}\cdot\mathbf{x}}\delta\hat{w}(\mathbf{x}), \tag{4.9}$$

$$\approx \sqrt{N}\sum_\nu \left(\delta\tilde{w}_{\mathbf{k}\nu}\hat{\alpha}_{\mathbf{k}\nu} + \delta\tilde{w}_{\mathbf{k}\nu}^*\hat{\alpha}_{-\mathbf{k}\nu}^\dagger \right), \tag{4.10}$$

where

$$\delta\tilde{w}_{\mathbf{k}\nu} \equiv \boldsymbol{\xi}^\dagger\mathrm{W}\mathbf{u}_{\mathbf{k}\nu} - \mathbf{v}_{\mathbf{k}\nu}^T\mathrm{W}\boldsymbol{\xi}, \tag{4.11}$$

is a quantity we will refer to as the w fluctuation amplitude. In obtaining Eq. (4.10), we have substituted the field operator expansion Eq. (2.14) into Eq. (4.4) to get

$$\delta\hat{w}(\mathbf{x}) = \sqrt{n}\sum_{mn} W_{mn}\left(\xi_m^*\hat{\delta}_n + \xi_n\hat{\delta}_m^\dagger\right) + \sum_{mn} W_{mn}\langle\hat{\delta}_m^\dagger\hat{\delta}_n\rangle + \sum_{mn}\hat{\delta}_m^\dagger W_{mn}\hat{\delta}_n, \tag{4.12}$$

and then neglected higher order terms in the quasiparticle operators, giving

$$\delta\hat{w}(\mathbf{x}) \approx \sqrt{n}\sum_{mn} W_{mn}\left(\xi_m^*\hat{\delta}_n + \xi_n\hat{\delta}_m^\dagger\right), \tag{4.13}$$

which should be a good approximation at low temperatures. Using our Bogoliubov formalism from Chapter 3, we can write the non-condensate operator as

$$\hat{\boldsymbol{\delta}}(\mathbf{x}) = \sum_{\mathbf{k}\neq\mathbf{0},\nu}(\mathbf{u}_{\mathbf{k}\nu}\hat{\alpha}_{\mathbf{k}\nu} + \mathbf{v}_{\mathbf{k}\nu}^*\hat{\alpha}_{-\mathbf{k}\nu}^\dagger)\frac{e^{i\mathbf{k}\cdot\mathbf{x}}}{\sqrt{V}}. \tag{4.14}$$

Substituting this into Eq. (4.13) and taking the Fourier transform, we get Eq.(4.10).

The static structure factor is then given by

$$S_w(\mathbf{k}) = \sum_\nu |\delta\tilde{w}_{\mathbf{k}\nu}|^2 \coth\left(\frac{E_{\mathbf{k}\nu}}{2k_BT}\right), \tag{4.15}$$

where we have used that

$$\langle\hat{\alpha}_{\mathbf{k}\nu}^\dagger\hat{\alpha}_{\mathbf{k}'\nu'}\rangle = \frac{\delta_{\mathbf{k}\mathbf{k}'}\delta_{\nu\nu'}}{e^{E_{\mathbf{k}\nu}/k_BT} - 1}, \tag{4.16}$$

with δ_{ab} the Kronecker delta.

In the high k limit, where the kinetic energy is large compared to the thermal and interaction energies, only the uncorrelated part of C_w contributes and from Eq. (4.7) we have

$$S_w(k\to\infty) = \frac{1}{n}\overline{w^2}. \tag{4.17}$$

We refer to this as the uncorrelated limit of the structure factor.

4.4 Results for Spin-1

We now specialise our general formalism of this Chapter to the case of total and spin density fluctuations, adopting the notation

$$\hat{w} \to \{\hat{n}, \hat{f}_x, \hat{f}_y, \hat{f}_z\}, \tag{4.18a}$$

$$\mathrm{W} \to \{\mathbb{1}, \mathrm{F}_x, \mathrm{F}_y, \mathrm{F}_z\}, \tag{4.18b}$$

$$\delta\tilde{w}_{\mathbf{k}\nu} \to \{\delta\tilde{n}_{\mathbf{k}\nu}, \delta\tilde{f}_{x,\mathbf{k}\nu}, \delta\tilde{f}_{y,\mathbf{k}\nu}, \delta\tilde{f}_{z,\mathbf{k}\nu}\}, \tag{4.18c}$$

$$S_w(\mathbf{k}) \to \{S_n(\mathbf{k}), S_x(\mathbf{k}), S_y(\mathbf{k}), S_z(\mathbf{k})\}. \tag{4.18d}$$

Using our analytic results from Chapter 3, and aided by Mathematica, we have constructed the Bogoliubov Hamiltonian and diagonalized to find the quasiparticles for each phase. From these we form expressions for the relevant structure factors. For each structure factor we find a limiting expression for the low k and high k behaviour. These results have been checked against known analytic results.

We have also implemented Python code to diagonalize the Hamiltonian at each point on a k-grid. From this we can numerically construct each structure factor and we have checked our limits against these numerical results and found agreement to within numerical precision.

Numerically implementing our formalism required a significant amount of coding. To analyze a point on the phase diagram, we take as input the interaction parameters, f_z magnetization, quadratic Zeeman and linear Zeeman parameters. We then compute the correct ground state spinor, and construct the Bogoliubov Hamiltonian on a k-grid. When diagonalizing, to look at fluctuation amplitudes it was necessary to correctly order the resulting energies across the k-grid.

We made use of the NumPy libraries to efficiently represent our data. The NumPy diagonalization method we used (numpy.linalg.eig) is efficiently implemented using low-level LAPACK routines in Fortran, and meant that our code runs in a few minutes for k-grids of order 10^5 points.

We summarise our extensive analytic and numeric work on the limiting expressions of the structure factors in the Tables that follow. In Table 4.1, we detail expressions found for the low k behaviour of the fluctuation amplitudes $\delta\tilde{w}_{\mathbf{k}\nu}$ for each spin mode ν and operator $\hat{w}$. In Table 4.2, we detail our results for the low k and high k limits – with $T = 0$ and $T > 0$ limits for low k – for all the structure factors $S_w(\mathbf{k})$. Both Tables comprehensively detail the limiting behaviours and effects of the three quasiparticle modes throughout the (p, q) phase diagram of the uniform spin-1 condensate. In the following Chapter we go beyond these analytic limits and numerically explore the excitations and fluctuations of the four ground state phases in detail.

Phase	Obs.(s)	$\|\delta\hat{w}_{\mathbf{k}\nu}\|^2$		
		$\nu = 0$	$\nu = 1$	$\nu = 2$
F	$\hat{n}, \hat{f}_z$	$\sqrt{\dfrac{\epsilon_{\mathbf{k}}}{2(c_0 + c_1)n}}$	0	0
	$\hat{f}_x, \hat{f}_y$	0	0	$\dfrac{1}{2}$
P	$\hat{n}$	$\dfrac{k\xi_n}{2}$	0	0
	$\hat{f}_z$	0	0	0
	$\hat{f}_x, \hat{f}_y$	0	$\dfrac{1}{2\sqrt{1 + 2c_1 n/q}}$	$\dfrac{1}{2\sqrt{1 + 2c_1 n/q}}$
AF	$\hat{n}$	$\left(1 - \dfrac{1}{2}\dfrac{\hat{f}_z^2}{n^2}\dfrac{c_1}{c_0}\right)\dfrac{k\xi_n}{2}$	$\dfrac{\hat{f}_z^2}{n^2}\sqrt{1 - \dfrac{\hat{f}_z^2}{n^2}\dfrac{c_1^{3/2}}{c_0^{3/2}}}\dfrac{k\xi_n}{2}$	0
	$\hat{f}_z$	$\dfrac{\hat{f}_z^2}{n^2}\sqrt{\dfrac{c_1}{c_0}}\dfrac{k\xi_s}{2}$	$\sqrt{1 - \dfrac{\hat{f}_z^2}{n^2}}\left(1 - \dfrac{3\hat{f}_z^2}{2n^2}\dfrac{c_1}{c_0}\right)\dfrac{k\xi_s}{2}$	0
	$\hat{f}_x \to +$ $\hat{f}_y \to -$	0	0	$\dfrac{1}{2}\left(\dfrac{1 \pm \alpha_z}{1 \pm \alpha_z - q/c_1 n}\right)\dfrac{E_{\mathrm{g},2}^{\mathrm{AF}}}{c_1 n}$
BA $(p=0)$	$\hat{n}$	$\sqrt{\dfrac{\epsilon_{\mathbf{k}}}{2(c_0 + c_1)n}}$	0	$\dfrac{\tilde{q}^2}{(1 - \tilde{q}^2)^{3/2}}\left(\dfrac{\epsilon_{\mathbf{k}}}{c_1 n}\right)^2$
	$\hat{f}_x$	$\dfrac{1}{1 - \tilde{q}^2}\sqrt{\dfrac{\epsilon_{\mathbf{k}}}{2(c_0 + c_1)n}}$	0	$\dfrac{\tilde{q}^2}{\sqrt{1 - \tilde{q}^2}}$
	$\hat{f}_y$	0	$\dfrac{1}{2}(1 + \tilde{q})\sqrt{\dfrac{q}{\epsilon_{\mathbf{k}}}}$	0
	$\hat{f}_z$	0	$\dfrac{1}{2}(1 - \tilde{q})\sqrt{\dfrac{\epsilon_{\mathbf{k}}}{q}}$	0

Table 4.1: Small k limits of fluctuation amplitudes. For $\hat{n}$ and f_z in the AF phase, the results are the first terms in an expansion for $c_1 \ll c_0$. Where the entry is zero, the fluctuation amplitude is zero for all k.

Phase	Obs.(s)	$S_w(k \to 0)$		$S_w(k \to \infty)$
		$T = 0$	$T > 0$	
F	$\hat{n}, \hat{f}_z$	$\sqrt{\dfrac{\epsilon_{\mathbf{k}}}{2(c_0 + c_1)n}}$	$\dfrac{k_B T}{(c_0 + c_1)n}$	1
	$\hat{f}_x, \hat{f}_y$	$\dfrac{1}{2}$	$\dfrac{k_B T}{E_{\mathrm{g},2}^{\mathrm{F}}}$	$\dfrac{1}{2}$
P	$\hat{n}$	$\dfrac{k\xi_n}{2}$	$\dfrac{k_B T}{c_0 n}$	1
	$\hat{f}_z$	0	0	0
	$\hat{f}_x, \hat{f}_y$	$\dfrac{1}{\sqrt{1 + 2c_1 n/q}}\left(1 + \dfrac{(c_1 n)^2}{q(q + 2c_1 n)}\dfrac{k^2 \xi_s^2}{2}\right)$	$\left(\dfrac{2q}{q(q + 2c_1 n) - p^2}\right)k_B T$	1
AF	$\hat{n}$	$\left[1 + \dfrac{f_z^2}{n^2}\left(-\dfrac{1}{2}\dfrac{c_1}{c_0} + \sqrt{1 - \dfrac{f_z^2}{n^2}}\left(\dfrac{c_1}{c_0}\right)^{3/2}\right)\right]\dfrac{k\xi_n}{2}$	$\dfrac{k_B T}{c_0 n}$	1
	$\hat{f}_z$	$\left[\sqrt{1 - \dfrac{f_z^2}{n^2}}\left(1 - \dfrac{3f_z^2}{2n^2}\dfrac{c_1}{c_0}\right) + \dfrac{f_z^2}{n^2}\sqrt{\dfrac{c_1}{c_0}}\right]\dfrac{k\xi_s}{2}$	$\dfrac{k_B T}{c_1 n}$	1
	$\hat{f}_x \to +$ $\hat{f}_y \to -$	$\dfrac{1}{2}\left(\dfrac{1 \pm \alpha_z}{1 \pm \alpha_z - q/c_1 n}\right)\left(\dfrac{E_{\mathrm{g},2}^{\mathrm{AF}}}{c_1 n} \pm \alpha_z \dfrac{c_1 n}{E_{\mathrm{g},2}^{\mathrm{AF}}}\dfrac{k^2 \xi_s^2}{2}\right)$	$\left(\dfrac{1 \pm \alpha_z}{1 \pm \alpha_z - q/c_1 n}\right)\dfrac{k_B T}{c_1 n}$	$\dfrac{1}{2}(1 \pm \alpha_z)$
BA $(p = 0)$	$\hat{n}$	$\sqrt{\dfrac{\epsilon_{\mathbf{k}}}{2(c_0 + c_1)n}}$	$\dfrac{k_B T}{(c_0 + c_1)n}$	1
	$\hat{f}_x$	$\dfrac{\tilde{q}^2}{\sqrt{1 - \tilde{q}^2}} + \dfrac{1}{1 - \tilde{q}^2}\sqrt{\dfrac{\epsilon_{\mathbf{k}}}{2(c_0 + c_1)n}}$	$\left(\dfrac{1}{(c_0 + c_1)n} + \dfrac{2\tilde{q}^2}{|c_1|n}\right)\dfrac{k_B T}{1 - \tilde{q}^2}$	1
	$\hat{f}_y$	$\dfrac{1}{2}(1 + \tilde{q})\sqrt{\dfrac{q}{\epsilon_{\mathbf{k}}}}$	$(1 + \tilde{q})\dfrac{k_B T}{\epsilon_{\mathbf{k}}}$	$\dfrac{1}{2}(1 + \tilde{q})$
	$\hat{f}_z$	$\dfrac{1}{2}(1 - \tilde{q})\sqrt{\dfrac{\epsilon_{\mathbf{k}}}{q}}$	$(1 - \tilde{q})\dfrac{k_B T}{q}$	$\dfrac{1}{2}(1 - \tilde{q})$

Table 4.2: High and low k limits of the structure factors. In the $k \to 0$ limits we distinguish between $T = 0$ and $T > 0$ results: In the $T = 0$ case we give a k expansion, whereas for $T > 0$ we give the structure factor value at $k = 0$. For $\hat{n}$ and $\hat{f}_z$ in the AF phase, the $T = 0$ results are the first terms in an expansion for $c_1 \ll c_0$ and the finite T results are valid for $|f_z| < n$. Note: in terms of $|c_1|n$ we have $\epsilon_{\mathbf{k}} = \frac{1}{2}k^2 \xi_s^2 |c_1|n$.

Chapter 5

Excitations and Fluctuations

In this Chapter we expand on our analytic results detailed in Tables 4.1 and 4.2 to fully explore the excitations for the ground state phases shown in Fig. 2.2, and how they manifest in the various structure factors. As we did at the end of Chapter 4, we specialise our general formalism to the case of total and spin density fluctuations. In the next subsections we discuss the various phases, their excitation spectra and fluctuations.

5.1 Parameter choice

With reference to Table 2.1 in Sec. 2, the most commonly realised spinor condensates of ^{87}Rb and ^{23}Na atoms have spin dependent interactions which are much smaller than their spin independent interactions. Additionally, ^{23}Na has $c_1 > 0$ (i.e. antiferromagnetic interactions), while ^{87}Rb has $c_1 < 0$ (i.e. ferromagnetic interactions). Here we choose to present results using $c_0 = -250c_1$ for BA, within the range of experimental predictions for ^{87}Rb, and using $c_0 = 50c_1$ for the other phases, within the range of experimental predictions for ^{23}Na. We adopt the spin healing length [see Eq. (2.12)] as a convenient length scale, noting that for our choice of parameters it is a factor of $\sqrt{50}$ or $\sqrt{250}$ larger than the density healing length [see Eq. (2.13)].
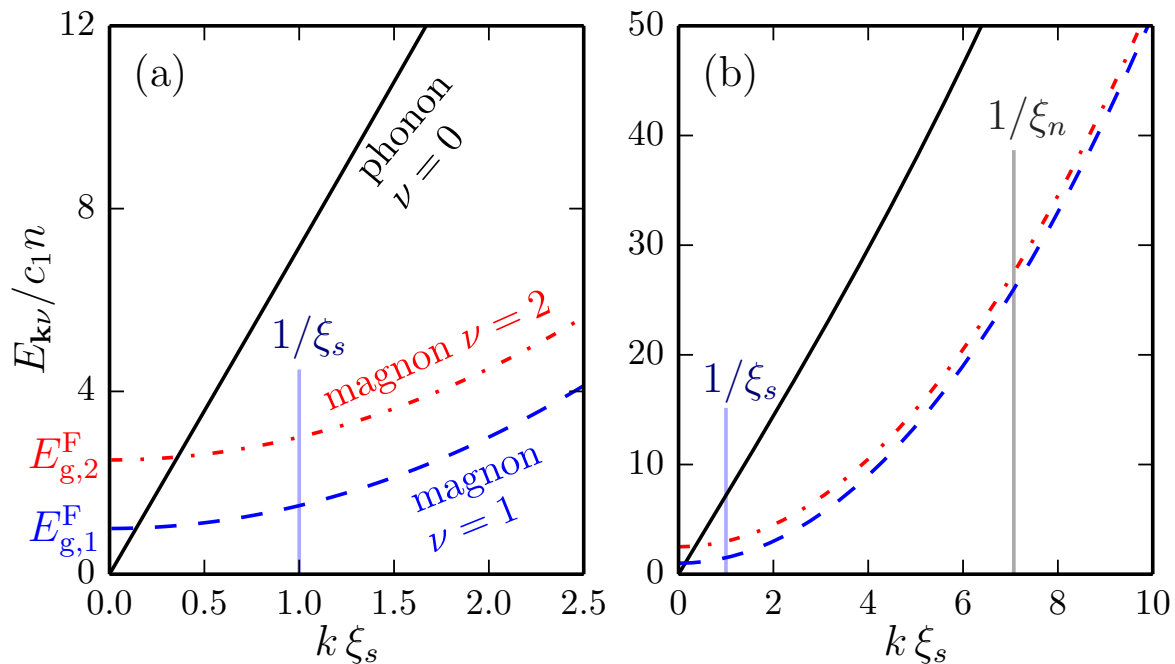
Figure 5.1: Bogoliubov dispersion relations in the F phase. Subplots (a) and (b) focus on different ranges of k values. We show the phonon (black solid line), magnon (blue dashed line), and transverse magnon (red dash-dot line) branches of the excitation spectra, and attribute these the indices $\nu = 0, 1, 2$, respectively. Parameters: $p = 1.5\, c_1 n$, $q = -c_1 n$, $c_0 = 50\, c_1$, $c_1 > 0$.

5.2   F phase

5.2.1   Condensate and excitation spectrum

The F phase occurs for both $c_1 > 0$ and $c_1 < 0$, and in this phase the condensate is completely magnetized in the $m_F = 1$ or -1 states depending on the value of p [see Fig. 2.2(a), (b)]. We will focus on the case $p > 0$ with atoms in the $m_F = 1$ state

$$\boldsymbol{\xi}^{\mathrm{F}} = [1, 0, 0]^T. \tag{5.1}$$

Here we have chosen $\boldsymbol{\xi}^{\mathrm{F}}$ to be real. The most general form of this state is obtained by applying an arbitrary gauge transformation $e^{i\chi_0}$ and a spin rotation about the z-spin axis (i.e. $e^{-i\mathrm{F}_z\chi_1}$) to $\boldsymbol{\xi}^{\mathrm{F}}$ (see Fig. 5.2). Because the F phase is axially symmetric these transformations leave the properties of the condensate, and its fluctuations, unchanged.

The nematic tensor [see Eq. (2.30)] for $\boldsymbol{\xi}^{\mathrm{F}}$ is

$$q^{\mathrm{F}} = n \begin{pmatrix} \frac{1}{2} & 0 & 0 \\ 0 & \frac{1}{2} & 0 \\ 0 & 0 & 1 \end{pmatrix}. \tag{5.2}$$
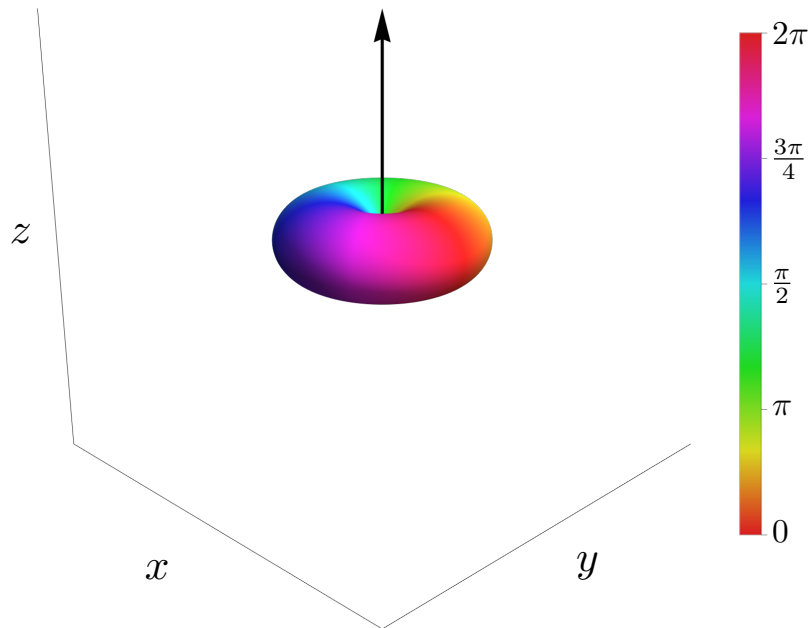

Figure 5.2: Surface plot of the spherical harmonic representation of the F spinor in spin-space [see Eq. (2.27)], coloured according to phase. Note the full axial symmetry about the z spin axis. We can see the spin-gauge symmetry in that a rotation about z is the same as a 2π phase winding.

An example of the excitation spectrum for the F state [28] is shown in Fig. 5.1. This spectrum has phonon (index $\nu = 0$), magnon (index $\nu = 1$), and transverse magnon (index $\nu = 2$) branches.[1] The phonon mode is the Nambu-Goldstone mode for this phase and resides entirely in the $m_F = 1$ component. The phonon is magnetic field independent and corresponds identically to the phonon mode of a scalar gas, but with an effective interaction of

$$c_0 + c_1 = 4\pi a_2 \hbar^2 / M, \tag{5.3}$$

corresponding to the scattering length of the spin-2 channel.

---

[1]We identify the phonon branch as that having the largest contribution to the density fluctuations. For the case that the condensate has an average spin we denote the magnon modes as transverse or axial if they give rise to fluctuations that are solely transverse or axial to the mean spin, respectively (c.f. [73]).

The magnon modes have energy gaps

$$E_{g,1}^{F} = 2p - 2c_1 n, \tag{5.4}$$

$$E_{g,2}^{F} = p - q, \tag{5.5}$$

for $\nu = 1$ and 2, respectively. These branches have quadratic dispersions, and are magnetic field sensitive (e.g. revealed by the dependence of $E_{g,1}^{F}$, $E_{g,2}^{F}$ on p and q). We now consider how these modes relate to fluctuations in the system for the observables of interest. This is most easily seen by examining the fluctuation amplitudes (i.e. $\delta \tilde{w}_{\mathbf{k}\nu}$), which reveal the contributions from the various excitation branches. By summing over these according to Eq. (4.15) the relevant static structure factors are then computed.

5.2.2 Fluctuations in n and f_z

Because the condensate resides entirely in the $m_F = 1$ level we trivially have $\mathsf{F}_z \boldsymbol{\xi}^F = \mathbb{1}\boldsymbol{\xi}^F$ so that [from Eq. (4.11)] the fluctuation amplitudes $\delta \tilde{n}_{\mathbf{k}\nu}$ and $\delta \tilde{f}_{z,\mathbf{k}\nu}$ are identical.[2] The results in Fig. 5.3(a) demonstrate that fluctuations in these quantities are entirely due to the phonon mode, with no contribution from either of the magnon modes. The (identical) static structure factors for density and axial spin are shown in Fig. 5.4(a) for several temperatures, with analytic limiting results given in Table 4.2. This behavior is similar to that of the density static structure factor for a scalar Bose gas, with the phonon speed of sound set by the scattering length of the spin-2 channel $(c_0 + c_1)$. For example,

$$S_n(\mathbf{0}) = k_B T / [(c_0 + c_1)n], \tag{5.6}$$

and the uncorrelated limit $[S_n(\mathbf{k}) \to 1]$ occurs for wavevectors $k \gg 1/\xi_n$ at sufficiently low temperatures [also see Table 4.2].

5.2.3 Fluctuations in f_x and f_y

The symmetry of the F phase about the spin z axis is reflected in the fluctuations of f_x and f_y being identical. Only the transverse magnon mode contributes to the fluctuation amplitudes $\delta \tilde{f}_{x,y}$, as shown in Fig. 5.3(b). Because this mode is single particle like, i.e.

$$\mathbf{u}_{\mathbf{k}2}^{T} = [0, 1, 0], \tag{5.7}$$

$$\mathbf{v}_{\mathbf{k}2}^{T} = \mathbf{0}, \tag{5.8}$$

---

[2]Note, for the F phase with the condensate in the $m_F = -1$ state, which we denote as $\boldsymbol{\xi}'_F$, then $\mathsf{F}_z \boldsymbol{\xi}^{F'} = -\mathbb{1}\boldsymbol{\xi}^{F'}$.
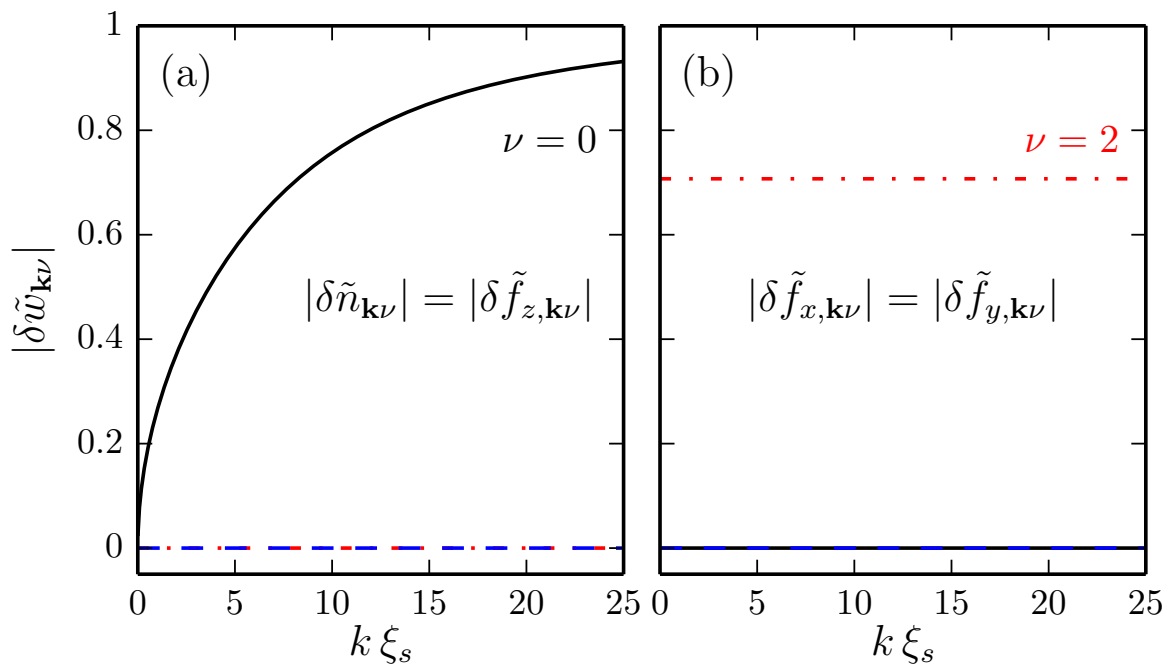
Figure 5.3: Fluctuation amplitudes for the F phase. Subplots (a) $\delta\tilde{n}_{\mathbf{k}\nu}$, $\delta\tilde{f}_{z,\mathbf{k}\nu}$, (b) $\delta\tilde{f}_{x,\mathbf{k}\nu}$, $\delta\tilde{f}_{y,\mathbf{k}\nu}$, as defined in Eq. (4.11). The modes (index ν) have the same line types as in Fig. 5.1. Other parameters as in Fig. 5.1.

the fluctuation amplitudes are constant valued with

$$|\delta\tilde{f}_{x,\mathbf{k}2}| = |\delta\tilde{f}_{x,\mathbf{k}2}| = 1/\sqrt{2}. \tag{5.9}$$

Note that the $\nu = 1$ magnon mode is of the form

$$\mathbf{u}_{\mathbf{k}1}^T = [0, 0, 1], \tag{5.10}$$

$$\mathbf{v}_{\mathbf{k}1}^T = \mathbf{0}, \tag{5.11}$$

and does not contribute to total density or spin density fluctuations.

The associated structure factors, S_x and S_y, are shown in Fig. 5.4(b), with analytic limiting results given in Table 4.2. These factors have a non-zero value for $k \to 0$ at $T = 0$, i.e.

$$S_{x,y}^{T=0}(k \to 0) \neq 0. \tag{5.12}$$

This behavior was also found for a two component system in Ref. [48], where the magnon mode was also energetically gapped. The energy gap of the transverse magnon mode delays the onset of thermal fluctuations to temperatures $T \gtrsim E_{\mathrm{g},2}^{\mathrm{F}}/k_B$.
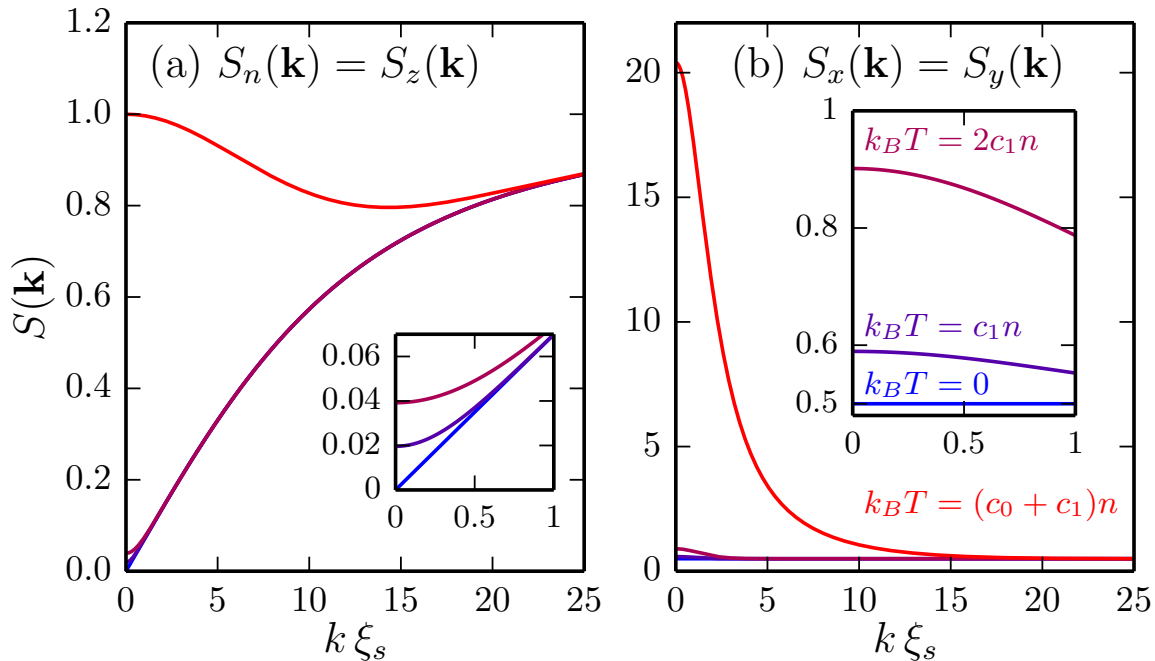
Figure 5.4: Static structure factors for the F phase at various temperatures. Structure factors (a) S_n and S_z (which are identical) (b) S_x and S_y (which are also identical), as defined in Eq. (4.15). For temperatures of (from bottom to top curves) $T = \{0, c_1, 2c_1, c_0 + c_1\} \times n/k_B$, as labelled in the inset to (b). Insets reveal additional detail for the lower temperature results at small $k\xi_s$. Other parameters as in Fig. 5.1.

5.3   P phase

5.3.1   Condensate and excitation spectrum

The P phase occurs for both $c_1 > 0$ and $c_1 < 0$ [see Figs. 2.2(a),(b)]. In this phase the condensate is unmagnetized and occupies the $m_F = 0$ level, with normalised spinor

$$\boldsymbol{\xi}^{\mathrm{P}} = [0, 1, 0]^T. \tag{5.13}$$

The nematic tensor [see Eq. (2.30)] for $\boldsymbol{\xi}^{\mathrm{P}}$ is

$$q^{\mathrm{P}} = n \begin{pmatrix} 1 & 0 & 0 \\ 0 & 1 & 0 \\ 0 & 0 & 0 \end{pmatrix}. \tag{5.14}$$

The most general form of the P phase spinor is obtained by applying an arbitrary gauge transformation and a spin rotation about the z-spin axis to $\boldsymbol{\xi}^{\mathrm{P}}$ (see Fig 5.5).

Because the P phase is axially symmetric these transformations leave the properties of the condensate, and its fluctuations, unchanged.
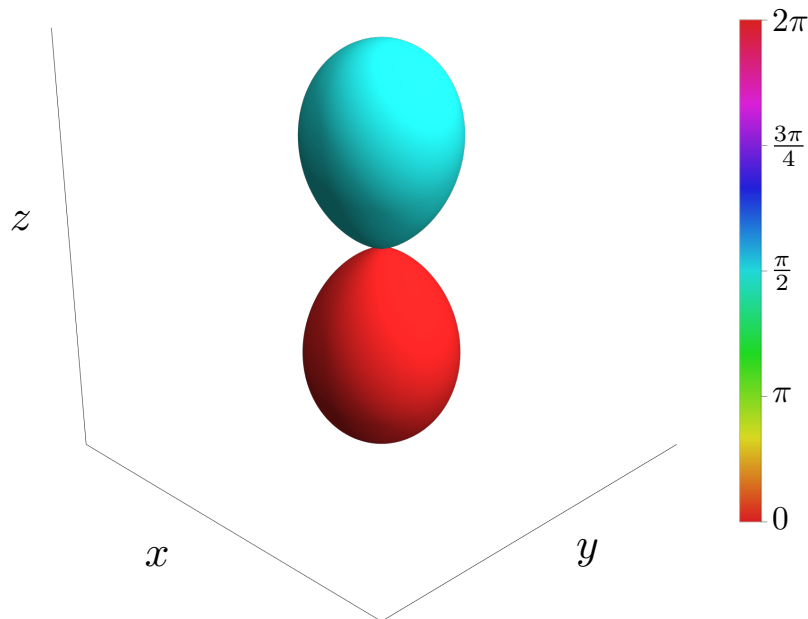

Figure 5.5: Surface plot of the spherical harmonic representation of the P spinor in spin-space [see Eq. (2.27)], coloured according to phase. Note the full axial symmetry about the z spin axis.

An example of the excitation spectrum for the P state [28] is shown in Fig. 5.6. This spectrum is similar to the F phase [Fig. 5.1] in that it has a phonon (index $\nu = 0$) and two gapped magnon branches (indices $\nu = 1, 2$). The magnon gaps depend on the magnetic field and are given by

$$E_{\mathrm{g},1}^{\mathrm{P}} = \sqrt{q(q + 2c_1 n)} - p, \tag{5.15}$$

$$E_{\mathrm{g},2}^{\mathrm{P}} = \sqrt{q(q + 2c_1 n)} + p, \tag{5.16}$$

for $\nu = 1$ and 2, respectively. The $\nu = 1$ magnon mode is of the form

$$\mathbf{u}_{\mathbf{k}1}^{T} = [u, 0, 0], \tag{5.17}$$

$$\mathbf{v}_{\mathbf{k}1}^{T} = [0, 0, v], \tag{5.18}$$

while the $\nu = 2$ magnon mode has

$$\mathbf{u}_{\mathbf{k}2}^{T} = [0, 0, u], \tag{5.19}$$

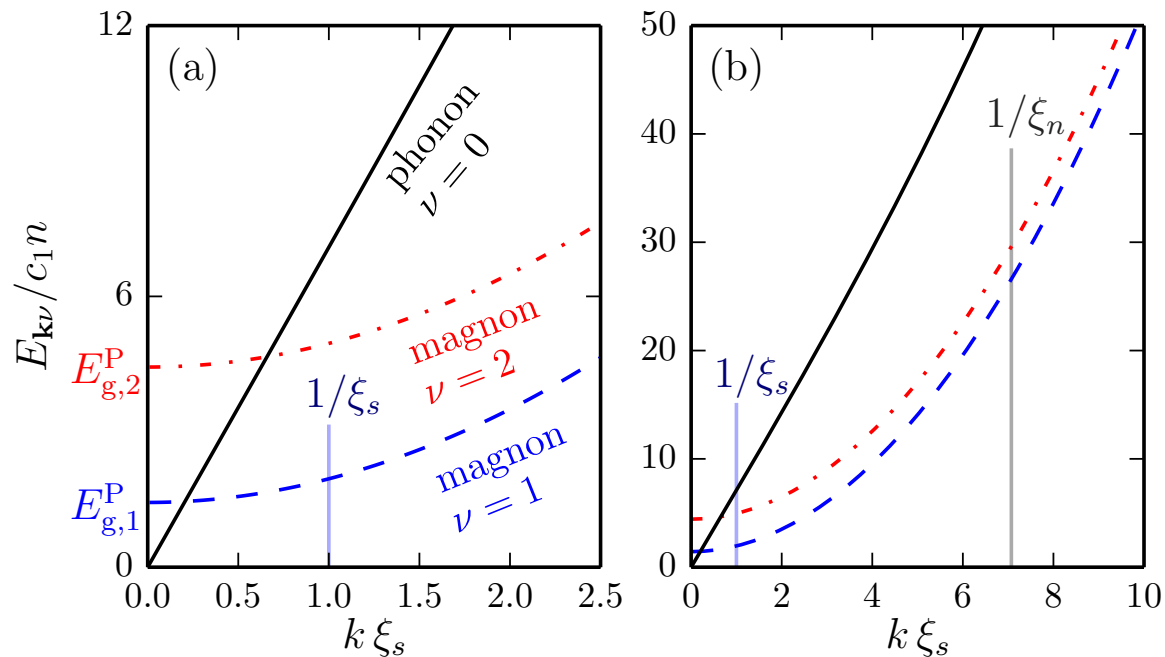$$\mathbf{v}_{\mathbf{k}2}^{T} = [v, 0, 0]. \tag{5.20}$$

Figure 5.6: Bogoliubov dispersion relations in the P phase. Subplots (a) and (b) focus on different ranges of k values. We show the branches of the excitation spectra for the phonon mode (black solid line) and the two magnon modes as (blue dashed line) and (red dash-dot line). Parameters: $q = 2.1 \, c_1 n$, $c_0 = 50 \, c_1$ and $p = 1.5 \, c_1 n$, $c_1 > 0$.

The phonon mode resides entirely in the $m_F = 0$ component and corresponds identically to that of a scalar gas with an effective interaction of c_0.

5.3.2   Fluctuations in n and f_z

Because the condensate resides entirely in the $m_F = 0$ level we have that the f_z fluctuations are identically zero [from Eq. (4.11)] to the level of approximation we work at here, with the leading order term coming from the small terms we neglected in Eq. (4.10). We do not consider a higher order treatment here, and take the f_z fluctuations to be zero.

The density fluctuations are entirely due to the phonon mode, which resides in $m_F = 0$, with no contribution from either of the magnon modes [see Fig. 5.7(a)] . The associated static structure factor is shown in Fig. 5.8(a) for several temperatures, with analytic limiting results given in Table 4.2.

5.3.3 Fluctuations in f_x and f_y

Because the P phase is axisymmetric, the f_x and f_y fluctuations are identical, and relevant fluctuation amplitudes are shown in Fig. 5.7(b). These results show that both magnon modes contribute equally. The associated structure factors are shown in Fig. 5.8(b), with analytic limiting results given in Table 4.2. Similar to the S_x and S_y structure factors considered for the F phase, these are also gapped at $k \to 0$ and at zero temperature.
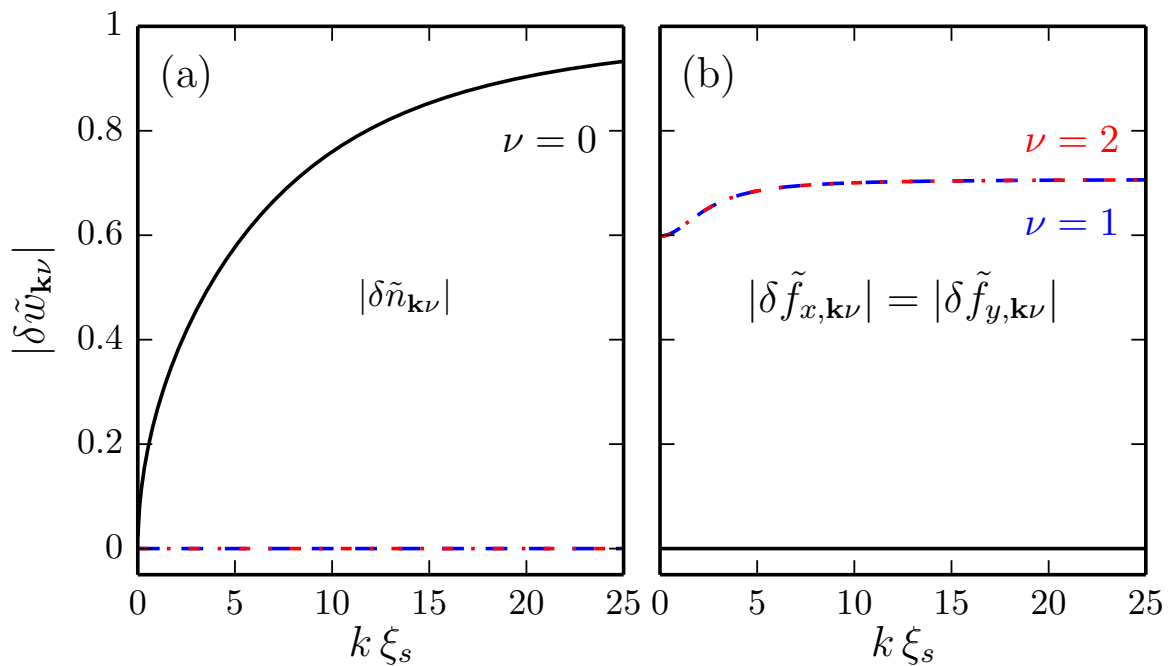
Figure 5.7: Fluctuation amplitudes for the P phase. Subplots (a) $\delta\tilde{n}_{\mathbf{k}\nu}$, (b) $\delta\tilde{f}_{x,\mathbf{k}\nu}$, $\delta\tilde{f}_{y,\mathbf{k}\nu}$, as defined in Eq. (4.11). Note $\delta\tilde{f}_{z,\mathbf{k}\nu} = 0$. The modes (index ν) have the same line types as in Fig. 5.6. Other parameters as in Fig. 5.6.
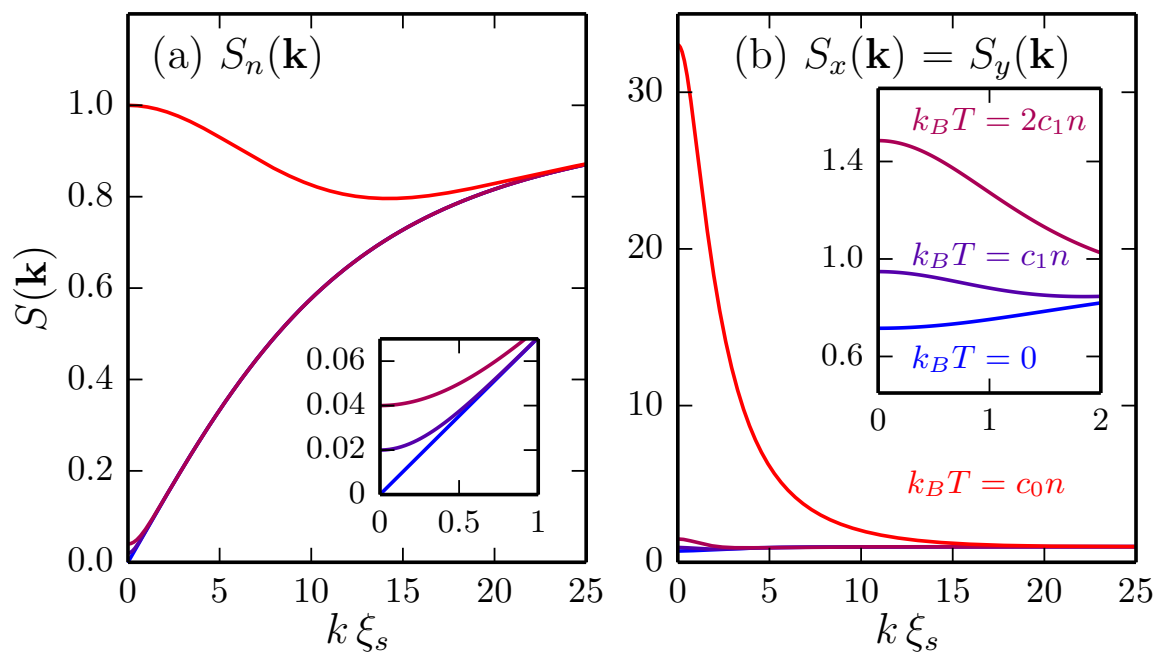
Figure 5.8: Static structure factors for the P phase at various temperatures. Structure factors (a) S_n, (b) S_x, S_y, as defined in Eq. (4.15). Note $S_z = 0$. For temperatures of (from bottom to top curves) $T = \{0, c_1, 2c_1, c_0\} \times n/k_B$, as labelled in the inset to (b). Insets reveal additional detail for small $k\xi_s$. Other parameters as in Fig. 5.6.

5.4 AF phase

5.4.1 Condensate and excitation spectrum

The AF phase occurs only for $c_1 > 0$ [see Fig. 2.2(a)]. In this phase the condensate takes the form

$$\boldsymbol{\xi}^{\mathrm{AF}} = \left[\sqrt{\tfrac{1}{2}(1 + f_z/n)}, 0, \sqrt{\tfrac{1}{2}(1 - f_z/n)} \right]^T, \qquad (5.21)$$

and has a z-component of magnetization given by

$$f_z = p/c_1, \qquad (5.22)$$

for $|p| \leq c_1 n$. The AF state breaks symmetry about the z axis, as can be seen from its nematic tensor [see Eq. (2.30)]

$$q^{\mathrm{AF}} = n \begin{pmatrix} \tfrac{1}{2}(1 + \alpha_z) & 0 & 0 \\ 0 & \tfrac{1}{2}(1 - \alpha_z) & 0 \\ 0 & 0 & 1 \end{pmatrix}, \qquad (5.23)$$

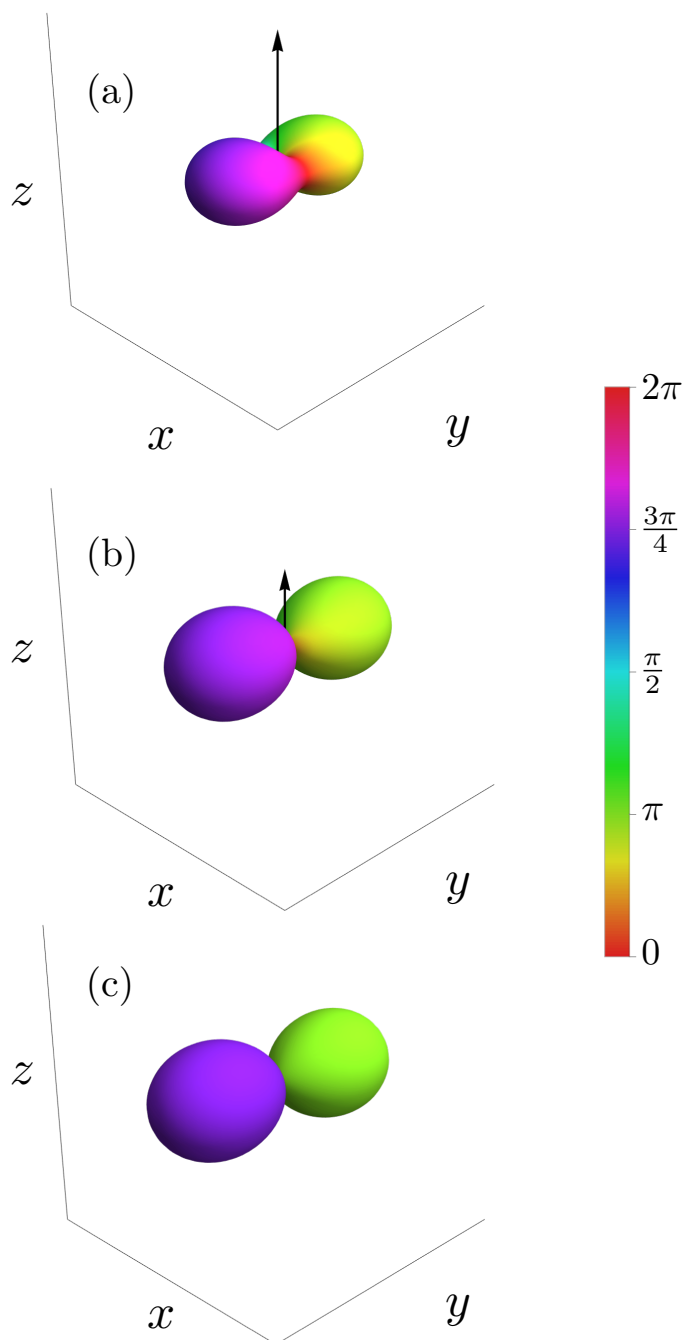where α is defined in Eq. (2.26).

Figure 5.9: Surface plot of the spherical harmonic representation of the AF spinor in spin-space [see Eq. (2.27)], coloured according to phase. Subplots are: (a) $f_z/n = 0.9$, (b) $f_z/n = 0.5$ and (c) $f_z/n = 0$. Note the broken symmetry about the z-axis, even though the magnetization is fully aligned – as discussed in the text, the broken symmetry arises in the nematic tensor rather than the magnetization vector.

We note that q^{AF} corresponds to q^{F} (5.2) in the limit of a fully magnetized AF state (i.e. $f_z \to n$). The most general form of the AF phase spinor is obtained by applying an arbitrary gauge transformation and a spin rotation about the z-spin axis to $\boldsymbol{\xi}^{\mathrm{AF}}$. We note that the spin rotation changes the orientation of the nematic distortion in the spin xy-plane (see Fig. 5.9).

An example of the AF excitation spectrum [28] is shown in Fig. 5.10. It has phonon (index $\nu = 0$), axial magnon (index $\nu = 1$), and transverse magnon (index $\nu = 2$) branches. The AF phase has two broken continuous symmetries giving rise to two Nambu-Goldstone modes: in addition to the phonon mode arising from the broken $U(1)$ symmetry of the condensate, the broken axial spin symmetry (revealed by the nematic tensor) yields a massless axial magnon mode. The axial magnon dispersion mode crosses over from having a linear to quadratic dependence on k at a wavevector of $k \sim 1/\xi_s$, whereas the phonon mode crosses over at $k \sim 1/\xi_n$. The transverse magnon mode has an energy gap of

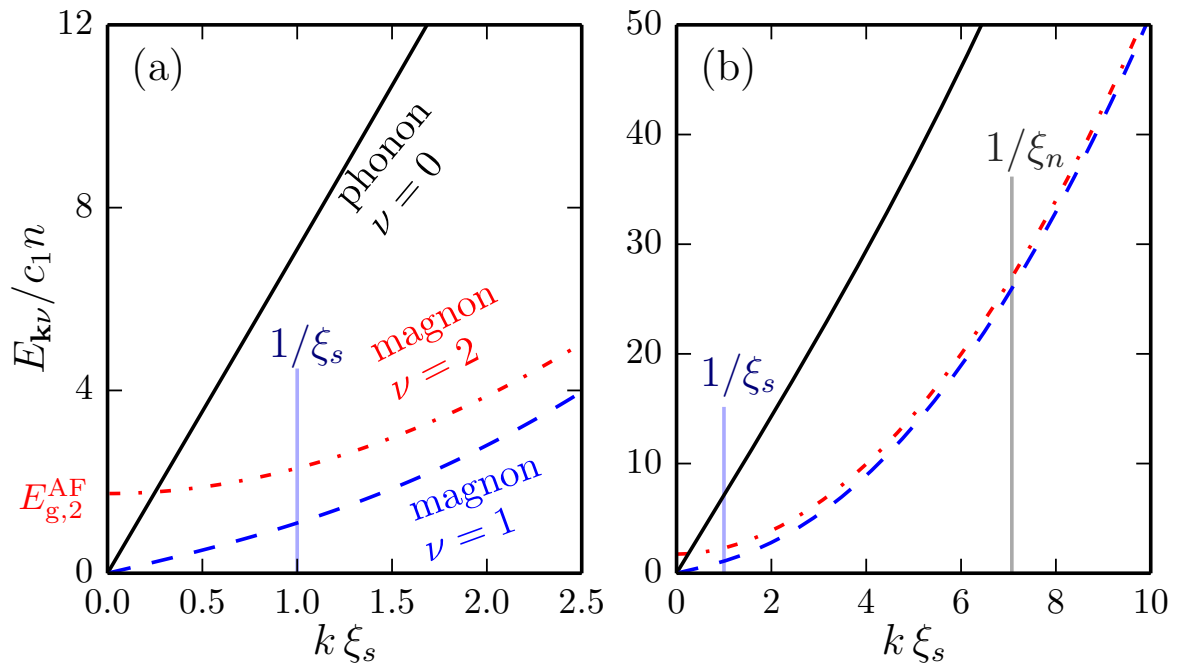$$E_{\mathrm{g},2}^{\mathrm{AF}} = c_1 n \sqrt{(1 - q/c_1 n)^2 - \alpha_z^2}. \tag{5.24}$$

Figure 5.10: Bogoliubov dispersion relations in the AF phase. Subplots (a) and (b) focus on different ranges of k values. We show the phonon (black solid line), axial magnon (blue dashed line), and transverse magnon (red dash-dot line) branches of the excitation spectra, and attribute these the indices $\nu = 0, 1, 2$, respectively. Parameters: $q = -c_1 n$, $c_0 = 50\,c_1$ and $p = 0.2\,c_1 n$, giving $f_z = 0.2\,n$, $\alpha_z \approx 0.98$.
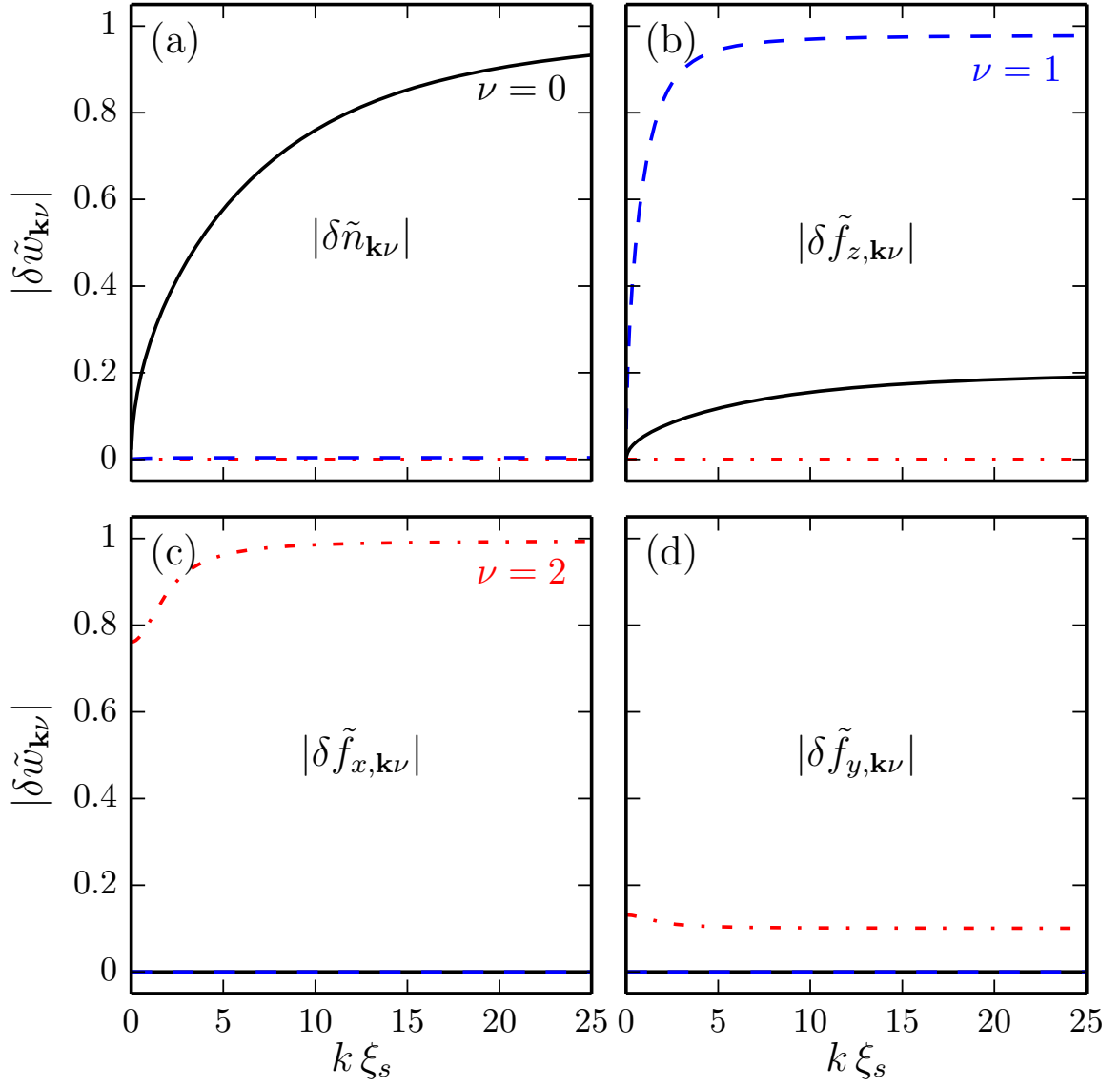
Figure 5.11: Fluctuation amplitudes for the AF phase. Subplots (a) $\delta\tilde{n}_{\mathbf{k}\nu}$, (b) $\delta\tilde{f}_{z,\mathbf{k}\nu}$, (c) $\delta\tilde{f}_{x,\mathbf{k}\nu}$, (d) $\delta\tilde{f}_{y,\mathbf{k}\nu}$, as defined in Eq. (4.11). The modes (index ν) have the same line types as in Fig. 5.10. Other parameters as in Fig. 5.10.
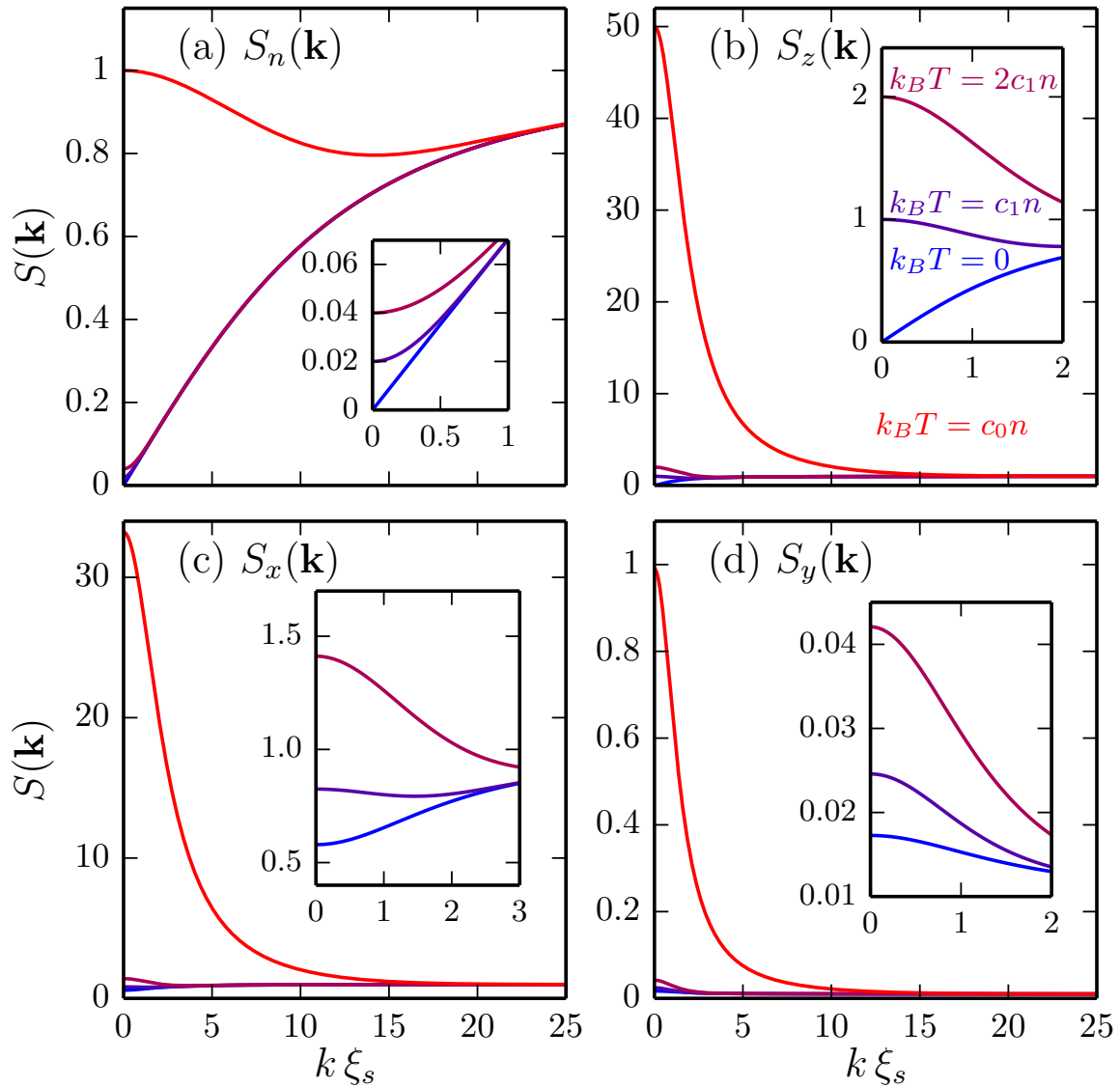
Figure 5.12: Static structure factors for the AF phase at various temperatures. Structure factors (a) S_n, (b) S_z, (c) S_x, (d) S_y, as defined in Eq. (4.15). For temperatures of (from bottom to top curves) $T = \{0, c_1, 2c_1, c_0\} \times n/k_B$, as labelled in the inset to (b). Insets reveal the lower temperature results at small $k\xi_s$. Other parameters as in Fig. 5.10.

5.4.2 Fluctuations in n

The density fluctuation amplitudes $\delta\tilde{n}_{\mathbf{k}\nu}$ are shown in Fig. 5.11(a). These results demonstrate that the density fluctuations are dominated by the phonon mode, although a weak contribution arises from the axial magnon mode. This magnon contribution increases as c_1 increases relative to c_0 and also depends on the axial magnetization f_z (note: the axial magnon and phonon modes decouple for $f_z = 0$, and at this point the magnon mode does not contribute to $\delta\tilde{n}_{\mathbf{k}\nu}$).

The density static structure factor (S_n) is shown in Fig. 5.12(a) for several temperatures. This behavior is similar to that of the density static structure factor in the F phase, except that the phonon speed of sound varies between the value set by $c_0 n$ and $(c_0 + c_1)n$ depending on f_z.

5.4.3 Fluctuations in f_z

The axial spin fluctuation amplitudes $\delta\tilde{f}_{z,\mathbf{k}\nu}$ are shown in Fig. 5.11(b), and demonstrate a dominant contribution from the axial magnon mode, and a smaller, but appreciable contribution from the phonon mode. The associated static structure factor (S_z) is shown in Fig. 5.12(b). The general behavior is similar to the density fluctuation case, but with the much smaller spin-dependent energy $c_1 n$ being the appropriate energy scale. Thus the fluctuations are more easily thermally activated and the uncorrelated limit [$S_z(\mathbf{k}) \to 1$] is reached at lower wave vectors $k \gg 1/\xi_s$ [also see Table 4.2].

5.4.4 Fluctuations in f_x and f_y

The transverse spin fluctuation amplitudes, i.e. $\delta\tilde{f}_{x,\mathbf{k}\nu}$ and $\delta\tilde{f}_{y,\mathbf{k}\nu}$, are shown in Figs. 5.11(c) and (d), respectively. Only the transverse magnon mode contributes to these. The difference in the behavior of $\delta\tilde{f}_{x,\mathbf{k}\nu}$ and $\delta\tilde{f}_{y,\mathbf{k}\nu}$ reveals the broken symmetry of the AF state about the z-spin axis [c.f. Eq. (5.23)].

The associated structure factors are shown in Figs. 5.12(c) and (d). Similar to the S_x and S_y structure factors for the F and P phases, these also have a non-zero value for $k \to 0$ at $T = 0$. The energy gap of the transverse magnon mode delays the onset of thermal fluctuations to temperatures $T \gtrsim E_{g,2}^{AF}/k_B$.

5.5 BA phase

5.5.1 Condensate and excitation spectrum

The BA phase occurs for $c_1 < 0$ [see Fig. 2.2(b)], and in this phase the condensate occupies all three m_F states. The results we present here are for the case of $p = 0$, where the magnetization is purely transverse (i.e. $f_z = 0$). This case has the advantage that it affords a simpler analytic treatment [66, 72], allowing us to write the spinor as

$$\boldsymbol{\xi}^{\mathrm{BA}} = \left[\tfrac{1}{2}\sqrt{1-\tilde{q}}, \sqrt{\tfrac{1}{2}(1+\tilde{q})}, \tfrac{1}{2}\sqrt{1-\tilde{q}}\right]^T, \tag{5.25}$$

where $\tilde{q}$ is defined in Eq. (2.25). For our choice of a real spinor $\boldsymbol{\xi}^{\mathrm{BA}}$, the magnetization is along the x-spin axis. The most general form of the BA phase spinor is given by an arbitrary gauge transformation and spin rotation about z-spin axis applied to $\boldsymbol{\xi}^{\mathrm{BA}}$. The nematic tensor for $\boldsymbol{\xi}^{\mathrm{BA}}$ [see Eq. (2.30)] is

$$q^{\mathrm{BA}} = n \begin{pmatrix} 1 & 0 & 0 \\ 0 & \tfrac{1}{2}(1+\tilde{q}) & 0 \\ 0 & 0 & \tfrac{1}{2}(1-\tilde{q}) \end{pmatrix}, \tag{5.26}$$

which reveals the broken symmetry of the BA state about the z axis (see Fig. 5.13) due to the transverse magnetization,

$$f_\perp = f_x = \sqrt{1 - \tilde{q}^2}, \tag{5.27}$$

where $f_\perp$ is defined in Eq. (2.23).

The Bogoliubov excitations of the BA phase have been investigated in several recent papers [66, 72] (also see Appendix of [49]).[3] The excitations of the BA phase at $p = 0$ are shown in Fig. 5.14. Because the BA phase has two broken continuous symmetries, the system has two gapless Nambu-Goldstone modes: a phonon branch (index $\nu = 0$) and a transverse magnon branch (index $\nu = 1$). These two modes are decoupled at $p = 0$. The transverse magnon has the energy dispersion [66]

$$E_{\mathbf{k}1} = \sqrt{\epsilon_{\mathbf{k}}(\epsilon_{\mathbf{k}} + q)}, \tag{5.28}$$

i.e. independent of the interaction parameters, where the free particle energy is defined in Eq. (3.16). Since the quadratic Zeeman sets the relevant energy scale for this magnon, we define an associated length scale

$$\xi_q \equiv \hbar/\sqrt{Mq}. \tag{5.29}$$

---

[3]While various analytic results have been reported for the $p = 0$ case [66], the understanding of the $p \neq 0$ case is based largely on numerical results [72].
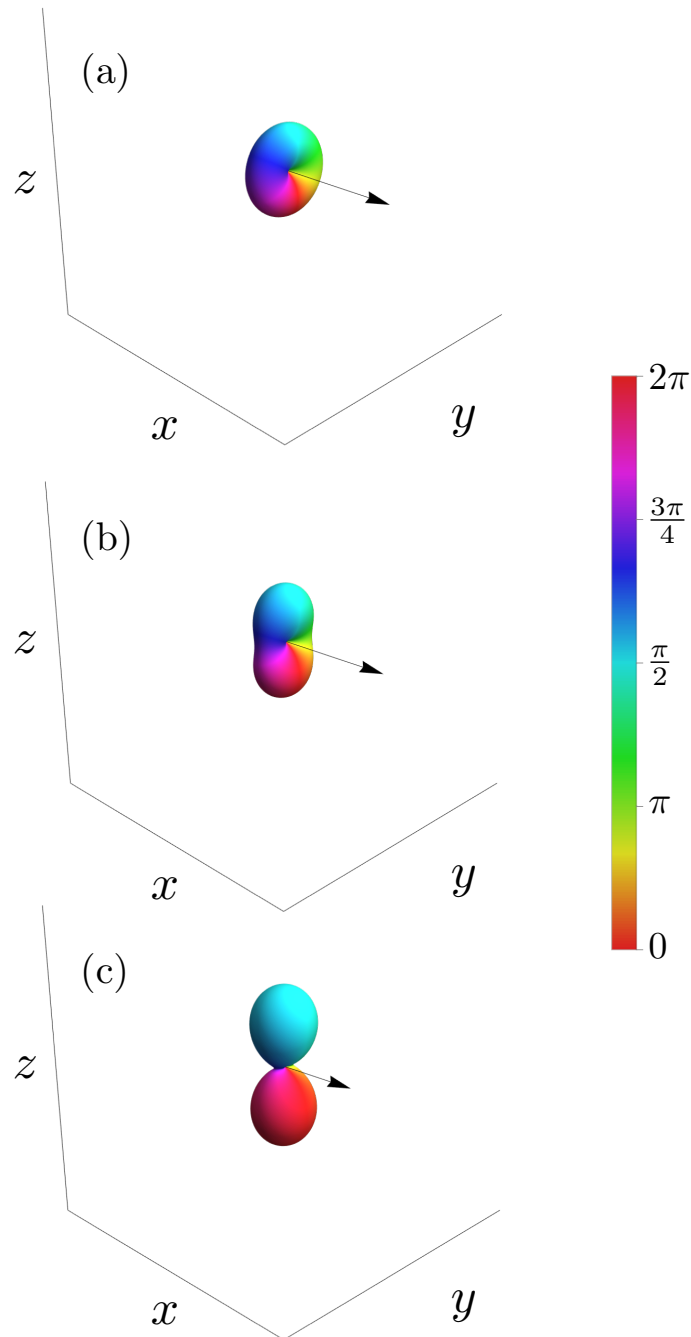
Figure 5.13: Surface plot of the spherical harmonic representation of the BA spinor in spin-space [see Eq. (2.27)], coloured according to phase. Subplots are: (a) $q = 0.01|c_1|n$, (b) $q = 0.5|c_1|n$ and (c) $q = 1.5|c_1|n$. Here, axial symmetry is broken by the magnetization vector and also by the nematic tensor (see text). As $q \to 0$ the spinor looks like a rotated F spinor, while for $\tilde{q} \to 1$ it becomes the P spinor.

The last branch (index $\nu = 2$) is a magnon excitation with energy gap

$$E_{g,2}^{BA} = 2|c_1|n\sqrt{1 - \tilde{q}^2} = 2f_x|c_1|n. \tag{5.30}$$

This gapped magnon does couple to the phonon branch, and they have an avoided crossing, as revealed in Fig. 5.14(a) and inset. We have chosen to switch the labelling either side of this crossing to match the labelling choice made in Ref. [72] and also to ensure that away from the crossing the $\nu = 0$ mode has phonon character (i.e. a dominant effect on density fluctuations). The coupling between these two modes is small so that the avoided crossing occurs over a narrow range of k vectors, with the energy gap between these branches being

$$\Delta_C = q\sqrt{1 - \tilde{q}^2}\sqrt{\frac{|c_1|}{c_0}}, \tag{5.31}$$
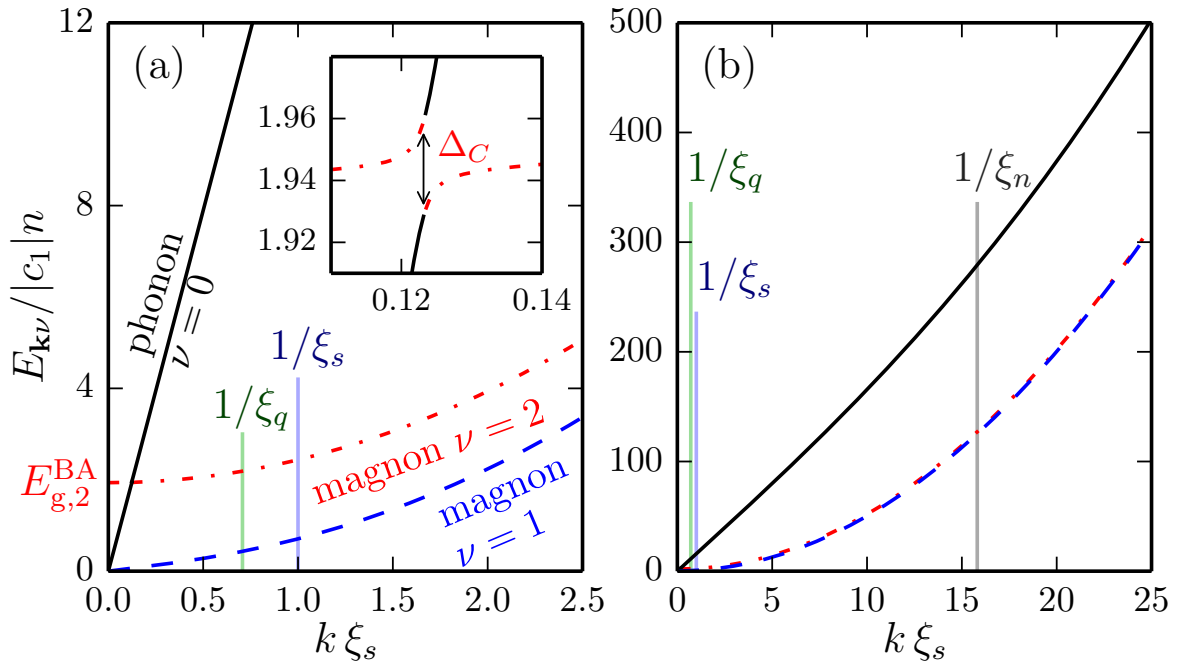
to lowest order in c_1/c_0.

Figure 5.14: Bogoliubov dispersion relations in the BA phase. Subplots (a) and (b) focus on different ranges of k values. We show the branches of the excitation spectra for the phonon mode (black solid line) and the axial (blue dashed line, note the magnetization axis is x) and transverse (red dash-dot line) magnon modes. Inset to (a) reveals an avoided crossing between the phonon and transverse magnon modes. Parameters: $q = 0.5\,|c_1|n$, $c_0 = -250\,c_1$, $p = 0$ and $c_1 < 0$.
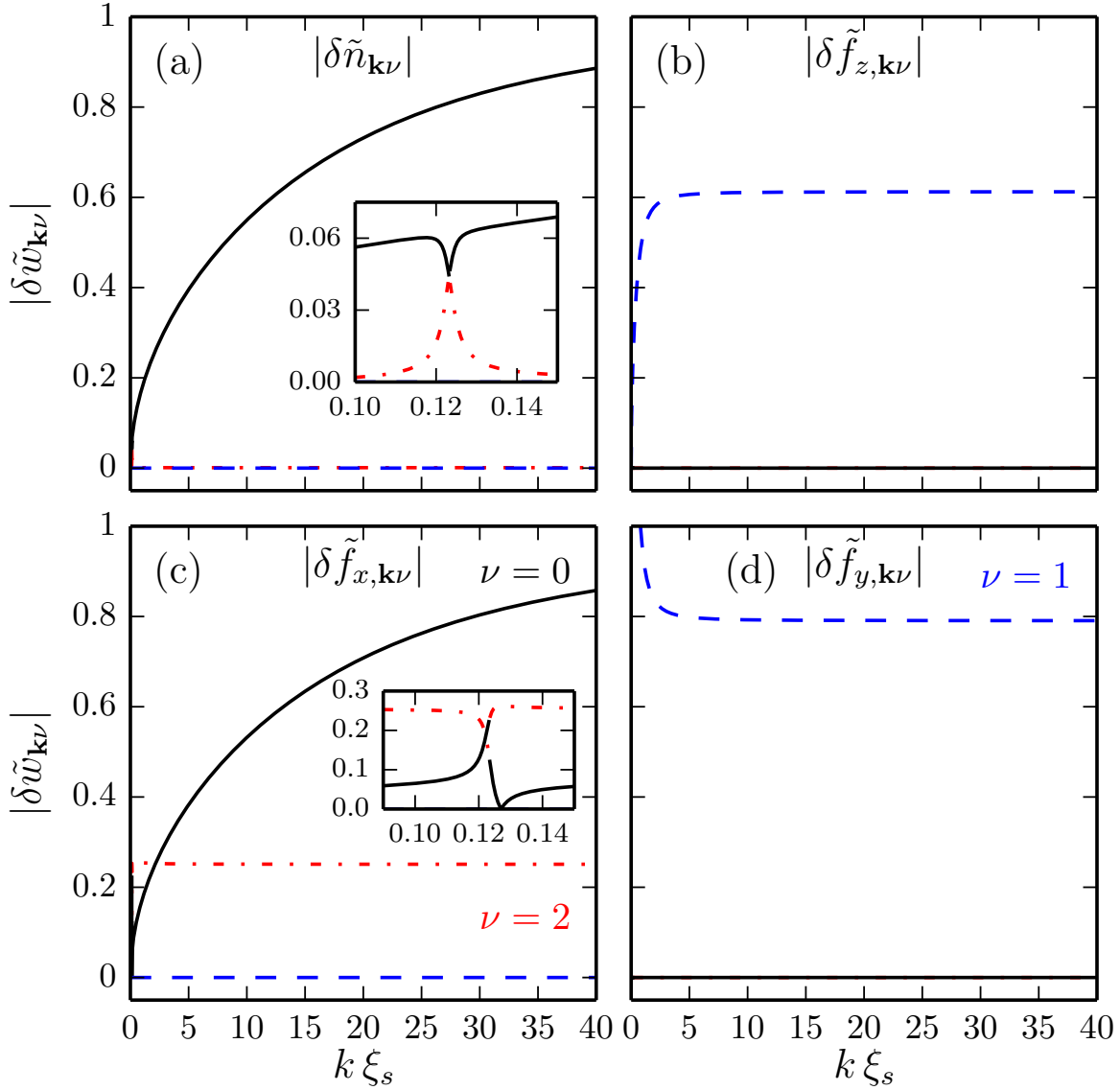
Figure 5.15: Fluctuation amplitudes for the BA phase. Subplots (a) $\delta\tilde{n}_{\mathbf{k}\nu}$, (b) $\delta\tilde{f}_{z,\mathbf{k}\nu}$, (c) $\delta\tilde{f}_{x,\mathbf{k}\nu}$, (d) $\delta\tilde{f}_{y,\mathbf{k}\nu}$, as defined in Eq. (4.11). The modes (index ν) have the same line types as in Fig. 5.14. Insets to (a) and (c) reveal additional detail for $k\xi_s$ close to the avoided crossing. Other parameters as in Fig. 5.14.
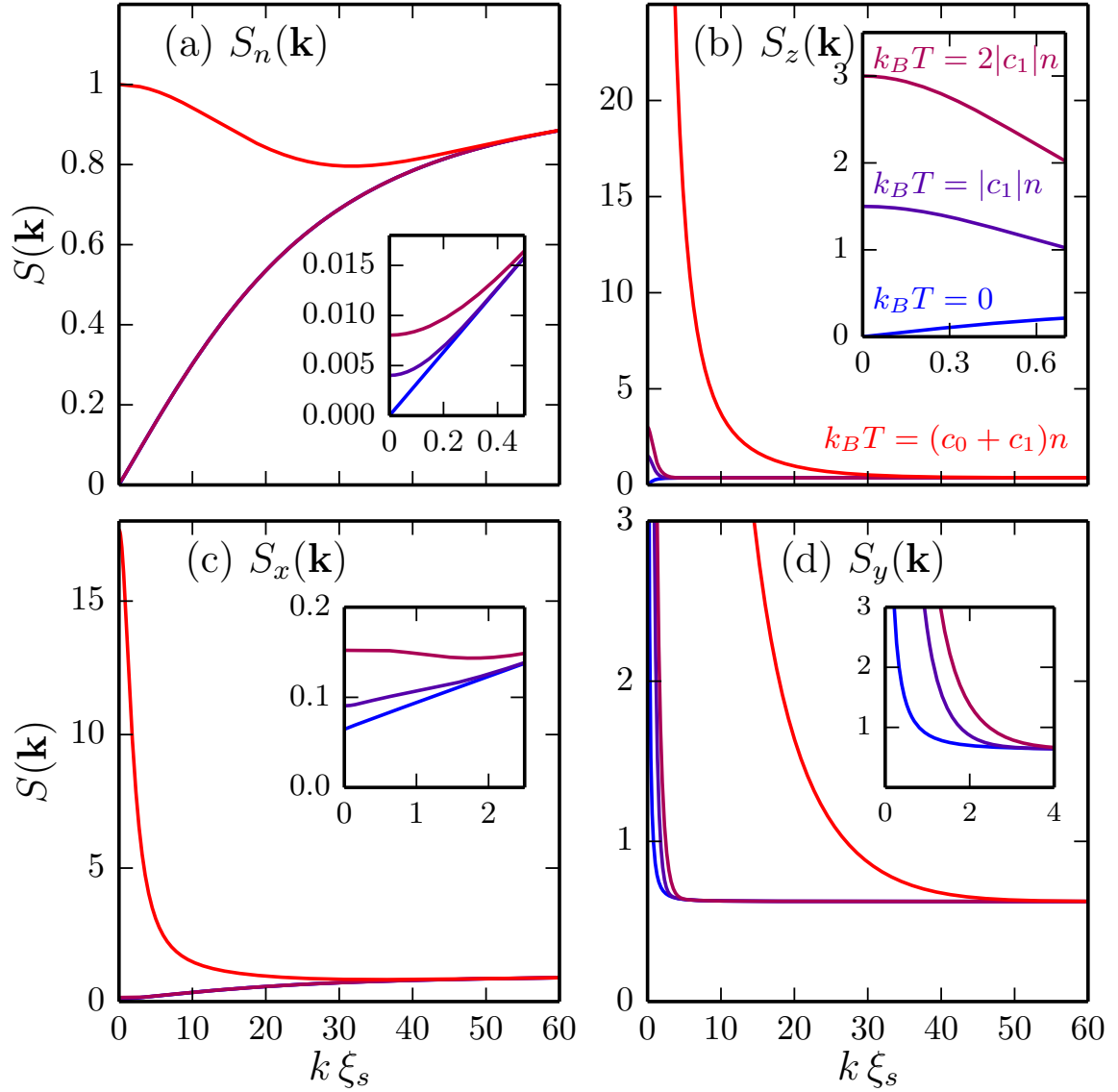
Figure 5.16: Static structure factors for the BA phase at various temperatures. Structure factors (a) S_n, (b) S_z, (c) S_x, (d) S_y, as defined in Eq. (4.15). For temperatures of (from bottom to top curves) $T = \{0, |c_1|, 2|c_1|, c_0 + c_1\} \times n/k_B$, as labelled in the inset to (b). Insets reveal additional detail for small $k\xi_s$. Other parameters as in Fig. 5.14.

5.5.2 Fluctuations in n and f_z

From Fig. 5.15(a) we see that the dominant contribution to density fluctuations comes from the phonon mode, although a contribution from the (gapped) axial magnon mode occurs near the avoided crossing noted in the spectrum.[4] In contrast the f_z fluctuations come entirely from the (Nambu-Goldstone) transverse magnon branch ($\nu = 1$) [see Fig. 5.15(b)].

The structure factors S_n and S_z are shown in Fig. 5.16(a) and (b), respectively, with analytic expressions for the limiting behavior provided in Table 4.2. Interestingly, the long wavelength fluctuations of the z component of magnetization is set by the quadratic Zeeman energy, i.e.

$$S_z(0) = (1 - \tilde{q})\frac{k_B T}{q}. \tag{5.32}$$

This diverges for $q \to 0$ as the full spin rotational symmetry $[SO(3)]$ is restored (noting we have set $p = 0$).

5.5.3 Fluctuations in f_x and f_y

Because the magnetization lies along x for our choice of p and $\boldsymbol{\xi}^{\mathrm{BA}}$, fluctuations in f_x correspond to fluctuations in the length of the magnetization. Fig. 5.15(c) reveals that both the gapped magnon mode and the phonon mode contribute to these fluctuations. In contrast, fluctuations in f_y are orthogonal to the direction of magnetization and act to restore the axial symmetry $[SO(2)]$ of the Hamiltonian. In Fig. 5.15(d) we see that these fluctuations are entirely due to the (Nambu-Goldstone) transverse magnon mode, and that these fluctuations diverge as $k \to 0$. The divergence is clearly apparent in S_y [see Fig. 5.16(d)], and is seen to go as k^{-2} for small k at finite temperature [see Table 4.2].

---

[4]The rapid variation in $\{\delta\tilde{n}_{\mathbf{k}0}, \delta\tilde{n}_{\mathbf{k}2}\}$ and $\{\delta\tilde{f}_{x,\mathbf{k}0}, \delta\tilde{f}_{x,\mathbf{k}2}\}$ for $k \approx 0.12/\xi_s$ occurs because the phonon and transverse magnon hybridize near the anti-crossing. We emphasise that summed contribution of these fluctuations to the relevant structure factors is smooth.

5.5.4 BA phase for $p \neq 0$

We conclude by briefly commenting on the qualitative behavior for $p \neq 0$. In this case the condensate magnetization tilts out of the xy-plane and the Nambu-Goldstone branches (i.e. $\nu = 0$ and $\nu = 1$ branches) become coupled (c.f. at $p = 0$ where the only coupling is between the $\nu = 0$ and $\nu = 2$ branches, giving rise to the avoided crossing). In Ref. [72] this occurrence was referred to as phonon-magnon coupling. As a result of this coupling the $\nu = 1$ mode contributes to density fluctuations, and the $\nu = 0$ mode contributes to the f_z fluctuations.

Chapter 6

Measuring fluctuations in finite cells

In this Chapter we apply our understanding of structure factors to a concrete experimental system of a quasi-2D spinor condensate. We consider making experimental measurements of this system; specifically, measuring the number of atoms or a total spin component within a measurement cell of finite volume. The size and shape of the measurement cell is an important consideration because it affects which parts of a structure factor contribute to fluctuations within the cell. We also explore the various limiting cases that exist for different sized cells independent of their precise shape. We present comprehensive analytic limit results, and compare them with full numerical solutions in all four magnetic ground state phases.

6.1   General theory

Let us consider making measurements in a localised region of space of a spin-1 Bose-Einstein condensate with observables that can be expressed as

$$\hat{W}_\sigma \equiv \int d^D\mathbf{x}\; \sigma(\mathbf{x})\hat{w}(\mathbf{x}), \tag{6.1}$$

where the weight function $\sigma(\mathbf{x})$ describes the localised cell in which the measurement is made and $\hat{w}(\mathbf{x})$ is a generalized density operator of interest as defined in Eq. (4.1) [also see Fig. 6.1].

The variance in $\hat{W}_\sigma$ is given by

$$\Delta W_\sigma^2 \equiv \langle \hat{W}_\sigma^2 \rangle - \langle \hat{W}_\sigma \rangle^2. \tag{6.2}$$
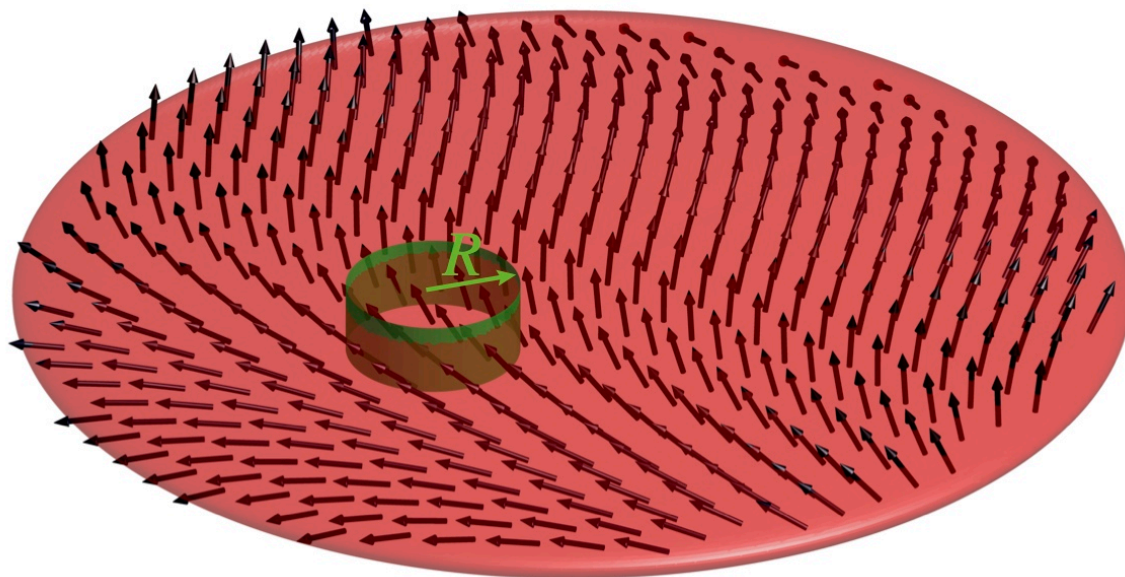
Figure 6.1: Schematic illustration of fluctuation measurement for a quasi-2D spinor condensate. Within a small cell of radius R (e.g. a cylindrical cell, indicated by green boundary walls) an operator of interest is measured. For example, the total number of atoms or the total components of spin.

This can be evaluated as

$$\Delta W_\sigma^2 = \int d^D\mathbf{x} \int d^D\mathbf{x}'\, \sigma(\mathbf{x})\sigma(\mathbf{x}') \left\langle \delta\hat{w}(\mathbf{x})\delta\hat{w}(\mathbf{x}')\right\rangle, \tag{6.3}$$

where the fluctuation operator $\delta\hat{w}(\mathbf{x}) = \hat{w}(\mathbf{x}) - w$ was defined in Eq. (4.4). The correlation function appearing in Eq. (6.3) is the same as the one defined in Eq. (4.3), i.e.

$$\left\langle \delta\hat{w}(\mathbf{x})\delta\hat{w}(\mathbf{x}')\right\rangle = C_w(\mathbf{x} - \mathbf{x}'). \tag{6.4}$$

For the homogeneous system, it depends only on the relative separation $\mathbf{r}$. This means we can carry out the first of the two spatial integrals in Eq. (6.3) to get

$$\Delta W_\sigma^2 = \int d^D\mathbf{x} \int d^D\mathbf{x}'\, \sigma(\mathbf{x})\sigma(\mathbf{x}')C_w(\mathbf{x} - \mathbf{x}') = \int d^D\mathbf{r}\, \tau_\sigma(\mathbf{r})C_w(\mathbf{r}), \tag{6.5}$$

where we have defined the *geometry function*

$$\tau_\sigma(\mathbf{r}) \equiv \int d^D\mathbf{x} \int d^D\mathbf{x}'\, \sigma(\mathbf{x})\sigma(\mathbf{x}')\delta(\mathbf{x} - \mathbf{x}' - \mathbf{r}). \tag{6.6}$$

We can then Fourier transform to get

$$\Delta W_\sigma^2 = n \int \frac{d^D\mathbf{k}}{(2\pi)^D} S_w(\mathbf{k})\tilde{\tau}_\sigma(\mathbf{k}), \tag{6.7}$$

where

$$\tilde{\tau}_\sigma(\mathbf{k}) = \left| \int d^D\mathbf{x}\, e^{-i\mathbf{k}\cdot\mathbf{x}}\sigma(\mathbf{x}) \right|^2, \tag{6.8}$$

is the Fourier space geometry function of the cell σ, $n = N/V$ and $S_w(\mathbf{k})$ is the w static structure factor as defined previously in Eq. (4.7).

6.2 Cell weight function

The integral of the weight function

$$V_\sigma = \int d^D\mathbf{x}\, \sigma(\mathbf{x}), \tag{6.9}$$

defines the D-dimensional effective volume of the cell. To ensure that we get Poissonian number fluctuations for uncorrelated atoms, we set $N_\sigma = nV_\sigma$, and require that $\Delta N_\sigma^2 = N_\sigma$ when $S_n(\mathbf{k}) = 1$. This gives us

$$\Delta N_\sigma^2 = n \int \frac{d^D\mathbf{k}}{(2\pi)^D} S_n(\mathbf{k})\tilde{\tau}_\sigma(\mathbf{k}) = n\tau_\sigma(\mathbf{0}) = \frac{N_\sigma}{V_\sigma}\int d^D\mathbf{x}[\sigma(\mathbf{x})]^2, \tag{6.10}$$

which leads to the normalization condition of the weight function

$$V_\sigma = \int d^D\mathbf{x}\, \sigma(\mathbf{x}) = \int d^D\mathbf{x}\, [\sigma(\mathbf{x})]^2. \tag{6.11}$$

6.3 Quasi-2D system

We now specialize our theory to the $D = 2$ case of measurements made in effectively 2D cells in a quasi-2D system, specifically a spin-1 Bose gas in a harmonic trap with a so-called 'pancake' geometry, as schematically shown in Fig. 6.1. Such a system has been realized, along with precise number fluctuation measurements, for a scalar gas of Cs atoms in Cheng Chin's lab at Chicago [43].

The pancake trap geometry consists of a tight harmonic potential along the quantization axis (which we take to be the z-axis) and a weak 'in-plane' harmonic potential (which we take to be the $x - y$ plane). This system is physically three-dimensional, but if the z trap is strong enough then excitations in the z direction become energetically unreachable, and the system will become frozen in the harmonic oscillator ground state in the z direction.

We go through an analysis of this situation in Appendix A, and conclude that we can approximately treat the central condensate region using our general uniform spin-1 theory by choosing appropriate parameters. The appropriate parameters, which we will consider for the rest of this Chapter are the effective 2D interaction parameters c_0^{2D} and c_1^{2D}, the 2D areal peak density, and a chemical potential shifted by the z trap's energy.

We note that a BEC is technically forbidden from existing at finite temperature in an infinite 2D system [74, 75]. However, we can safely ignore finite-size effects as long as the fluctuation integral Eq. (6.7) converges in the limit that we integrate down to $k = 0$ (i.e. an infinite system).

6.4 Cells in a quasi-2D system

Experimental measurements of cold-atom systems are always limited in their resolution and thus encompass a finite measured volume instead of being precisely at one point in space. Here we discuss the two types of cell we consider to approximate such finite-resolution measurements of a quasi-2D gas, illustrated in Fig. 6.2.

(i) Cylindrical cell: contains all points (with equal weight) in a disc of fixed radius R from the cell centre as schematically indicated by the green cell boundary in Fig. 6.1. For this case we have

$$\sigma(\mathbf{x}) = \theta(R^2 - |\mathbf{x}|^2), \tag{6.12}$$

where θ is the Heaviside step function, giving a cell volume of $V_\sigma = \pi R^2$. The geometry function is

$$\tilde{\tau}_\sigma(\mathbf{k}) = \frac{4\pi^2 R^2 J_1^2(Rk)}{k^2}, \tag{6.13}$$

where J_1 is the first order Bessel function of the first kind. This type of *hard cell* has been considered in previous theoretical studies (e.g. see [48, 76–79]). Of particular relevance are the results of Klawunn *et al.* [78] for disc-shaped cells in a quasi-2D scalar condensate.

(ii) Gaussian cell: density contributions are weighted by distance from cell centre with Gaussian weight,

$$\sigma(\mathbf{x}) = 2\exp(-|\mathbf{x}|^2/R^2), \tag{6.14}$$

where R is the radial length scale over which the weighting falls by a factor of $1/e$, giving a cell volume of $V_\sigma = 2\pi R^2$. This cell shape approximates the effect of measurements made with a real imaging system of finite resolution (e.g. see [43–45]), with R being related to the resolution spot size. For this case

$$\tilde{\tau}_\sigma(\mathbf{k}) = 4\pi^2 R^4 e^{-k^2 R^2/2}. \tag{6.15}$$

6.5 Thermodynamic Limit

For sufficiently large cells $\tilde{\tau}_\sigma(\mathbf{k})$ becomes concentrated near $\mathbf{k} = \mathbf{0}$ and the fluctuations cross over to the thermodynamic limit expression

$$\Delta W_\sigma^2 \approx N_\sigma k_B T \chi_w, \tag{6.16}$$

where $N_\sigma = nV_\sigma$ is the average number of atoms in the cell and we have introduced a generalised static susceptibility,

$$\chi_w \equiv S_w(0)/k_B T. \tag{6.17}$$

This result is valid when the dimension R of the cell is much larger than any microscopic length scale of the system, i.e. healing and thermal length scales.
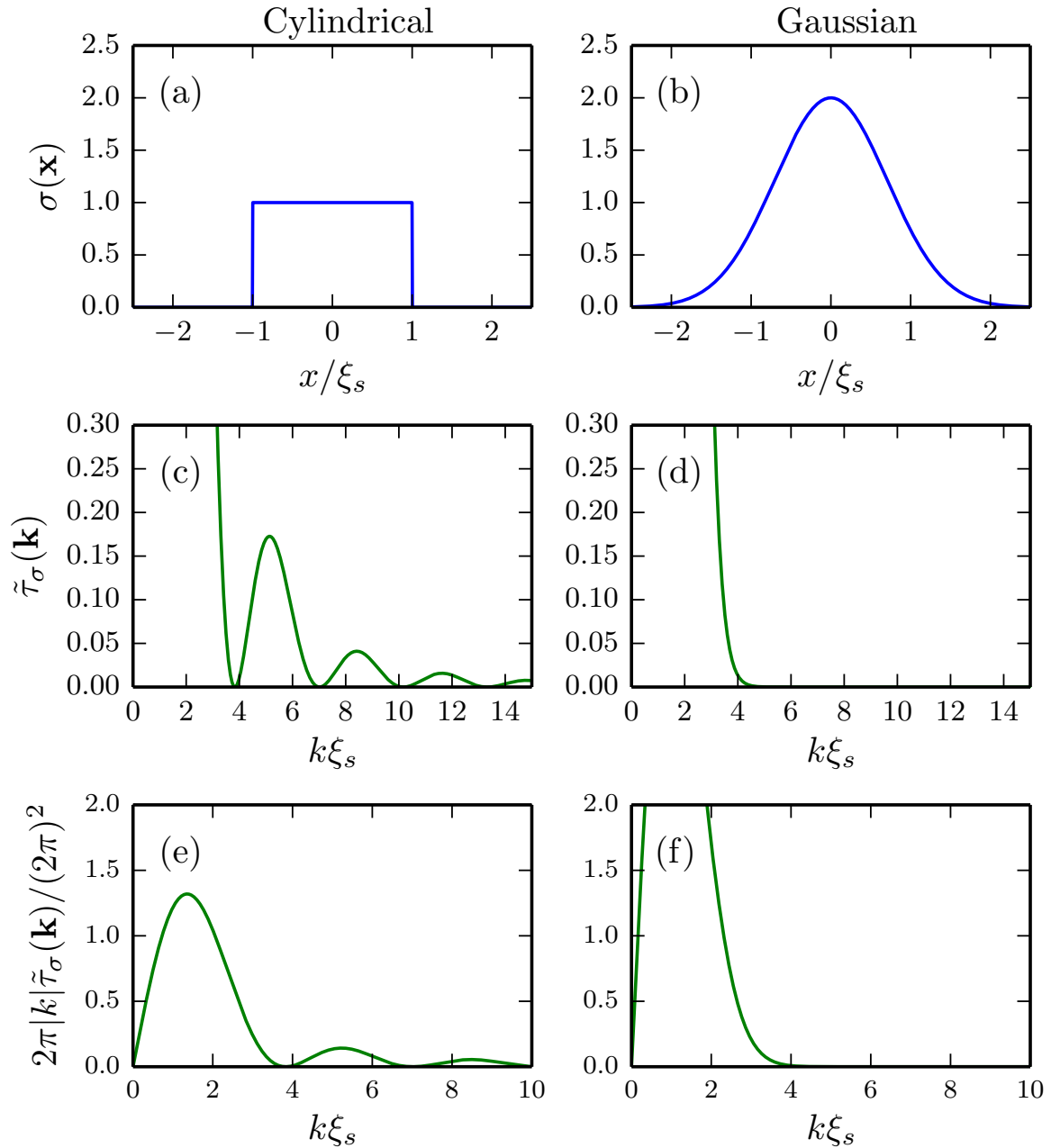
Figure 6.2: Weight and geometry functions for $R = 2\xi_s$. Subplots: (a) and (b) are weight functions, (c) and (d) are geometry functions (momentum space) and (e) and (f) are the geometry functions multiplied by the cylindrical Jacobian, $2\pi|k|$. Left and right columns are for cylindrical and gaussian cells, respectively. In (c) and (d) we see different decay rates – the cylindrical geometry function has a slow algebraic decay in momentum space ($\sim k^{-3}$), while the geometry function of gaussian cells decays exponentially.

6.6   Quantum Fluctuations: Small Cells

Classically, we expect all fluctuations to vanish at zero temperature. However, quantum mechanically, fluctuations persist. These *quantum* fluctuations are dominant in regimes where thermal effects can be neglected (i.e. here we take $T = 0$). It is convenient to treat large cells, where collective modes dominate, separately from small cells where we recover a quantum shot noise limit. Here we consider the small cell regime, and discuss the large cell case in the next section. The length scale ξ_L that defines the cross over between small and large cells depends on the phase and observable under consideration, and is also given in the next subsection (i.e. ξ_Q or ξ_E).

For $k \gg 1/\xi_L$ the structure factors approach the incoherent value [see Eq. (4.17)]

$$S_w(k \to \infty) = \boldsymbol{\xi}^\dagger \mathrm{W}^2 \boldsymbol{\xi}, \tag{6.18}$$

which is dependent on the condensate order parameter [c.f. the familiar result of $S_n(k \to \infty) = 1$ for density fluctuations]. For sufficiently small cells ($R \ll \xi_L$), $\tilde{\tau}_\sigma(\mathbf{k})$ spreads out so much that result (6.7) is dominated by the incoherent value of $S_w(\mathbf{k})$, and the fluctuations approach the *quantum shot noise* value

$$\Delta W_\sigma^2 \approx N_\sigma S_w(\infty). \tag{6.19}$$

6.7   Quantum Fluctuations: Large Cells

Interactions can affect the long wavelength modes which strongly contribute to the fluctuations measured in large cells.

Two cases arise dependent upon the $k \to 0$ behaviour of the structure factor. Depending on the phase and spin density (and ignoring the special cases of the gapped S_x and divergent S_y structure factors in the BA phase, which we treat later), the $T = 0$ structure factors can either (i) approach zero linearly with k [e.g. see Fig. 6.3(a)] or (ii) approach a finite value at $k = 0$ quadratically with k, with a characteristic correlation peak or trough [e.g. see Fig. 6.3(b)].
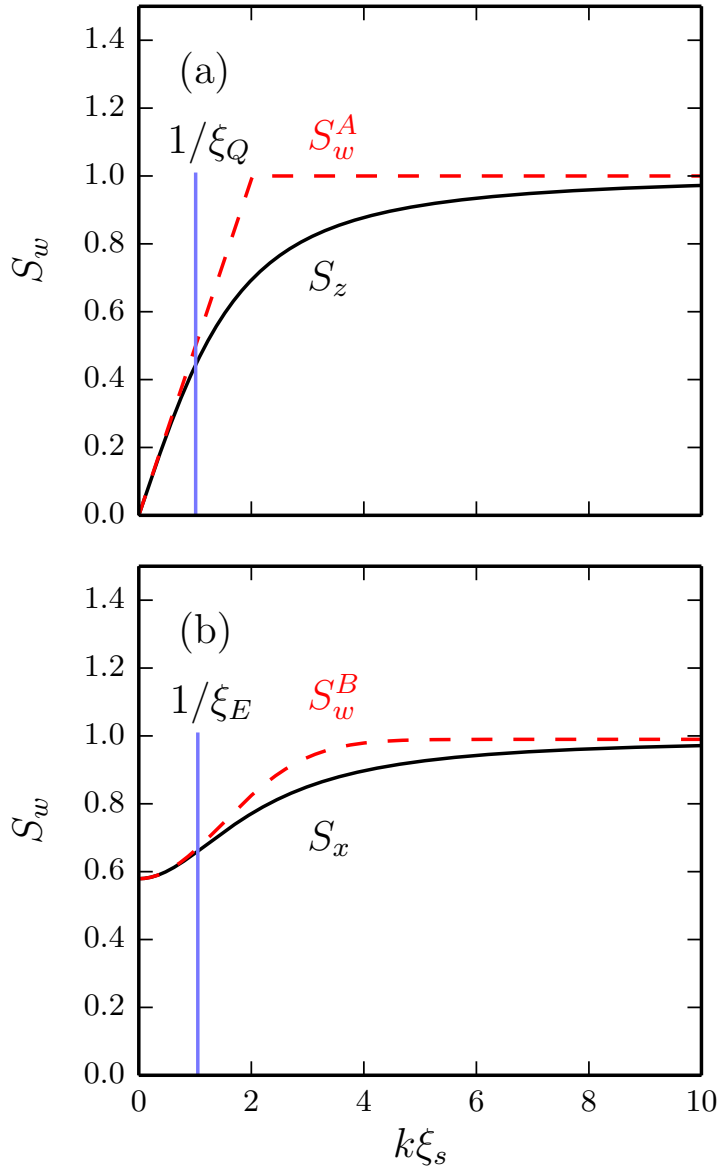
Figure 6.3: Examples of the two models for $T = 0$ structure factors used to derive analytic results. Subplots are: (a) model S_w^A (dashed red line) for where $S_w \propto k$ as $k \to 0$ with characteristic length scale ξ_Q [with S_z (solid black line) as a specific example], and (b) model S_w^B (dashed red line) for where $S_w \propto k^2$ as $k \to 0$ with characteristic length scale ξ_E [with S_x (solid black line) as a specific example]. Examples are from the AF phase with $c_0/c_1 = 50/3$, $f_z/n = 0.2$ and $q/c_1 n = -1$.

6.7.1 Suppressed Structure Factor

For cases where the structure factor vanishes as $k \to 0$ like

$$S_w = \tfrac{1}{2}\xi_Q k, \tag{6.20}$$

(e.g. as happens for S_n at $T = 0$), we find the quasi-2D specific results [78]

$$\frac{\Delta W_\sigma^2}{N_\sigma} \approx \begin{cases} \dfrac{\xi_Q}{\pi R} \ln\left(\dfrac{S_w(\infty)CR}{\xi_Q}\right), & \text{Cylindrical cell} \qquad (6.21\text{a}) \\[2ex] \dfrac{\xi_Q}{2R}\sqrt{\dfrac{\pi}{2}}, & \text{Gaussian cell} \qquad (6.21\text{b}) \end{cases}$$

where ξ_Q parameterises the long wavelength behavior and C is determined by the short wavelength properties of the system[1]. The result for the gaussian cell is valid in the limit that $R \gg \xi_Q$, and follows from applying the result in Sec. B.2 of Appendix B to Eq. (6.20). The result for the cylindrical cell requires accounting for high k behaviour [due to the momentum tail of the geometry function; see Fig. 6.2 (e)], and can be derived by using a model structure factor [see Fig. 6.3 (a)]

$$S_w^A(k) = \begin{cases} \tfrac{1}{2}\xi_Q k, & k < 2/\xi_Q, \\[1ex] S_w(\infty), & k > 2/\xi_Q. \end{cases} \tag{6.22}$$

Integrating Eq. (6.7) using this model yields (6.21a) with

$$C = 16e^{\gamma-1} \approx 10.5, \tag{6.23}$$

where $\gamma \approx 0.5572$ is the Euler constant (also see 3D result for density fluctuations obtained in Sec. IV of Ref. [77]).

Interestingly the prefactor of the logarithm scales as the perimeter of the cell $R \sim \sqrt{N_\sigma}$, showing that long-wavelength quantum fluctuations grow more slowly (non-extensively) with R than thermal fluctuations [which grow extensively as $N_\sigma \sim R^2$, see Eq. (6.16)].

---

[1]For a scalar quasi-2D condensate, ξ_Q is the healing length, and using the Bogoliubov dispersion relation the value $C \approx 7.4$ is obtained (see [78]).

6.7.2   Gapped Structure Factor

For gapped structure factors (where $S_w(0) > 0$) like S_x at $T = 0$ [e.g. Fig. 6.3 (b)], where we can write the structure factor as

$$S_w(k) = S_w(0) + \beta k^2 \xi_s^2 + O(k^4), \tag{6.24}$$

with β containing extra terms of the k^2 coefficient, the fluctuations are given by

$$\frac{\Delta W_\sigma^2}{N_\sigma} \approx S_w(0) + \begin{cases} \dfrac{1}{\sqrt{\pi}} \left[S_w(\infty) - S_w(0) \right] \dfrac{\xi_E}{R}, & \text{Cylindrical cell} \qquad (6.25a) \\[2ex] \dfrac{1}{2} \left[S_w(\infty) - S_w(0) \right] \dfrac{\xi_E^2}{R^2}, & \text{Gaussian cell.} \qquad (6.25b) \end{cases}$$

where

$$\xi_E = \sqrt{\frac{4\beta}{S_w(\infty) - S_w(0)}} \, \xi_s. \tag{6.26}$$

The gaussian result follows from the integrals given in Appendix B.2 using $a = \beta \xi_s^2$. The cylindrical result was derived by making the general observation that in this case the structure factor can be represented as a peak (or dip) at $k = 0$ on top of the background value set by $S_w(\infty)$. Indeed, with reference to Eq. (4.5), the peak is determined by the Fourier transform of the normally ordered part of the correlation function, whereas the Fourier transform of the delta function (completely uncorrelated) part sets the background value. Thus, for a simple analytic model of this case, we use [see Fig. 6.3 (b)]

$$S_w^B(k) \approx [S_w(0) - S_w(\infty)] e^{-(\xi_E k)^2/4} + S_w(\infty), \tag{6.27}$$

where $S_w(0) - S_w(\infty)$ is the peak height, and $2/\xi_E$ is the k-width. To find ξ_E, we perform a series expansion of Eq. (6.27) to get

$$S_w^B(k) \approx S_w(0) - \frac{1}{4}[S_w(0) - S_w(\infty)] k^2 \xi_E^2 + O(k^4), \tag{6.28}$$

and match terms with Eq. (6.24) to solve for ξ_E, giving Eq. (6.26). Substituting our model structure factor Eq. (6.27) into Eq. (6.7) and integrating gives the fluctuation result Eq. (6.25a).

6.8 Cell fluctuation results for spin-1

Like we did for the structure factors and fluctuation amplitudes in Chapter 5, we specialize our results to the cases of measuring total density and the three components of spin density within cells, using the notation

$$\hat{w} \to \{\hat{n}, \hat{f}_x, \hat{f}_y, \hat{f}_z\}, \tag{6.29a}$$

$$\hat{W}_\sigma \to \{\hat{N}_\sigma, \hat{F}_{x,\sigma}, \hat{F}_{y,\sigma}, \hat{F}_{z,\sigma}\}, \tag{6.29b}$$

$$S_w(\mathbf{k}) \to \{S_n(\mathbf{k}), S_x(\mathbf{k}), S_y(\mathbf{k}), S_z(\mathbf{k})\}. \tag{6.29c}$$

We use the structure factor results derived and detailed in Chapter 5, including numerical results and limiting analytic expressions, and apply the cell fluctuation measurement formalism derived in the previous Sections. Our extensive analytic results, obtained with this Chapter's formalism, are summarised in Table 6.1. For the BA phase (with condensate magnetised along f_x) the $\hat{F}_{y,\sigma}$ fluctuations are divergent in the $k \to 0$ limit, while the $\hat{F}_{x,\sigma}$ fluctuations have a gapped zero-temperature structure factor, and we discuss these in Sec. 6.8.5.1. For the P phase, $\hat{F}_{z,\sigma}$ fluctuations are zero to our level of approximation [see Chapter 5.3.2].

To numerically calculate cell fluctuations, we extend our numerics from Chapter 5. For both cylindrical and gaussian cells, we construct the geometry function and integrate this against our computed structure factors. The integration presents challenges numerically, with regards to getting numerical convergence and agreement with analytic limits, particularly for cylindrical cells with the Bessel function in the geometry function – see Fig. 6.2 (c) and (e) compared with (d) and (f). We have to be careful in our choice of k-grid in order to get correct results. For small R, we extend our k-grid to a maximum size scaled by $1/R$ in order to account for the spreading of the geometry function. For large R, we set a minimum size according to the healing length so that the Bessel function can still sample short wavelength behaviour. Gaussian cells are numerically easier to handle because their geometry function decays exponentially and thus in their case we only need k-grids out to a few multiples of $1/R$; in our case we generally use $k_{\max} = 5/R$. Resolution-wise, we use k-grids with between 10^4 and 10^5 points.

In the following subsections, we compare our numeric and analytic results for the fluctuations of the measurement operators given in Eq. (6.29b) in each ground state phase. We discuss the fluctuation scaling with temperature and cell size, and compare cylindrical cells with gaussian cells.

Phase	Obs.(s)	Quantum Large Cells	Thermodynamic Limit	Quantum Small Cells
	$\hat{W}_\sigma$	ξ_Q, ξ_E	χ_w	$S_w(\infty)$
F	$\hat{N}_\sigma, \hat{F}_{z,\sigma}$	$\xi_Q = \hbar/\sqrt{M(c_0+c_1)n}$	$1/(c_0+c_1)n$	1
	$\hat{F}_{x,\sigma}, \hat{F}_{y,\sigma}$	$\xi_E = 0$	$1/E_{g,3}^F$	$1/2$
P	$\hat{N}_\sigma$	$\xi_Q = \xi_n$	$1/c_0 n$	1
	$\hat{F}_{x,\sigma}, \hat{F}_{y,\sigma}$	$\xi_E = \sqrt{\dfrac{c_1 n}{q+2c_1 n}}\sqrt{\dfrac{|c_1|n}{\sqrt{q(q+2c_1 n)}-q}}\,\xi_s$	$2q/[q(q+2c_1 n)-p^2]$	1
	$\hat{F}_{z,\sigma}$	0	0	0
AF	$\hat{N}_\sigma$	$\xi_Q = \left\{1 + \dfrac{f_z^2}{n^2}\left[-\dfrac{1}{2}\dfrac{c_1}{c_0} + \sqrt{1-\dfrac{f_z^2}{n^2}}\left(\dfrac{c_1}{c_0}\right)^{\frac{3}{2}}\right]\right\}\xi_n$	$1/c_0 n$	1
	$\hat{F}_{z,\sigma}$	$\xi_Q = \left[\sqrt{1-\dfrac{f_z^2}{n^2}}\left(1-\dfrac{3f_z^2}{2n^2}\dfrac{c_1}{c_0}\right) + \dfrac{f_z^2}{n^2}\sqrt{\dfrac{c_1}{c_0}}\right]\xi_s$	$1/c_1 n$	1
	$\hat{F}_{x,\sigma}$	$\xi_E = \sqrt{\dfrac{2\alpha_z c_1 n}{(\alpha_z + [1-q/c_1 n - E_{g,2}^{AF}/c_1 n])E_{g,2}^{AF}}}\,\xi_s$	$\dfrac{1+\alpha_z}{1+\alpha_z - \frac{q}{c_1 n}}\dfrac{1}{c_1 n}$	$\frac{1}{2}(1+\alpha_z)$
	$\hat{F}_{y,\sigma}$	$\xi_E = \sqrt{\dfrac{2\alpha_z c_1 n}{(\alpha_z - [1-q/c_1 n - E_{g,2}^{AF}/c_1 n])E_{g,2}^{AF}}}\,\xi_s$	$\dfrac{1-\alpha_z}{1-\alpha_z - \frac{q}{c_1 n}}\dfrac{1}{c_1 n}$	$\frac{1}{2}(1-\alpha_z)$
BA $(p=0)$	$\hat{N}_\sigma$	$\xi_Q = \hbar/\sqrt{M(c_0+c_1)n}$	$1/(c_0+c_1)n$	1
	$\hat{F}_{x,\sigma}$	$\xi_Q[\star] = \dfrac{1}{1-\tilde{q}^2}\dfrac{\hbar}{\sqrt{m(c_0+c_1)n}}$	$\dfrac{1}{1-\tilde{q}^2}\left(\dfrac{1}{(c_0+c_1)n} + \dfrac{2\tilde{q}^2}{|c_1|n}\right)$	1
	$F_{y,\sigma}$	$[\star]$	$[\star]$	$\frac{1}{2}(1+\tilde{q})$
	$\hat{F}_{z,\sigma}$	$\xi_Q = \frac{1}{2}(1-\tilde{q})\xi_s/\sqrt{\tilde{q}}$	$(1-\tilde{q})/q$	$\frac{1}{2}(1-\tilde{q})$

Table 6.1: Analytic results for cell measurement fluctuations in a uniform spin-1 condensate. We detail parameters in all four magnetic phases for the quantum large-cell limit [Eq. (6.21)], thermodynamic limit [Eq. (6.16)] and quantum small-cell limit [Eq. (6.19)] for the observables in Eq. (6.29b). Values for $S_w(0)$ [needed for Eq. (6.25)] are provided in Table 4.2. The quantities $\tilde{q}$, α_z, $E_{g,2}^{AF}$, and $E_{g,3}^F$ are defined in Eqs. (2.25), (2.26), Eq. (5.24), and Eq. (5.5), respectively.

$\star$ – the zero-temperature $\hat{F}_{x,\sigma}$ structure factor is gapped, and the $\hat{F}_{y,\sigma}$ structure factor is divergent at $k \to 0$; we cover these specific cases later in Sec. 6.8.5.

6.8.1 Parameters for numerical results

We calculate fluctuations numerically for the quasi-2D uniform system that approximates the central region of a cloud of $N = 10^6$ atoms in a harmonic pancake trap with frequencies $\omega_{z,\rho} = 2\pi \times (300, 5)$ Hz (see Appendix A for details).

We choose interaction parameters within the range of experimental values, with reference to Table 2.1. For the F, P and AF phases, we use parameters appropriate to antiferromagnetic ^{23}Na, and for the BA phase we consider parameters appropriate for ferromagnetic ^{87}Rb, as listed in Table 6.2.

Parameter	^{23}Na	^{87}Rb
$c_0 n/k_B$	14.3 nK	28.1 nK
$\lvert c_1 \rvert n/k_B$	0.280 nK	0.111 nK
ξ_n	1.21 μm	0.446 μm
ξ_s	8.68 μm	7.08 μm

Table 6.2: Species-specific parameters for numerically calculating fluctuations within cells. Note that the interaction parameters are the appropriate quasi-2D effective interaction parameters for the system, and that for ^{87}Rb we have $c_1 < 0$.

6.8.2 F phase

Numerical results for the F phase are presented, along with analytic limits, in Fig. 6.4 as a function of temperature and in Fig. 6.5 as a function of cell size R. As discussed in Chapter 5, to our level of approximation we have that $\hat{N}_\sigma = \hat{F}_{z,\sigma}$ in the F phase. Since only the density phonon mode ($\nu = 0$) contributes to these fluctuations, the $\hat{N}_\sigma$ and $\hat{F}_{z,\sigma}$ operators can essentially be described using similar arguments to those applied to describe the the number fluctuations of a scalar system, with healing length

$$\xi_Q = \hbar/\sqrt{M(c_0 + c_1)n} = 1.20\,\mu\text{m}, \tag{6.30}$$

slightly smaller than the density healing length ξ_n. The behaviour of this type of system has been studied thoroughly [45, 78], and can be understood by considering the competing length scales. The relevant length scales are the cell size R, the thermal wavelength defined in relation to the $\nu = 0$ spectrum

$$E_0^F\left(\frac{1}{\lambda_{th}}\right) \equiv k_B T, \tag{6.31}$$

and the correlation length ξ_Q which depends on the structure factor of the operator under consideration. We note that for $k_B T < (c_0 + c_1)n$, λ_{th} is the *thermal phonon wavelength*,

$$\lambda_{th} \sim \frac{\hbar^2}{M\xi_Q k_B T}, \tag{6.32}$$

while for $k_B T > (c_0 + c_1)n$ it is proportional to the usual thermal de-Broglie wavelength

$$\lambda_{th} \sim \frac{\hbar}{\sqrt{2Mk_B T}}. \tag{6.33}$$

For $R \ll \{\lambda_{th}, \xi_Q\}$, we go to the quantum small-cell limit as we see in Fig. 6.5(a) and (c). In this regime, atoms within the cell are independent, and we sample the incoherent value of the structure factor independently of temperature so long as $\lambda_{th} \gg R$.

As T increases to the point where λ_{th} is comparable to or smaller than R, the relevant modes become thermally occupied and fluctuations increase. We see this in Fig. 6.4 (a) and (c), noting that it happens at lower T for larger cells. In the high T regime, $\lambda_{th} \ll R$ and the fluctuations increase linearly with T, as predicted by the classical thermodynamic result in Eq. (6.16). However, if R is not much larger than ξ_Q then correlations are still important, which leads to an offset from the limit. This reduction was seen and discussed in Fig. 3 of Ref. [78]. With reference to the $T = 5$ nK and $T = 50$ nK lines on Fig. 6.5 (a) and (c), we see that for any temperature we can get to

a regime where R is larger than all other length scales and fluctuations are dominated by thermal modes, thus reaching the thermodynamic limit.

In the case of zero-temperature, for $R \gtrsim \xi_Q$ we sample the quantum phonon regime [see Fig. 2(b) in Ref. [45]] as $R \to \infty$ (since $\lambda_{th} = \infty$) and we get fluctuations which monotonically decrease to zero (relative to N_σ) with increasing R.

Due to the axial symmetry of the F phase, we have that $\hat{F}_{x,\sigma} = \hat{F}_{y,\sigma}$. For these fluctuations, the correlation length ξ_E is zero. This leads to fluctuations which scale extensively at low temperatures (i.e. there is no R dependence). For high temperatures, modes become thermally occupied and fluctuations increase linearly with T [see Fig. 6.4 (b) and (d), similar to the high temperature regime in Fig. 6.4(a) and (c)].

Comparing cylindrical and gaussian cell subplots in Figs. 6.4 and 6.5, we see that they have qualitatively the same fluctuation behaviour. To understand the small differences, we note that the oscillating tail of the cylindrical geometry function [see Fig. 6.2 (c) and (e)] means cylindrical cells are sensitive to fluctuations at higher momenta than just the main peak (whose position depends on $1/R$ for both cell shapes), unlike gaussian cells with their exponentially decaying momentum dependence. Thus, gaussian fluctuations have less fluctuations at low-temperature with large cells, because only modes with wavelength $\sim R$ contribute and the higher value of the incoherent limit is exponentially suppressed. The decay rate of the cylindrical geometry function [see Fig. 6.2] means that cylindrical cells converge slower to our high R fluctuation limits, which we see in both Fig. 6.4 and Fig. 6.5. Gaussian cells converge slower to the small cell limit, since their geometry function spreads out slower in momentum space than that of cylindrical cells. Another difference is that, as shown in Fig. 6.5 (a), the cylindrical zero-temperature high-R limit [Eq. (6.21a)] is valid for a wider range of R values than the analogous gaussian limit [Eq. (6.21b)] in Fig. 6.5 (c), although it becomes an invalid approximation for $R/\xi_Q \lesssim 1$.
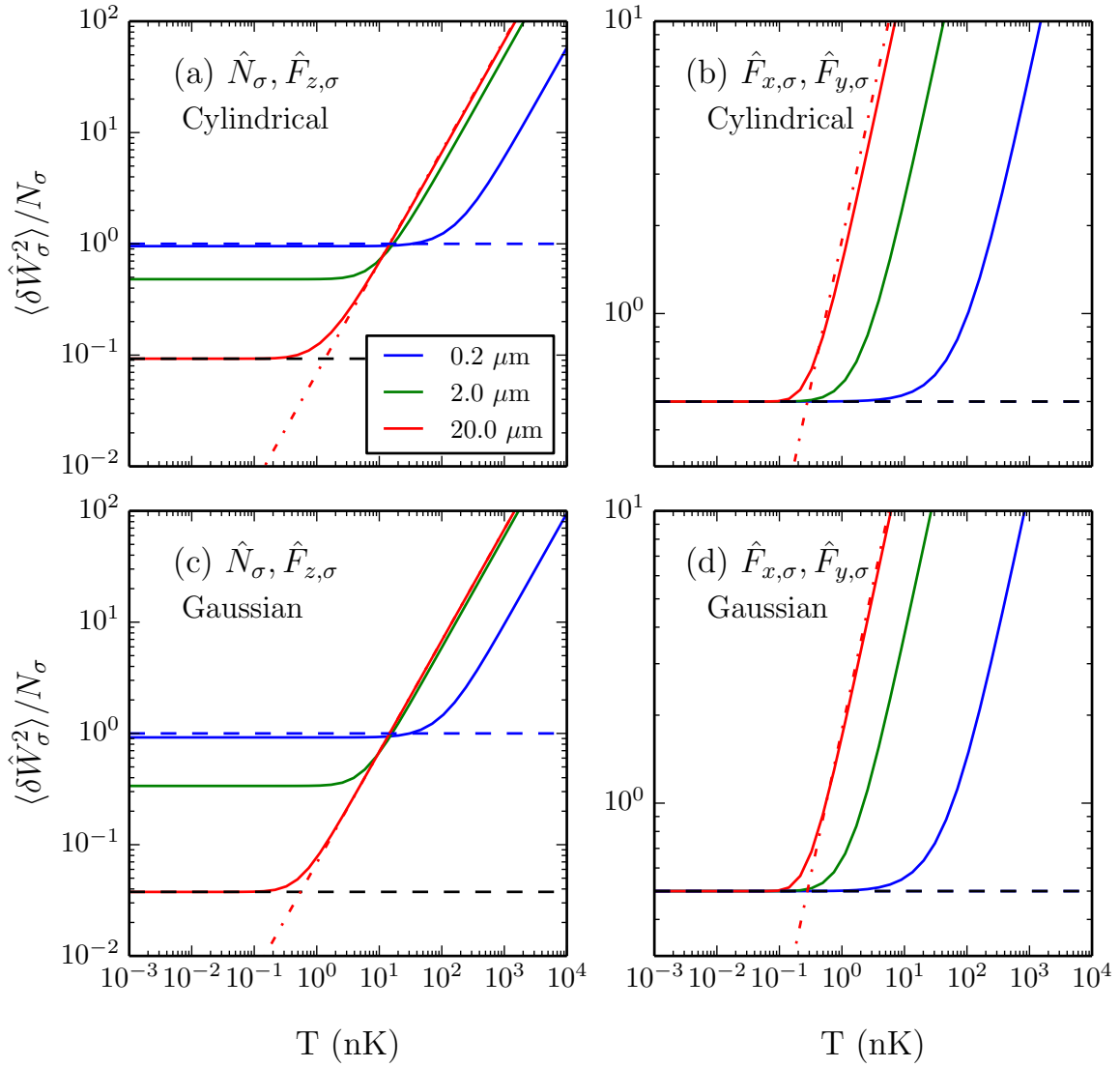
Figure 6.4: Cell fluctuations for the F phase as a function of temperature T. Subplots show observables (a) $\hat{N}_\sigma$, $\hat{F}_{z,\sigma}$ and (b) $\hat{F}_{x,\sigma}$, $\hat{F}_{y,\sigma}$ for cylindrical cells, and (c) $\hat{N}_\sigma$, $\hat{F}_{z,\sigma}$ and (d) $\hat{F}_{x,\sigma}$, $\hat{F}_{y,\sigma}$ for gaussian cells. We plot cell sizes of $R \in \{0.2, 2, 20\} \times \mu$m, as labelled in (a). Also plotted are the quantum small cell limit (dashed blue line), quantum large cell limit (dashed black line) and thermodynamic limit (dot-dashed red line). Parameters are as in Sec. 6.8.1, with $f_z = n$, $p = c_1 n$ and $q = -c_1 n$.
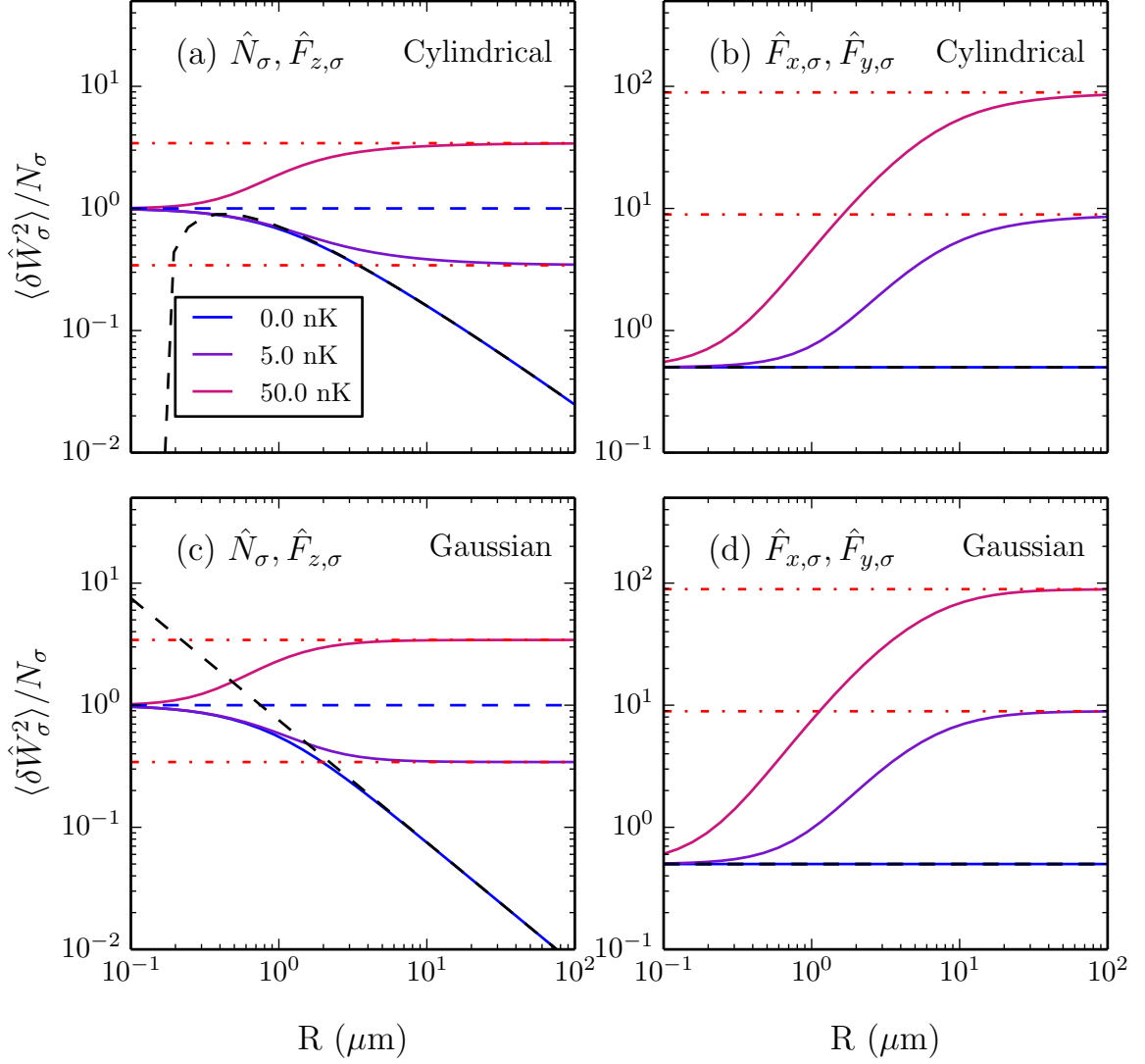
Figure 6.5: Cell fluctuations for the F phase as a function of cell size R. Subplots show observables (a) $\hat{N}_\sigma, \hat{F}_{z,\sigma}$ and (b) $\hat{F}_{x,\sigma}, \hat{F}_{y,\sigma}$ for cylindrical cells, and (c) $\hat{N}_\sigma, \hat{F}_{z,\sigma}$ and (d) $\hat{F}_{x,\sigma}, \hat{F}_{y,\sigma}$ for gaussian cells. For temperatures $T \in \{0, 5, 50\}$ nK, as labelled in (a). Also plotted are the quantum small cell limit (dashed blue line), quantum large cell limit (dashed black line) and thermodynamic limit (dot-dashed red line). Parameters are as in Sec. 6.8.1, with $f_z = n$, $p = c_1 n$ and $q = -c_1 n$.

6.8.3   P phase

Numerical results for the P phase are presented, along with analytic limits, in Fig. 6.6 as a function of temperature and in Fig. 6.7 as a function of cell size R. As discussed in Chapter 5, to our level of approximation we have that $\hat{F}_{z,\sigma} = 0$ in the P phase. Our analysis in Chapter 5 also showed that only the $\nu = 0$ phonon mode contributes to $\hat{N}_\sigma$ fluctuations, and thus they are essentially described by an equivalent scalar system but with healing length given by

$$\xi_Q = \xi_n = 1.21\,\mu\text{m}. \tag{6.34}$$

The same analysis done in the F phase for $\hat{N}_\sigma$ and $\hat{F}_{z,\sigma}$ now applies for the results shown in Fig. 6.6 (a) and (c) and Fig. 6.7 (b) and (d).

The axial symmetry of the P phase means that, as in the F phase, we have $\hat{F}_{x,\sigma} = \hat{F}_{y,\sigma}$. The same analysis as for the F phase applies, except that now we have a non-zero correlation length given by

$$\xi_E = 6.63\,\mu\text{m}, \tag{6.35}$$

which causes non-extensive scaling with R at low temperatures in Fig. 6.6(b) and (d). Zero temperature fluctuations have a non-zero lower limit set by the gap ($k = 0$ value) of the structure factor [see Fig. 5.8 (b)], as seen by the solid blue lines in Fig. 6.7 (b) and (d) having a non-zero high-R limit (a similar non-zero value was seen in Ref. [48] for a gapped structure factor in a two-component system). This is different from the analogous case in the F phase in Fig. 6.5 (b) and (d) where the zero temperature fluctuations tended to zero at high R. At high temperatures we get the same behaviour as in the F phase.
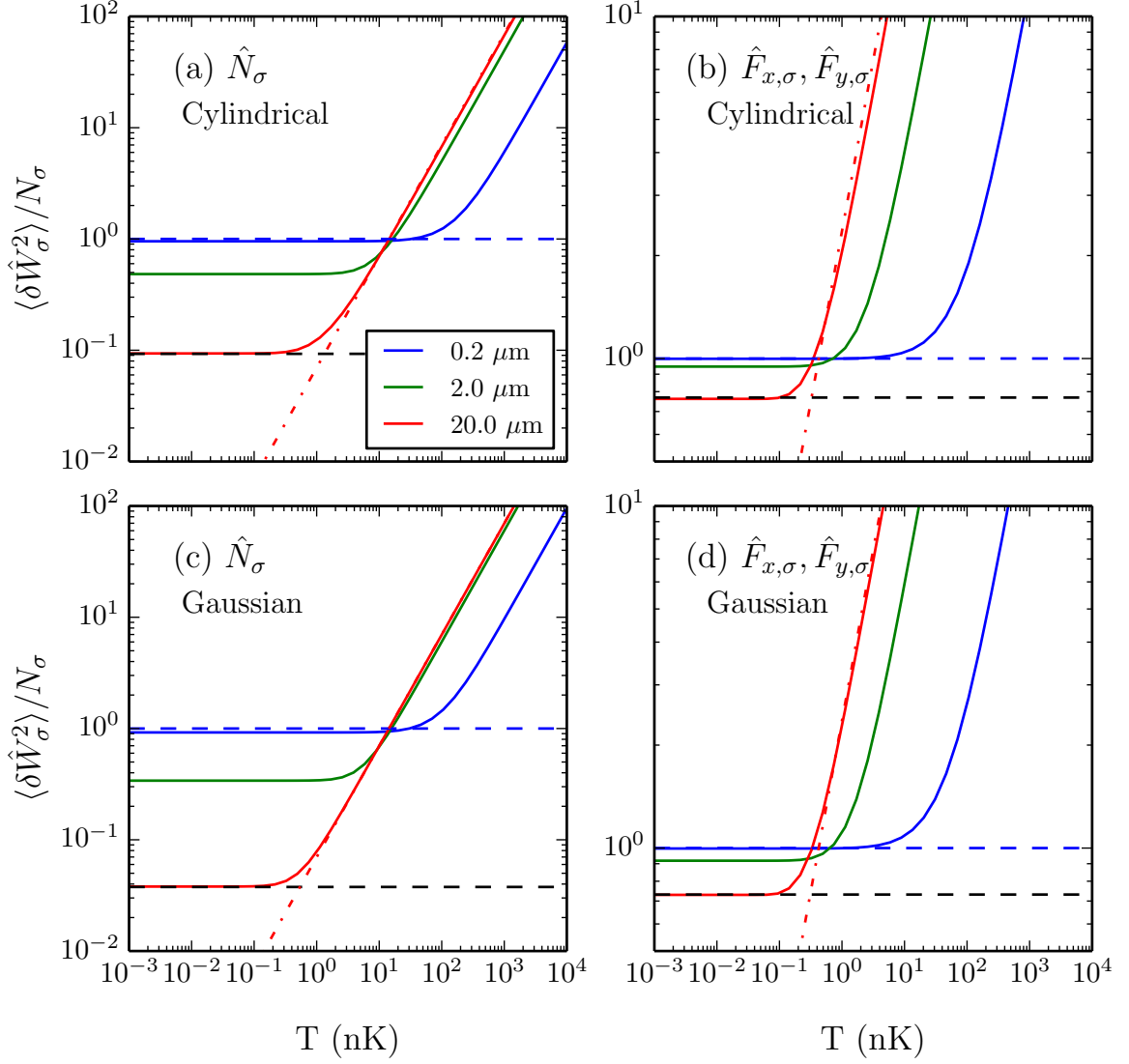
Figure 6.6: Cell fluctuations for the P phase as a function of temperature. Subplots show observables (a) $\hat{N}_\sigma$ and (b) $\hat{F}_{x,\sigma}, \hat{F}_{y,\sigma}$ for cylindrical cells, and (c) $\hat{N}_\sigma$ and (d) $\hat{F}_{x,\sigma}, \hat{F}_{y,\sigma}$ for gaussian cells. For cell sizes $R \in \{0.2, 2, 20\}\mu$m, as labelled in (a). Also plotted are the quantum small cell limit (dashed blue line), quantum large cell limit (dashed black line) and thermodynamic limit (dot-dashed red line). Parameters are as in Sec. 6.8.1, with $f_z = 0$, $p = 1.5c_1n$ and $q = 2.1c_1n$.
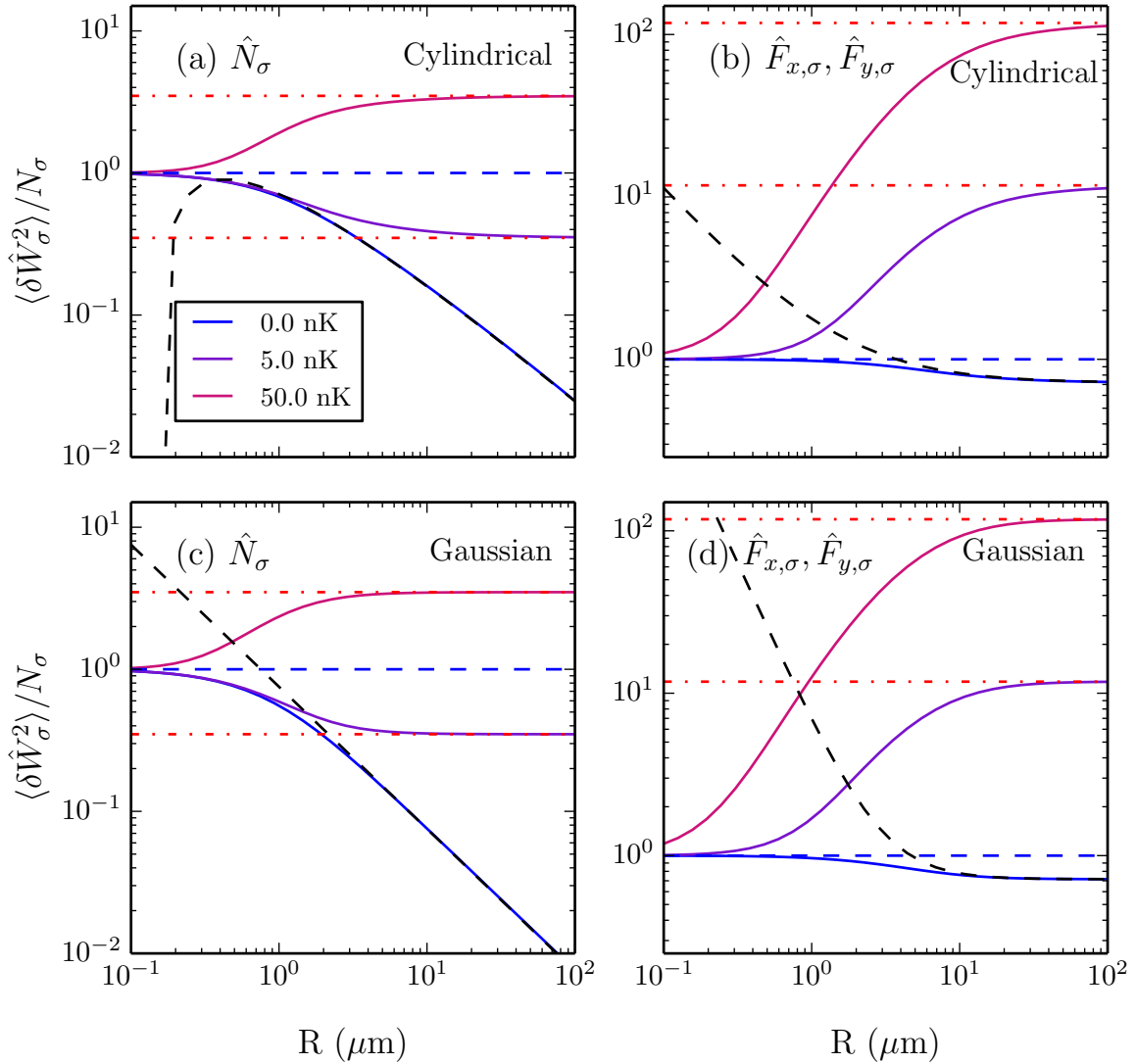
Figure 6.7: Cell fluctuations for the P phase as a function of cell size R. Subplots show observables (a) $\hat{N}_\sigma$ and (b) $\hat{F}_{x,\sigma}, \hat{F}_{y,\sigma}$ for cylindrical cells, and (c) $\hat{N}_\sigma$ and (d) $\hat{F}_{x,\sigma}, \hat{F}_{y,\sigma}$ for gaussian cells. For temperatures $T \in \{0, 5, 50\}$ nK, as labelled in (a). Also plotted are the quantum small cell limit (dashed blue line), quantum large cell limit (dashed black line) and thermodynamic limit (dot-dashed red line). Parameters are as in Sec. 6.8.1, with $f_z = 0$, $p = 1.5c_1n$ and $q = 2.1c_1n$.

6.8.4 AF phase

Numerical results for the AF phase are presented, along with analytic limits, in Fig. 6.8 (cylindrical cells) and Fig. 6.9 (gaussian cells) as a function of temperature, and in Fig. 6.10 (cylindrical cells) and Fig. 6.11 (gaussian cells) as a function of cell size R. The $\hat{N}_\sigma$ and $\hat{F}_{z,\sigma}$ fluctuations can essentially be described by the number fluctuations of equivalent scalar systems. For $\hat{N}_\sigma$, the healing length is

$$\xi_Q = 1.21\,\mu\text{m}. \tag{6.36}$$

For $\hat{F}_{z,\sigma}$, the appropriate healing length is

$$\xi_Q = 8.55\,\mu\text{m}, \tag{6.37}$$

which is only slightly smaller than the spin healing length ξ_s. The results in subplots (a) and (b) in Figs. 6.8, 6.9, 6.10 and 6.11 can then be interpreted in the same way as the results for $\hat{N}_\sigma$ and $\hat{F}_{z,\sigma}$ in the F phase.

For $\hat{F}_{x,\sigma}$, the correlation length is

$$\xi_E = 8.27\,\mu\text{m}, \tag{6.38}$$

while for $\hat{F}_{y,\sigma}$ it is

$$\xi_E = 10.8\,\mu\text{m}. \tag{6.39}$$

The results in subplots (c) and (d) in Figs. 6.8, 6.9, 6.10 and 6.11 can be interpreted in the same way as the results for $\hat{F}_{x,\sigma}$ and $\hat{F}_{y,\sigma}$ in the P phase. There is one difference: for $\hat{F}_{y,\sigma}$, the $k = 0$ gap in the structure factor is higher than the $k \to \infty$ incoherent limit [see Fig. 5.12 (d)]. This has the effect that at low temperatures, fluctuations scale non-extensively in the opposite manner to $\hat{F}_{x,\sigma}$ fluctuations – as cell size increases the fluctuations increase faster than the volume does. We can also see this in subplot (d) of Figs. 6.10 and 6.11, where the fluctuations are lowest for the quantum small cell limit. It is worth noting that axial symmetry is broken in the AF phase, and this leads to heavy suppression of $\hat{F}_{y,\sigma}$ fluctuations in our results [where for our parameters we have $\alpha = 0.98$; $\alpha = 1$ is fully asymmetric, see Eq. (5.23)].
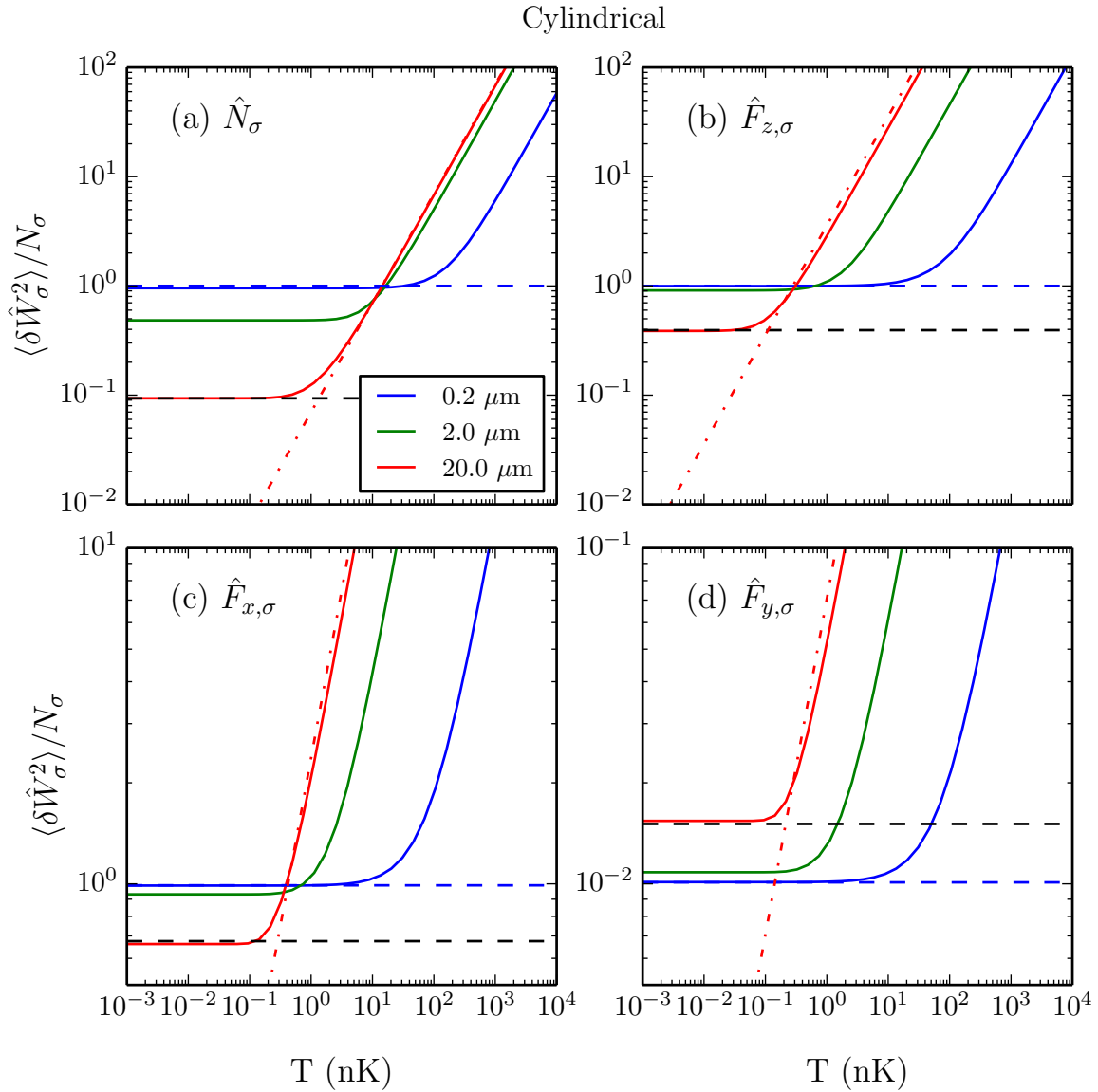
Figure 6.8: Cylindrical cell fluctuations for the AF phase as a function of temperature. Subplots show observables (a) $\hat{N}_\sigma$, (b) $\hat{F}_{z,\sigma}$, (c) $\hat{F}_{x,\sigma}$ and (d) $\hat{F}_{y,\sigma}$. For cell sizes $R \in \{0.2, 2, 20\}\mu$m, as labelled in (a). Also plotted are the quantum small cell limit (dashed blue line), quantum large cell limit (dashed black line) and thermodynamic limit (dot-dashed red line). Parameters are as in Sec. 6.8.1, with $f_z = 0.2n$ and $q = -c_1 n$.
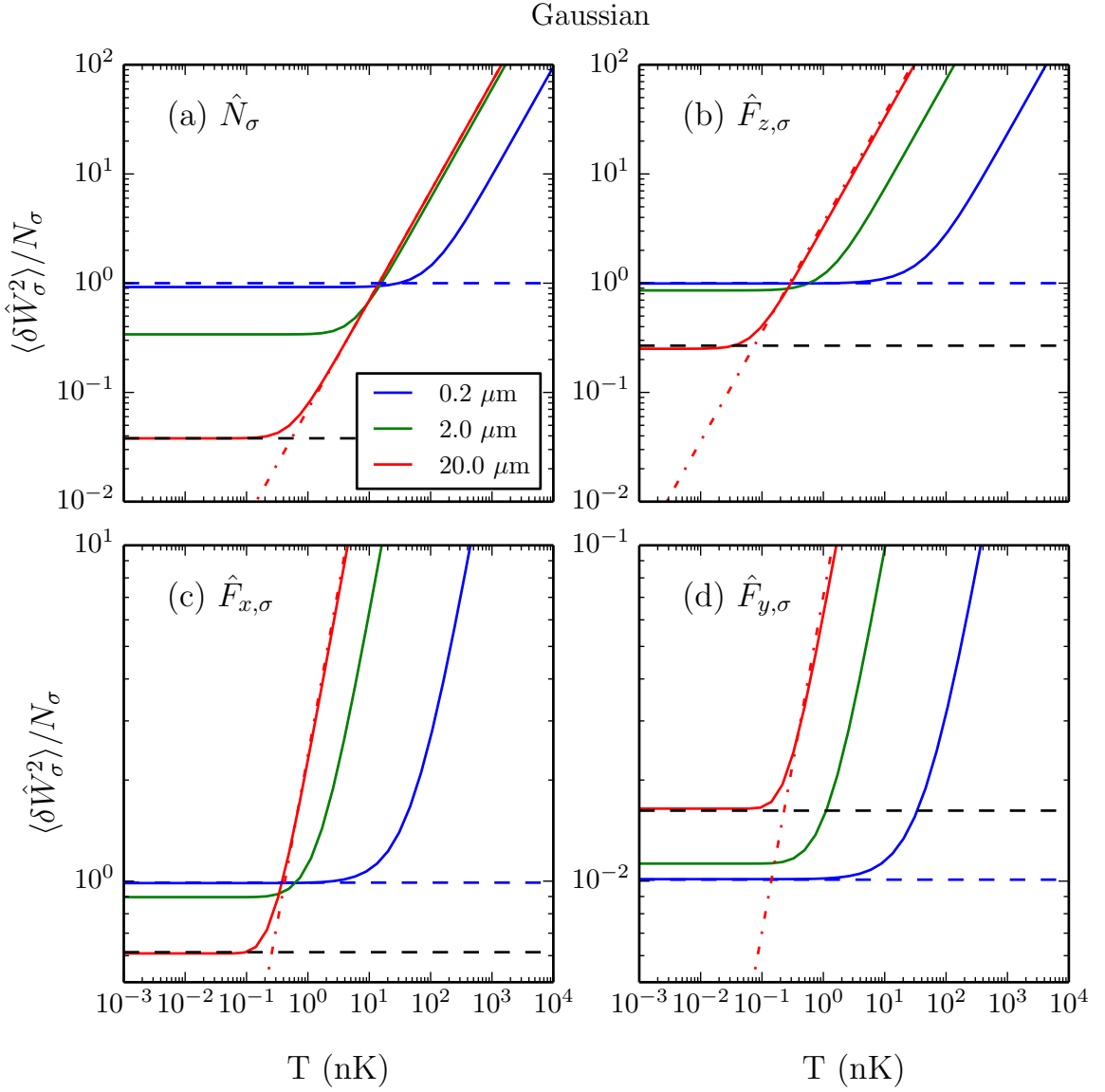
Figure 6.9: Cell fluctuations for the AF phase as a function of temperature, as in Fig. 6.8, but for gaussian cells.
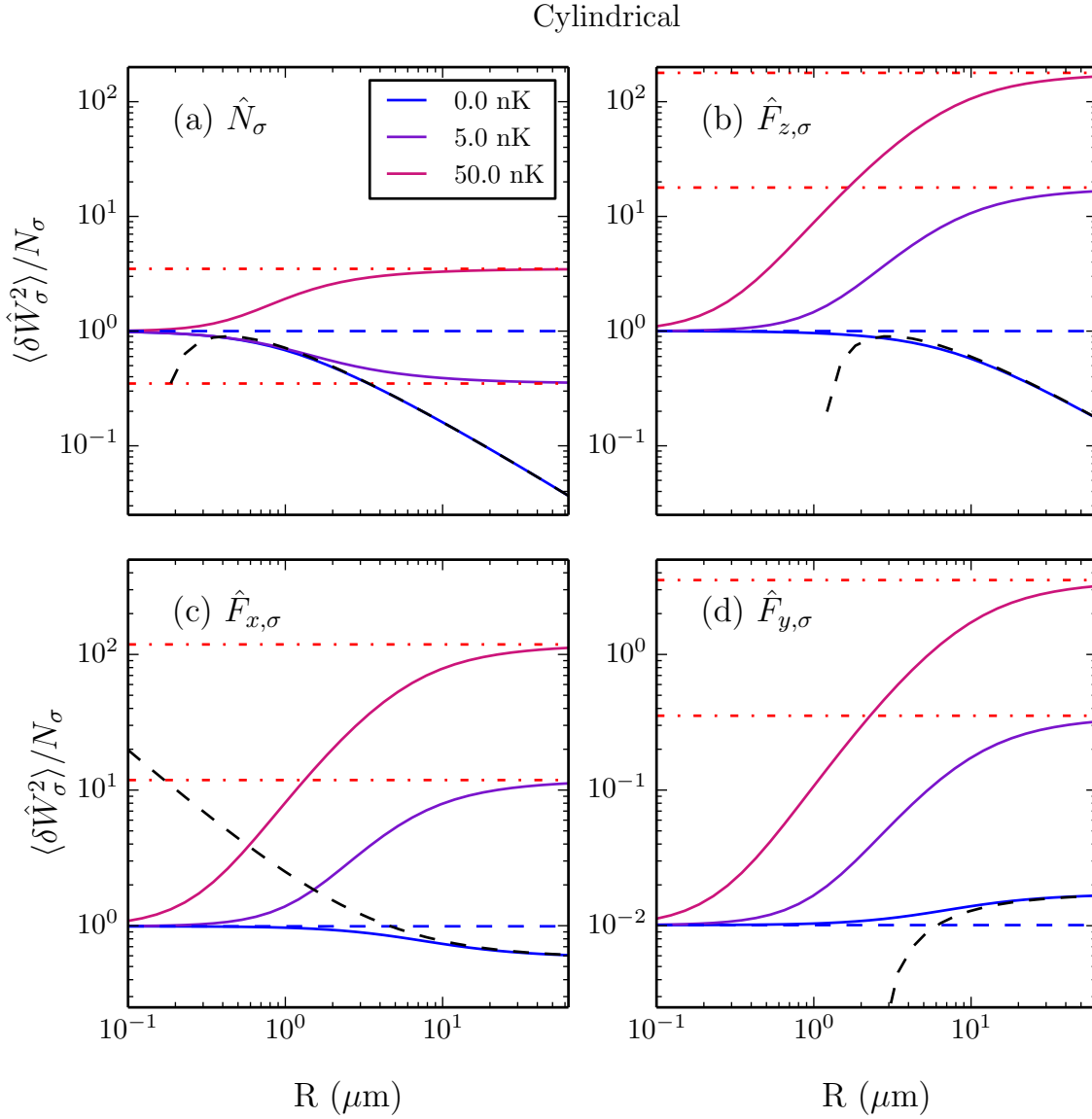
Figure 6.10: Cylindrical cell fluctuations for the AF phase as a function of cell size R. Subplots show observables (a) $\hat{N}_\sigma$, (b) $\hat{F}_{z,\sigma}$, (c) $\hat{F}_{x,\sigma}$ and (d) $\hat{F}_{y,\sigma}$. For temperatures $T \in \{0, 5, 50\}$ nK, as labelled in (a). Also plotted are the quantum small cell limit (dashed blue line), quantum large cell limit (dashed black line) and thermodynamic limit (dot-dashed red line). Parameters are as in Fig. 6.8.
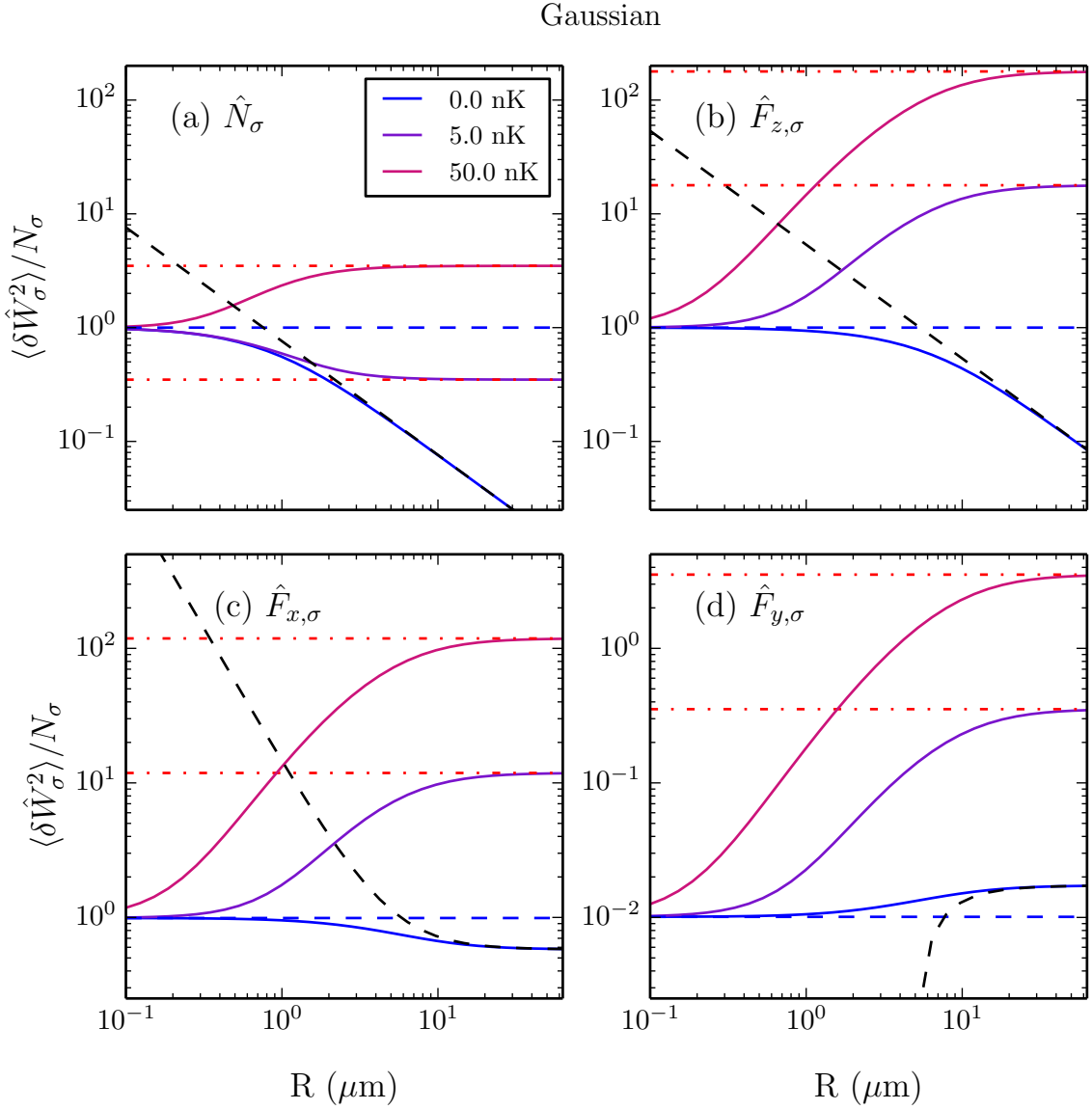
Figure 6.11: Cell fluctuations for the AF phase as a function of cell size R, as in Fig. 6.10, but for gaussian cells.

6.8.5   BA phase

Numerical results for $\hat{N}_\sigma$, $\hat{F}_{z,\sigma}$ and $\hat{F}_{x,\sigma}$ fluctuations in the BA phase are presented, along with analytic limits, in Fig. 6.12 (cylindrical cells) and Fig. 6.13 (gaussian cells) as a function of temperature, and in Fig. 6.14 (cylindrical cells) and Fig. 6.15 (gaussian cells) as a function of cell size R. Note that for this phase, we use parameters from Table 2.1 appropriate to ferromagnetic ^{87}Rb, which has a much smaller density healing length than ^{23}Na which we looked at in previous phases.

The $\hat{N}_\sigma$ and $\hat{F}_{z,\sigma}$ fluctuations can essentially be described by the number fluctuations of equivalent scalar systems. For $\hat{N}_\sigma$, the healing length is

$$\xi_Q = \xi_n = 0.446\,\mu\text{m}. \tag{6.40}$$

For $\hat{F}_{z,\sigma}$, the relevant healing length is

$$\xi_Q = 10.0\,\mu\text{m}, \tag{6.41}$$

which is larger than the spin healing length $\xi_s = 7.08\,\mu\text{m}$.

For $\hat{F}_{x,\sigma}$, the $\hat{f}_x$ structure factor is gapped [i.e. non-zero at $k = 0$, see Fig. 5.16 (c)], but otherwise has a linear dependence on k as $k \to 0$, with a healing length

$$\xi_Q = 0.36\,\mu\text{m}, \tag{6.42}$$

slightly larger than the density healing length. To calculate the quantum large-cell fluctuations (which are affected by the gap), we adapt our model of Sec. 6.7.1, writing the structure factor as

$$S_x(k) = S_x(0) + S_x^A(k), \tag{6.43}$$

where

$$S_x^A(k) = \begin{cases} \frac{1}{2}\xi_Q k, & k < 2/\xi_Q, \\ d \equiv S_x(\infty) - S_x(0), & k > 2/\xi_Q, \end{cases} \tag{6.44}$$

i.e. we separate out the constant part and write the remaining part as a model structure factor. We get results slightly modified from the quantum large-cell results in Eqs. (6.21a) and (6.21b),

$$\frac{\Delta \hat{F}_{x,\sigma}^2}{N_\sigma} \approx S_x(0) + \begin{cases} \dfrac{\xi_Q}{\pi R} \ln\left(\dfrac{CdR}{\xi_Q}\right), & \text{Cylindrical cells} \quad\;\;\; \text{(6.45a)} \\[2ex] \dfrac{\xi_Q}{2R}\sqrt{\dfrac{\pi}{2}}, & \text{Gaussian cells} \quad\quad\;\; \text{(6.45b)} \end{cases}$$

where C is the same constant described in the Sec. 6.7.1 that depends on the small-wavelength behaviour of the structure factor.

The same analysis we performed on the F phase now applies to the results for $\hat{N}_\sigma$, $\hat{F}_{z,\sigma}$ and $\hat{F}_{x,\sigma}$. The only significant difference, apart from the length scales, is that $\hat{F}_{x,\sigma}$ has a minimum level of fluctuations set by the structure factor gap, which we can see in the low temperature behaviour with R in subplot (c) of Figs 6.12 and 6.14. We saw similar behaviour in the P phase with the $\hat{F}_{x,\sigma}$ and $\hat{F}_{y,\sigma}$ fluctuations [see subplots (b) and (d) in both Figs. 6.6 and 6.7], although their structure factors had a quadratic dependence on k rather than a linear one.
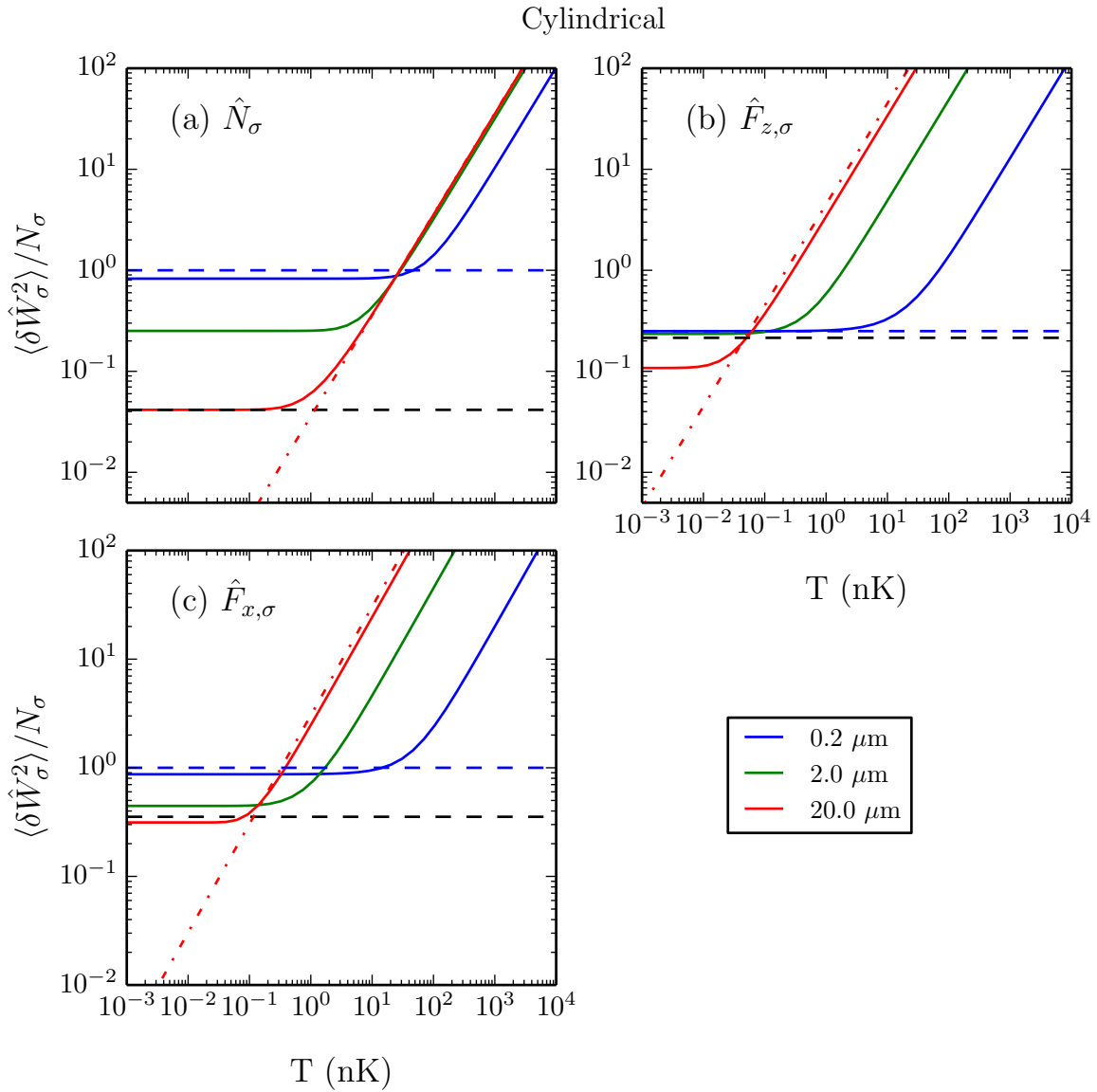
Figure 6.12: Cylindrical cell fluctuations for the BA phase as a function of temperature. Subplots show observables (a) $\hat{N}_\sigma$, (b) $\hat{F}_{z,\sigma}$, and (c) $\hat{F}_{x,\sigma}$. For cell sizes $R \in \{0.2, 2, 20\}\mu$m, as labelled in legend (outset). Also plotted are the quantum small cell limit (dashed blue line), quantum large cell limit (dashed black line) and thermodynamic limit (dot-dashed red line). Parameters are as in Sec. 6.8.1, with $f_z = 0$, $p = 0$ and $q = |c_1|n$.
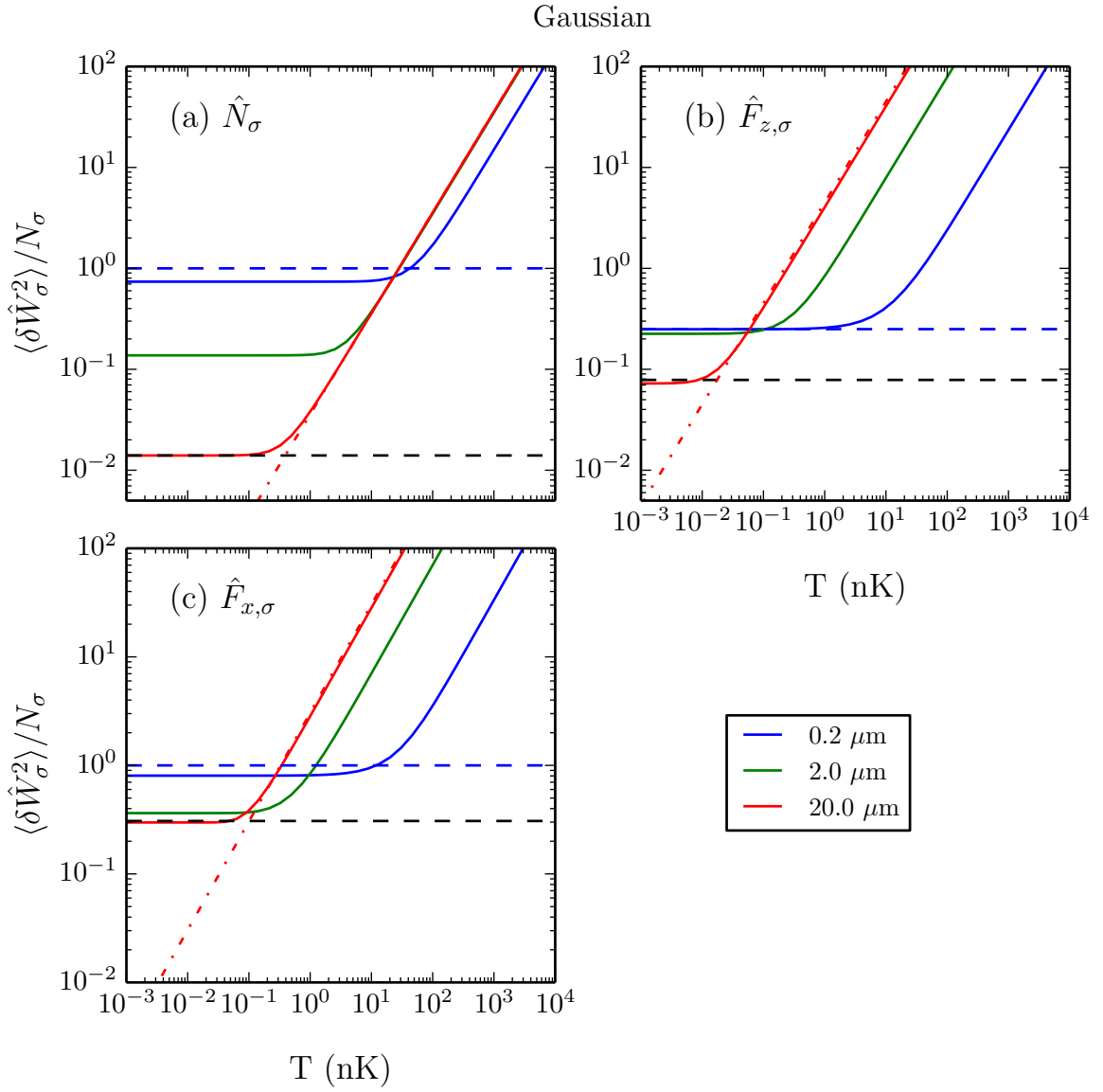
Figure 6.13: Cell fluctuations for the BA phase as a function of temperature, as in Fig. (6.12), but for gaussian cells.
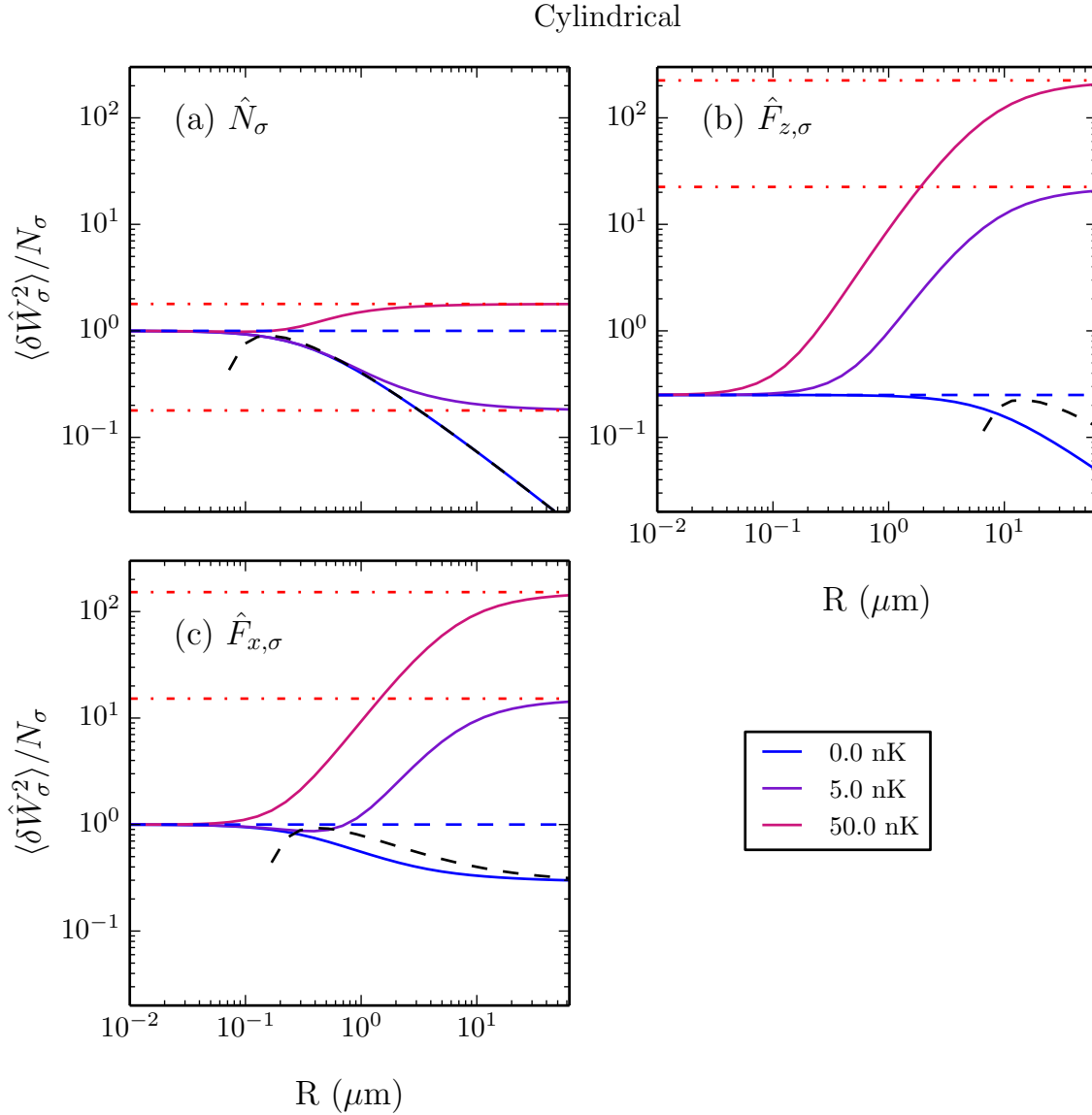
Figure 6.14: Cylindrical cell fluctuations for the BA phase as a function of cell size R. Subplots show observables (a) $\hat{N}_\sigma$, (b) $\hat{F}_{z,\sigma}$, and (c) $\hat{F}_{x,\sigma}$. For temperatures $T \in \{0, 5, 50\}$ nK, as labelled in legend (outset). Also plotted are the quantum small cell limit (dashed blue line), quantum large cell limit (dashed black line) and thermodynamic limit (dot-dashed red line). Parameters are as in Fig. (6.12).

Figure 6.15: Cell fluctuations for the BA phase as a function of cell size R, as in Fig. (6.14), but for gaussian cells.

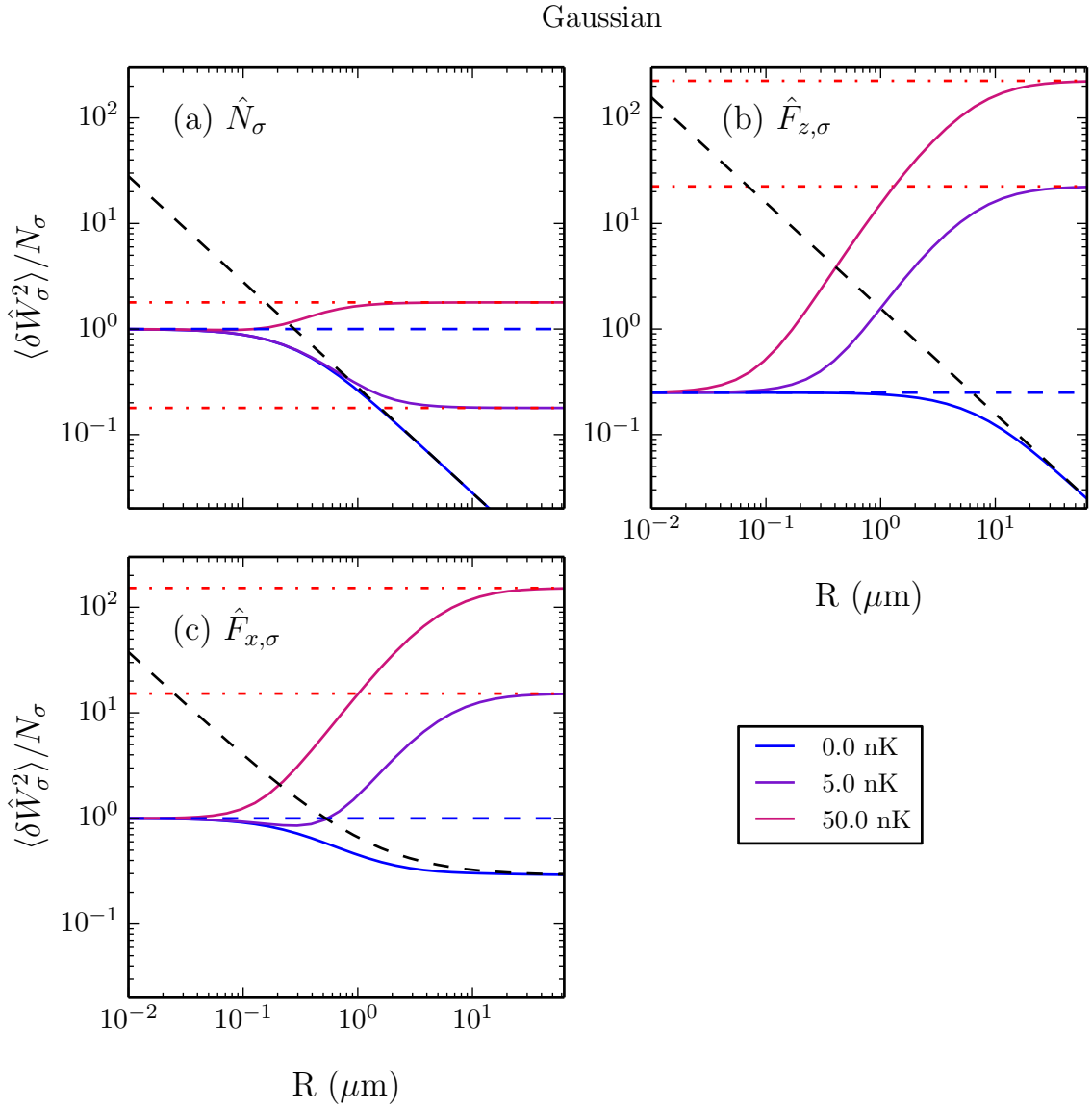### 6.8.5.1 Divergent $\hat{f}_y$ structure factor

In the BA phase [see Fig. 5.16 (d)], the $\hat{f}_y$ structure factor diverges as

$$
S_y(k \to 0) = \begin{cases} \left(\dfrac{(1+\tilde{q})\sqrt{\tilde{q}}}{\xi_s} \right) k^{-1}, & T = 0, & \text{(6.46a)} \\[4mm] \left(\dfrac{2(1+\tilde{q})}{\xi_s^2} \dfrac{k_B T}{|c_1|n} \right) k^{-2}, & T > 0. & \text{(6.46b)} \end{cases}
$$

Let us define

$$
\tilde{\xi}_Q = \frac{2}{(1+\tilde{q})} \frac{\xi_s}{\sqrt{\tilde{q}}}, \tag{6.47}
$$

$$
\tilde{\xi}_E^2 = \frac{2}{(1+\tilde{q})} \xi_s^2, \tag{6.48}
$$

such that we can write the structure factor as

$$
S_y(k \to 0) = \begin{cases} \left(\dfrac{1}{2} k \tilde{\xi}_Q \right)^{-1}, & T = 0, & \text{(6.49a)} \\[4mm] \left(\dfrac{1}{2} k \tilde{\xi}_E \right)^{-2} \dfrac{k_B T}{|c_1|n}, & T > 0. & \text{(6.49b)} \end{cases}
$$

In the BA phase, the f_x magnetization breaks the continuous SO(2) axial spin symmetry about z, and $\hat{f}_y$ fluctuations act to restore the broken symmetry. The $T = 0$ $\hat{f}_y$ structure factor in Eq. (6.46a) can be integrated in 2D to get convergent results, but for finite temperature the fluctuation integral diverges for $k \to 0$ (the limit of an infinite system). This is not surprising, because breaking a continuous symmetry is forbidden at finite temperature in an infinite 2D system [74, 75]. This issue also occurs for the BEC phase transition, which breaks global U(1) phase symmetry and results in divergent phase fluctuations which destroy the condensate order. In practise BEC theory is only applicable in a finite 2D system of size L_{sys} at sufficiently low temperature that the phase coherence length is $\gtrsim L_{\text{sys}}$ [80]. In a similar manner, finite-temperature $\hat{F}_{y,\sigma}$ fluctuations explicitly depend on L_{sys}.

Applying the results in Appendix B to the $T = 0$ structure factor in Eq. (6.46a), we find that the (convergent) quantum large-cell limits are given by

$$
\frac{\Delta \hat{F}_{y,\sigma}^2}{N_\sigma} \approx \frac{2R}{\tilde{\xi}_Q} \times \begin{cases} \dfrac{8}{3\pi}, & \text{Cylindrical cells,} & \text{(6.50a)} \\[4mm] \sqrt{\dfrac{\pi}{2}}, & \text{Gaussian cells.} & \text{(6.50b)} \end{cases}
$$

In contrast, as expected, the thermodynamic limits of the $\hat{F}_{y,\sigma}$ fluctuations are divergent. To handle this divergence, following the results in Appendix B applied to

Eq. (6.46b), we restrict ourselves to a finite system of size $L_{\text{sys}} \equiv R/\kappa$ for $\kappa \ll 1$, i.e. a low k cutoff $k_{\min} \equiv 1/L_{\text{sys}}$. The fluctuations then converge to give us the thermodynamic limits

$$\frac{\Delta \hat{F}_{y,\sigma}^2}{N_\sigma} \approx \frac{2R^2}{\tilde{\xi}_E^2} \left(\frac{k_B T}{|c_1|n} \right) \times \begin{cases} \ln\left(\dfrac{2}{\kappa}\right) + \dfrac{1}{4} - \gamma_e, & \text{Cylindrical cells,} \qquad (6.51a) \\[2mm] \ln\left(\dfrac{2}{\kappa^2}\right) - \gamma_e, & \text{Gaussian cells.} \qquad (6.51b) \end{cases}$$

We now present numerical results for $\hat{F}_{y,\sigma}$ fluctuations in the BA phase, along with the analytic limits just derived. In Fig. 6.16 fluctuations are shown as a function of temperature, and in Fig. 6.17 as a function of cell size R. A cutoff of $k_{\min} = 10^{-2}/\xi_s$ (i.e. $L_{\text{sys}} = 10^2 \xi_s$) has been used to get finite fluctuations at high temperatures. The analysis of the $\hat{F}_{y,\sigma}$ fluctuations has some similarities with that done in the F phase for $\hat{N}_\sigma$ and $\hat{F}_{z,\sigma}$ fluctuations, but with important differences due to the diverging $\hat{f}_y$ structure factor.

Only the ungapped $\nu = 1$ magnon mode contributes to the $\hat{F}_{y,\sigma}$ fluctuations, and it has an associated length scale [see Sec. 5.5]

$$\xi_q = \hbar/\sqrt{Mq} = 7.08 \,\mu\text{m}, \qquad (6.52)$$

and for our parameters is equal to the spin healing length ξ_s. The relevant length scales for the fluctuations are the cell size R, the thermal wavelength defined in relation to the $\nu = 1$ spectrum

$$E_1^{BA} \left(\frac{1}{\lambda_{th}} \right) \equiv k_B T, \qquad (6.53)$$

and the lengths $\tilde{\xi}_Q$ and $\tilde{\xi}_E$ as defined in Eqs. (6.47) and (6.48), which for our parameters are

$$\tilde{\xi}_Q = 13.4 \,\mu\text{m}, \qquad (6.54)$$

$$\tilde{\xi}_E = 8.18 \,\mu\text{m}. \qquad (6.55)$$

Analogous to the F phase, for $k_B T < q$, λ_{th} is the thermal phonon wavelength while for $k_B T > q$ it is proportional to the usual thermal de-Broglie wavelength.

For $R \ll \{\lambda_{th}, \tilde{\xi}_Q, \tilde{\xi}_E\}$, we go to the quantum small-cell limit as we see in Fig. 6.17 (a) and (b). As T increases to the point where λ_{th} is comparable to or smaller than R, the relevant modes become thermally occupied and fluctuations increase, as we see in Fig. 6.16 (a) and (b). In the high T regime, $\lambda_{th} \ll R$ and the fluctuations increase linearly with T, but with an additional R^2 dependence from the diverging structure factor. This non-extensive scaling is clearly seen in the slope of the $T > 0$ lines in Fig. 6.17 (a) and (b).

With reference to the $T = 5$ nK and $T = 50$ nK lines on Fig. 6.17 (a) and (c), we see that for any non-zero temperature we can get to a regime where R is larger than all other length scales and fluctuations are dominated by thermal modes, thus reaching the thermodynamic limit.

In the case of zero-temperature, for $R \sim \tilde{\xi}_Q$ we sample the linearly diverging structure factor, and we get non-extensive scaling with fluctuations increasing linearly with increasing R, as we see with the $T = 0$ solid blue line in Figs. 6.17 (a) and (b).

Comparing cylindrical and gaussian cell subplots in Figs. 6.16 and 6.17, we see that they have qualitatively the same fluctuation behaviour. The differences are barely noticeable on a log scale. At large R, cylindrical cells have a slightly smaller scaling coefficient than gaussian cells due to the first peak of the geometry function being relatively smaller, so they scale the divergence differently [as seen in Eqs. (6.50a)-(6.51b)].
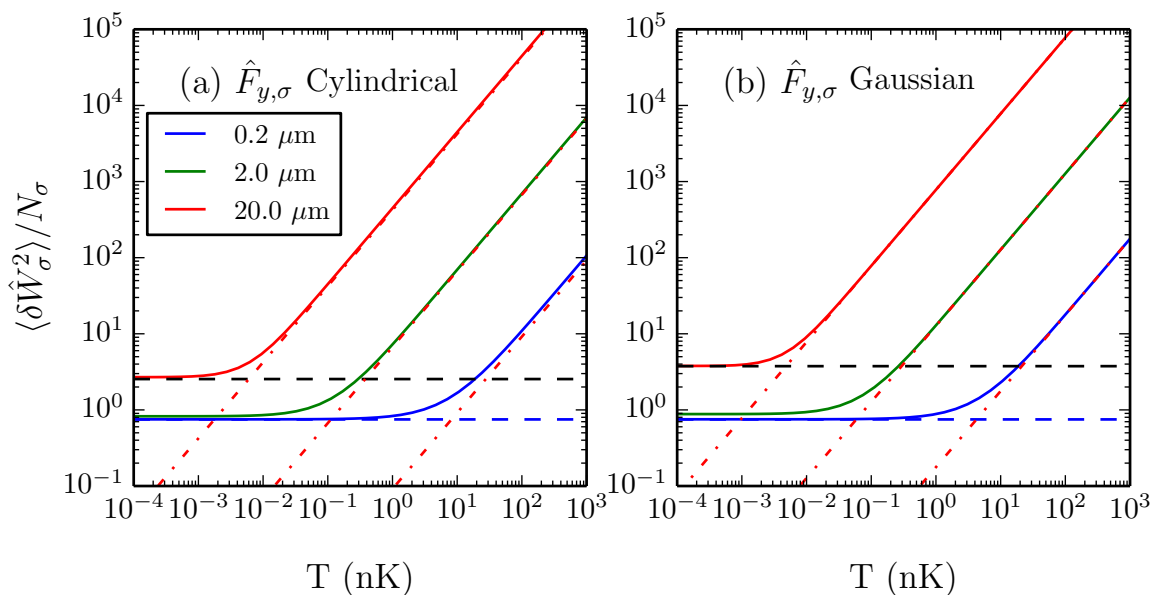

Figure 6.16: $\hat{F}_{y,\sigma}$ cell fluctuations in the BA phase as a function of temperature. For cell sizes $R \in \{0.2, 2, 20\}\mu$m, as labelled in (a). Also plotted are the quantum small cell limit (dashed blue line), quantum large cell limit (dashed black line) and thermodynamic limit (dot-dashed red lines). Parameters as in Fig. (6.12), with $k_{\min} = 10^{-2}\xi_s$ (see text).

Figure 6.17: $\hat{F}_{y,\sigma}$ cell fluctuations in the BA phase as a function of cell size R. At temperatures $T \in \{0, 5, 50\}$nK, as labelled in (a). Also plotted are the quantum small cell limit (dashed blue line), quantum large cell limit (dashed black line) and thermodynamic limit (dot-dashed red lines). Parameters as in Fig. (6.12), with $k_{\min} = 10^{-2}\xi_s$ (see text).
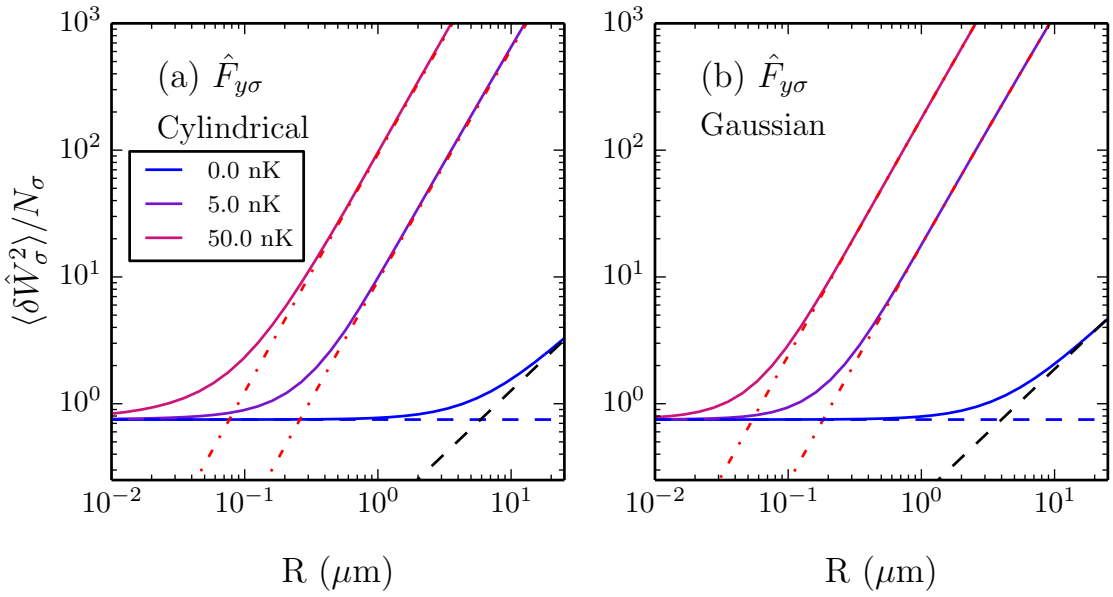
Chapter 7

Discussion and Conclusions

7.1   Density Fluctuations

In this thesis we have developed a formalism for the static structure factor of a uniform spin-1 condensate subject to constant linear and quadratic Zeeman shifts. Our results are based on the Bogoliubov formalism and are accurate to the leading order term proportional to the condensate density. The static structure factors are an important tool in quantifying fluctuations for scalar and binary systems (e.g. see [77–79, 81]), and this work is important for extending such results to the spinor system.

A feature of spinor condensates is that additional continuous symmetries can be broken, leading to new Nambu-Goldstone modes, as is predicted to occur for the AF and BA phases. For the AF phase we found that the asymmetry in the nematic order of the condensate was revealed through the f_x and f_y fluctuations. In the BA phase we observed a divergence in the f_y fluctuations, associated with the spontaneous development of a transverse (axial-symmetry-breaking) magnetization. Our results show that this divergence arises from the Nambu-Goldstone magnon mode. Interestingly, such a divergence in fluctuations was not observed in our results for the AF phase, which also has a Nambu-Goldstone magnon branch [$\nu = 1$ in Fig. 5.10]. The reason is that for the AF phase the broken symmetry manifests only in the nematic order of the condensate, not in the spin order. Indeed, an immediate extension of our theory is to assess fluctuations of the nematic density,

$$\hat{q}_{\alpha\beta}(\mathbf{x}) = \hat{\boldsymbol{\psi}}^{\dagger}(\mathbf{x})Q_{\alpha\beta}\hat{\boldsymbol{\psi}}(\mathbf{x}), \tag{7.1}$$

as a generalisation of Eq. (2.30). We find that for the AF state the fluctuations in q_{xy} diverge for $k \to 0$ due to both the phonon and magnon modes, with the magnon branch

dominating. Because some of the techniques used to image the spin density are also sensitive to the nematic density (e.g. see [29]), the measurement of such fluctuations may also be possible in experiments.

7.2   Fluctuations measured in cells

We have applied our fluctuation formalism to the experimentally realistic situation of measuring fluctuations within finite cells, considering the two limits of hard-edged cylindrical and soft-edged gaussian cells. Our analytic limiting results come from approximate integrals of the relevant structure factors, and our numerical analysis has shown the relevant regimes of validity for the small cell quantum limit and the large cell quantum and thermodynamic limits.

For operators with structure factors similar to those of equivalent scalar systems, our results for cylindrical cells are in agreement with the work done in Ref. [78] for a scalar system. The extension from scalar systems to a spin-1 system required creating model structure factors for certain spin-density operators in order to perform analytic integrals. Numerically verifying these analytic results required care in the case of cylindrical cells due to the slow decay of the structure factor at high k, and in general gaussian cells fluctuation integrals are much faster to converge numerically. Physically, measurements will be a convolution of these two shapes, and experimental results are expected to be between the bounds of the cylindrical and gaussian results.

7.3   Application to experiment

Our analysis here has been for a uniform system, and several factors will become important in applying these results to the experimental regime. First, external trapping potentials cause the total density of the condensate to vary spatially and a full treatment of the trapped system would require a large-scale numerical solution of the Gross-Pitaevskii equation for the condensate and of the Bogoliubov-de Gennes equations for the quasiparticles. However, our analysis can be applied to this situation using the local density approximation, i.e. we consider the gas to be homogeneous at each point in space using the local value of the condensate density. A discussion of the local density approximation in relation to the density response of a scalar condensate is presented in Ref. [46]. Second, in our analysis of the AF and BA phases we have assumed that the axisymmetry is broken uniformly over the entire system. For the case where

the system forms domains of local broken axisymmetry our analysis will only apply to each domain (also see discussion in [72]).

7.4 Outlook

We hope that this work will motivate future experiments to investigate the fluctuations of the spin-1 system. The different scaling that emerges in the low-temperature regime is a clear signal of the quantum and spinor nature of the spin-1 Bose condensate. There are a variety of potential future research directions that are opened up by the work in this thesis. There are more operators than just total and spin density available; as already mentioned, nematic density operators already reveal interesting extra information. Within the spin-1 system there are many more phenomena that are still poorly understood and ripe for theoretical illumination. Current spin-1 systems have a magnetic dipole moment, which we have neglected in this thesis but has been shown to have a detectable effect in spin-1 ^{87}Rb systems [39, 82].

Appendix A

Quasi-2D spinor condensate

Here we detail how to apply our formalism for the uniform spin-1 condensate to a trapped system in the quasi-2D regime, where the z direction is frozen in the ground-state of a harmonic trap. We show that the effect of the confining z-trap is to scale the interaction parameters and shift the chemical potential by the trap energy.

Our formalism goes beyond the mean-field approach to analyze the fluctuations of the condensate, so we also show that moving to quasi-2D involves the same Bogoliubov quasiparticle modes as for the 3D case, which means we can apply our spin-1 Bogoliubov theory to the quasi-2D system.

Finally, we consider a system with a weak in-plane harmonic trap, which is what experiments can actually achieve. We show it can be adequately described (close to the centre of the trap) by our formalism for the uniform system, by using a density equal to the peak density of the in-plane harmonic trap.

A.1 Uniform, trapped in z

A.1.1 Condensate

The quasi-2D regime is realised by harmonic confinement of angular frequency ω_z in the z direction, i.e. a trapping potential

$$V(z) = \frac{1}{2}M\omega_z^2 z^2, \tag{A.1}$$

with length scale

$$l_z = \sqrt{\hbar/M\omega_z}. \tag{A.2}$$

Appendix A. Quasi-2D spinor condensate

We assume that the trap is sufficiently tight such that the thermal and interaction energy scales are less than $\hbar\omega_z$ so that the system is in the harmonic oscillator ground state in the z direction and we don't have to account for excited z-modes.

In this case, we can write the 3-dimensional condensate wave function as

$$\boldsymbol{\psi}(\mathbf{x}) = \sqrt{n}\,\boldsymbol{\xi}\chi(z), \tag{A.3}$$

where n is the areal density and $\chi(z)$ is the harmonic oscillator ground state given by

$$\chi(z) \equiv \frac{1}{(\pi l_z^2)^{1/4}} \exp\left(-\frac{z^2}{2l_z^2}\right). \tag{A.4}$$

We can write the spinor GPE

$$\mu\boldsymbol{\psi}(\mathbf{x}) = \left[h_0 + \frac{1}{2}M\omega_z^2 z^2 + c_0\boldsymbol{\psi}^\dagger(\mathbf{x})\boldsymbol{\psi}(\mathbf{x})\mathbb{1} + c_1\sum_\alpha \left[\boldsymbol{\psi}^\dagger(\mathbf{x})\mathrm{F}_\alpha\boldsymbol{\psi}(\mathbf{x})\right]\mathrm{F}_\alpha\right]\boldsymbol{\psi}(\mathbf{x}), \tag{A.5}$$

where $\mathbb{1}$ is the 3×3 identity matrix. We can project $\boldsymbol{\psi}^\dagger(\mathbf{x})$ onto this, substitute in Eq. (A.3), and integrate over z (from $-\infty$ to ∞), i.e.

$$\mu = \int \left(\chi^*(z)\boldsymbol{\xi}^\dagger h_0\boldsymbol{\xi}\chi(z) + \frac{1}{2}M\omega_z^2 z^2|\chi(z)|^2 + \left[c_0 n + c_1|\mathbf{f}|^2\right]|\chi(z)|^4\right)dz, \tag{A.6}$$

since $\boldsymbol{\xi}^\dagger\boldsymbol{\xi} = 1$ and $\int |\chi(z)|^2\,dz = 1$. The first term on the R.H.S is

$$\int \left[\chi^*(z)\boldsymbol{\xi}^\dagger h_0\boldsymbol{\xi}\chi(z)\right]dz = \left[\int \chi^*(z)\frac{-\hbar^2}{2M}\frac{\partial^2}{\partial z^2}\chi(z)\,dz\right] - p\boldsymbol{\xi}^\dagger\mathrm{F}_z\boldsymbol{\xi} + q\boldsymbol{\xi}^\dagger\mathrm{F}_z^2\boldsymbol{\xi} \tag{A.7}$$

$$= \frac{1}{4}\hbar\omega_z - pf_z/n + q(1 - |\xi_0|^2). \tag{A.8}$$

The second term (z trap potential) is

$$\frac{1}{2}m\omega_z^2 \int z^2|\chi(z)|^2\,dz = \frac{1}{4}\hbar\omega_z. \tag{A.9}$$

The last term is

$$\left[c_0 n + c_1|\mathbf{f}|^2\right]\int |\chi(x)|^4\,dz = \frac{[c_0 n + c_1|\mathbf{f}|^2]}{\sqrt{2\pi}l_z}. \tag{A.10}$$

We can then define effective 2D interaction parameters

$$\tilde{c}_0 = \frac{c_0}{\sqrt{2\pi}l_z}, \quad \tilde{c}_1 = \frac{c_1}{\sqrt{2\pi}l_z}. \tag{A.11}$$

Thus we get

$$\tilde{\mu} = -pf_z/n + q(1 - |\xi_0|^2) + \tilde{c}_0 n + \tilde{c}_1|\mathbf{f}|^2, \tag{A.12}$$

where

$$\tilde{\mu} \equiv \mu - \frac{1}{2}\hbar\omega_z. \tag{A.13}$$

This matches our general μ defined in Eq. (3.11), after making the replacements $\tilde{c}_0 \to c_0$, $\tilde{c}_1 \to c_1$, $\tilde{\mu} \to \mu$. Thus we can apply our formalism for the uniform spin-1 condensate by using these effective interaction parameters and modified chemical potential.

A.1.2 Excitations

Here we show that we can treat the excitations in the quasi-2D system with our formalism for the uniform 3D system by integrating out the z direction and using effective interaction parameters.

For the uniform system harmonically trapped in the z direction, we assume that the z direction is so strongly trapped that the only excitations to appear are in-plane, with the z direction frozen in the harmonic oscillator ground state. In this case, the non-condensate operator becomes

$$\hat{\boldsymbol{\delta}}(\mathbf{x}) = \sum_{\mathbf{k}_\rho \neq \mathbf{0}, \nu} (\mathbf{u}_{\mathbf{k}_\rho \nu}(z) \hat{\alpha}_{\mathbf{k}_\rho \nu} + \mathbf{v}^*_{\mathbf{k}_\rho \nu}(z) \hat{\alpha}^\dagger_{-\mathbf{k}_\rho \nu}) \frac{e^{i\mathbf{k}_\rho \cdot \boldsymbol{\rho}}}{\sqrt{V}}. \tag{A.14}$$

Using Eq. (A.3) for the condensate, and adding a harmonic potential of the form given in Eq. (A.1), the resulting Bogoliubov Hamiltonian is the same as the one derived in Sec 3.1, but with effective interaction parameters $c_0 \to \tilde{c}_0$ and $c_1 \to \tilde{c}_1$ as defined in Eq. (A.11), a shifted chemical potential $\tilde{\mu}$ [as defined in Eq. (A.13)], and n being the in-plane areal density.

For the quasiparticle amplitudes, let us assume that they have the same z-dependence as the condensate, i.e.

$$\mathbf{u}_{\mathbf{k}_\rho, \nu}(z) = \mathbf{u}_{\mathbf{k}_\rho, \nu} \chi(z), \tag{A.15}$$

$$\mathbf{v}_{\mathbf{k}_\rho, \nu}(z) = \mathbf{v}_{\mathbf{k}_\rho, \nu} \chi(z), \tag{A.16}$$

where $\chi(z)$ is the harmonic oscillator ground state given by Eq. (A.4). Then the Bogoliubov de-Gennes equations become

$$\chi(z) \sigma_z M^B_{\mathbf{k}} \begin{pmatrix} \mathbf{u}_{\mathbf{k}_\rho, \nu} \\ \mathbf{v}_{\mathbf{k}_\rho, \nu} \end{pmatrix} = \chi(z) E_{\mathbf{k}\nu} \begin{pmatrix} \mathbf{u}_{\mathbf{k}_\rho, \nu} \\ \mathbf{v}_{\mathbf{k}_\rho, \nu} \end{pmatrix}. \tag{A.17}$$

We can then project out the z-dependence by multiplying Eq. (A.17) by $\chi^*(z)$ and integrating over z (from $-\infty$ to ∞). This gives us effectively the same Bogoliubov de-Gennes equations as Eq. (3.24), with $\mathbf{k} \to \mathbf{k}_\rho$.

Thus we can use our formalism for the uniform system to describe the collective excitations of the uniform quasi-2D system by using effective interaction parameters, a shifted chemical potential, and the in-plane density.

A.2 Trapped in 2-D

We would like to use our formalism for the uniform system on a quasi-2D system with N atoms inside a weak, cylindrically symmetric harmonic trap in the radial direction given by

$$V(\boldsymbol{\rho}) = \frac{1}{2} M \omega_\rho^2 \rho^2, \tag{A.18}$$

where $\rho \equiv \sqrt{x^2 + y^2}$. Let us consider a region close to the centre of the trap where the density is approximately uniform and thus our formalism can be applied. In this region, we can approximate the density as the peak density at the centre. For the case where $c_0 \gg c_1$, i.e. the density interaction energy dominates all other effects, and if we neglect kinetic energy [the Thomas-Fermi (TF) approximation] then a similar approach to Sec. A.1 gives us

$$n_{TF}(\boldsymbol{\rho}) \approx \frac{\tilde{\mu} - V(\boldsymbol{\rho})}{\tilde{c}_0}, \tag{A.19}$$

where $\tilde{\mu}$ is the chemical potential that fixes N in our trapped system, defined in Eq. (A.13). Our system extends to the Thomas-Fermi radius, given by

$$R_{TF}^2 = \frac{2\tilde{\mu}}{M \omega_\rho^2}. \tag{A.20}$$

Using these we can relate $\tilde{\mu}$ to N by carrying out the integral

$$N = \int_0^{R_{TF}} 2\pi \rho \, n_{TF}(\boldsymbol{\rho}) \, \mathrm{d}\rho = \frac{\pi \tilde{\mu}^2}{M \tilde{c}_0 \omega_\rho^2}, \tag{A.21}$$

and thus we have

$$\tilde{\mu} = \sqrt{\frac{\tilde{c}_0 N M \omega_\rho^2}{\pi}}. \tag{A.22}$$

Therefore, using effective interaction parameters as in Eq. (A.11) and the peak density

$$n_{\mathrm{peak}} = \frac{\tilde{\mu}}{\tilde{c}_0}, \tag{A.23}$$

we can apply our general mean-field formalism of Chapter 2 to a harmonic pancake trapped quasi-2D system.

Appendix B

Cell fluctuation integrals

If $S_w(k) = a$, then regardless of cell shape we get

$$\Delta W_\sigma^2 = n \int \frac{d^D \mathbf{k}}{(2\pi)^D} S_w(\mathbf{k}) \tilde{\tau}_\sigma(\mathbf{k}) = an\tau_\sigma(\mathbf{0}) = aN_\sigma, \qquad \text{(B.1)}$$

because the weight function is normalized according to Eq. (6.11).

We now specialize to cell-specific results for the case of $R \to \infty$ with $S_w(k) \to ak^n$ as $k \to 0$, where the system size is R/κ (i.e. the k integral starts at κ/R). We use these results to generate the large R fluctuation limit for all our structure factor limits by summing each contribution of the k power series.

B.1   Cylindrical cells

$$\frac{R^n \Delta W_\sigma^2}{aN_\sigma} \to 2R^n \int_{\kappa/R}^\infty dk\, k^{n+1} [J_1(kR)/k]^2 \qquad \text{(B.2)}$$

$$= \begin{cases} \frac{1}{2}\left[\ln(2/\kappa) + \frac{1}{4} - \gamma_e\right] & n = -2 \\ \frac{8}{3\pi} - \frac{\kappa}{2} & n = -1 + \mathrm{O}\left(\kappa^{n+4}\right), \\ 1 - \frac{1}{4}\kappa^2 & n = 0 \end{cases} \qquad \text{(B.3)}$$

where the Euler-gamma constant is

$$\gamma_e \approx 0.5772. \qquad \text{(B.4)}$$

For $n \in \{0, -1\}$ we can take the limit of $\kappa \to 0$ (i.e. an infinite system), but $n = 2$ is divergent. For $n > 0$, we construct model structure factors that we can integrate, since the Bessel function makes integrating the full structure factors problematic.

B.2 Gaussian cells

$$
\frac{R^n \Delta W_\sigma^2}{a N_\sigma} \rightarrow
\begin{cases}
\frac{1}{2}\left[\ln(2/\kappa^2) - \gamma_e\right] + \mathrm{O}\left(\kappa^{n+4}\right) & n = -2 \\
2^{n/2}\Gamma(n/2 + 1) - \frac{\kappa^{n+2}}{n+2} + \mathrm{O}\left(\kappa^{n+4}\right) & n \neq -2
\end{cases}
\tag{B.5}
$$

$$
=
\begin{cases}
\frac{1}{2}\left[\ln(2/\kappa^2) - \gamma_e\right] & n = -2 \\
\sqrt{\frac{\pi}{2}} - \kappa & n = -1 \\
1 - \frac{1}{2}\kappa^2 & n = 0 \\
\sqrt{\frac{\pi}{2}} - \frac{1}{3}\kappa^3 & n = 1 \\
2 - \frac{1}{4}\kappa^4 & n = 2
\end{cases}
\quad + \mathrm{O}\left(\kappa^{n+4}\right),
\tag{B.6}
$$

where γ_e is defined in Eq. (B.4). For $n > -2$ we can take $\kappa \to 0$ (i.e. an infinite system), but $n \leq -2$ is divergent.

Bibliography

[1] S. Bose. *Planck's law and the light quantum hypothesis.* Z. Phys **26**, 178 (1924).

[2] A. Einstein. *Quantum theory of the monoatomic ideal gas.* Sitzungsberichte der Preussischen Akademie der Wissenschaften, Physikalischmathematische Klasse 261–267 (1924).

[3] M. H. Anderson, J. R. Ensher, M. R. Matthews, C. E. Wieman, and E. A. Cornell. *Observation of Bose-Einstein condensation in a dilute atomic vapor.* Science **269**, 198 (1995).

[4] K. B. Davis, M. O. Mewes, M. R. Andrews, N. J. van Druten, D. S. Durfee, D. M. Kurn, and W. Ketterle. *Bose-Einstein condensation in a gas of sodium atoms.* Phys. Rev. Lett. **75**, 3969 (1995).

[5] C. C. Bradley, C. A. Sackett, J. J. Tollett, and R. G. Hulet. *Evidence of Bose-Einstein condensation in an atomic gas with attractive interactions.* Phys. Rev. Lett. **75**, 1687 (1995).

[6] A. Griesmaier, J. Werner, S. Hensler, J. Stuhler, and T. Pfau. *Bose-Einstein condensation of chromium.* Phys. Rev. Lett. **94**, 160401 (2005).

[7] M. Lu, N. Q. Burdick, S. H. Youn, and B. L. Lev. *Strongly dipolar Bose-Einstein condensate of dysprosium.* Phys. Rev. Lett. **107**, 190401 (2011).

[8] M. Lu, N. Q. Burdick, and B. L. Lev. *Quantum degenerate dipolar fermi gas.* Phys. Rev. Lett. **108**, 215301 (2012).

[9] K. Aikawa, A. Frisch, M. Mark, S. Baier, A. Rietzler, R. Grimm, and F. Ferlaino. *Bose-Einstein condensation of erbium.* Phys. Rev. Lett. **108**, 210401 (2012).

Bibliography

[10] D. M. Stamper-Kurn, M. R. Andrews, A. P. Chikkatur, S. Inouye, H.-J. Miesner, J. Stenger, and W. Ketterle. *Optical confinement of a Bose-Einstein condensate.* Phys. Rev. Lett. **80**, 2027 (1998).

[11] A. Görlitz, T. L. Gustavson, A. E. Leanhardt, R. Löw, A. P. Chikkatur, S. Gupta, S. Inouye, D. E. Pritchard, and W. Ketterle. *Sodium Bose-Einstein condensates in the $F = 2$ state in a large-volume optical trap.* Phys. Rev. Lett. **90**, 090401 (2003).

[12] M. D. Barrett, J. A. Sauer, and M. S. Chapman. *All-optical formation of an atomic Bose-Einstein condensate.* Phys. Rev. Lett. **87**, 010404 (2001).

[13] H. Schmaljohann, M. Erhard, J. Kronjäger, M. Kottke, S. van Staa, L. Cacciapuoti, J. J. Arlt, K. Bongs, and K. Sengstock. *Dynamics of $F = 2$ spinor Bose-Einstein condensates.* Phys. Rev. Lett. **92**, 040402 (2004).

[14] Q. Beaufils, R. Chicireanu, T. Zanon, B. Laburthe-Tolra, E. Maréchal, L. Vernac, J.-C. Keller, and O. Gorceix. *All-optical production of chromium Bose-Einstein condensates.* Phys. Rev. A **77**, 061601 (2008).

[15] D. G. Fried, T. C. Killian, L. Willmann, D. Landhuis, S. C. Moss, D. Kleppner, and T. J. Greytak. *Bose-Einstein condensation of atomic hydrogen.* Phys. Rev. Lett. **81**, 3811 (1998).

[16] S. L. Cornish, N. R. Claussen, J. L. Roberts, E. A. Cornell, and C. E. Wieman. *Stable ^{85}Rb Bose-Einstein condensates with widely tunable interactions.* Phys. Rev. Lett. **85**, 1795 (2000).

[17] F. Pereira Dos Santos, J. Léonard, J. Wang, C. J. Barrelet, F. Perales, E. Rasel, C. S. Unnikrishnan, M. Leduc, and C. Cohen-Tannoudji. *Bose-Einstein condensation of metastable helium.* Phys. Rev. Lett. **86**, 3459 (2001).

[18] G. Modugno, G. Ferrari, G. Roati, R. J. Brecha, A. Simoni, and M. Inguscio. *Bose-Einstein condensation of potassium atoms by sympathetic cooling.* **294**, 1320 (2001).

[19] T. Weber, J. Herbig, M. Mark, H.-C. Nägerl, and R. Grimm. *Bose-Einstein condensation of cesium.* **299**, 232 (2003).

[20] Y. Takasu, K. Maki, K. Komori, T. Takano, K. Honda, M. Kumakura, T. Yabuzaki, and Y. Takahashi. *Spin-singlet Bose-Einstein condensation of two-electron atoms.* Phys. Rev. Lett. **91**, 040404 (2003).

[21] G. Roati, M. Zaccanti, C. D'Errico, J. Catani, M. Modugno, A. Simoni, M. Inguscio, and G. Modugno. ^{39}K *Bose-Einstein condensate with tunable interactions.* Phys. Rev. Lett. **99**, 010403 (2007).

[22] T. Fukuhara, S. Sugawa, and Y. Takahashi. *Bose-Einstein condensation of an ytterbium isotope.* Phys. Rev. A **76**, 051604 (2007).

[23] S. Kraft, F. Vogt, O. Appel, F. Riehle, and U. Sterr. *Bose-Einstein condensation of alkaline earth atoms:* $^{40}Ca.$ Phys. Rev. Lett. **103**, 130401 (2009).

[24] S. Stellmer, M. K. Tey, B. Huang, R. Grimm, and F. Schreck. *Bose-Einstein condensation of strontium.* Phys. Rev. Lett. **103**, 200401 (2009).

[25] Y. N. M. de Escobar, P. G. Mickelson, M. Yan, B. J. DeSalvo, S. B. Nagel, and T. C. Killian. *Bose-Einstein condensation of* $^{84}Sr.$ Phys. Rev. Lett. **103**, 200402 (2009).

[26] S. Stellmer, M. K. Tey, R. Grimm, and F. Schreck. *Bose-Einstein condensation of* $^{86}Sr.$ Phys. Rev. A **82**, 041602 (2010).

[27] P. G. Mickelson, Y. N. Martinez de Escobar, M. Yan, B. J. DeSalvo, and T. C. Killian. *Bose-Einstein condensation of* ^{88}Sr *through sympathetic cooling with* $^{87}Sr.$ Phys. Rev. A **81**, 051601 (2010).

[28] Y. Kawaguchi and M. Ueda. *Spinor Bose-Einstein condensates.* Physics Reports **520**, 253 (2012). ISSN 0370-1573.

[29] D. M. Stamper-Kurn and M. Ueda. *Spinor Bose gases: Symmetries, magnetism, and quantum dynamics.* Rev. Mod. Phys. **85**, 1191 (2013).

[30] D. A. Steck. *Sodium D line data.* (2010). Revision 2.1.4, Date accessed: 25 June 2014. URL http://steck.us/alkalidata.

[31] D. A. Steck. *Rubidium 87 D line data.* (2010). Revision 2.1.4, Date accessed: 25 June 2014. URL http://steck.us/alkalidata.

[32] T.-L. Ho. *Spinor Bose condensates in optical traps.* Phys. Rev. Lett. **81**, 742 (1998).

[33] T. Ohmi and K. Machida. *Bose-Einstein condensation with internal degrees of freedom in alkali atom gases.* J. Phys. Soc. Jpn **67**, 1822 (1998).

[34] J. Stenger, S. Inouye, D. M. Stamper-Kurn, H.-J. Miesner, A. P. Chikkatur, and W. Ketterle. *Spin domains in ground-state Bose-Einstein condensates.* Nature **396**, 345 (1999).

[35] M.-S. Chang, C. D. Hamley, M. D. Barrett, J. A. Sauer, K. M. Fortier, W. Zhang, L. You, and M. S. Chapman. *Observation of spinor dynamics in optically trapped ^{87}Rb Bose-Einstein condensates.* Phys. Rev. Lett. **92**, 140403 (2004).

[36] M.-S. Chang, Q. Qin, W. Zhang, L. You, and M. S. Chapman. *Coherent spinor dynamics in a spin-1 Bose condensate.* Nat. Phys. **1**, 111 (2005).

[37] A. T. Black, E. Gomez, L. D. Turner, S. Jung, and P. D. Lett. *Spinor dynamics in an antiferromagnetic spin-1 condensate.* Phys. Rev. Lett. **99**, 070403 (2007).

[38] M. Vengalattore, S. R. Leslie, J. Guzman, and D. M. Stamper-Kurn. *Spontaneously modulated spin textures in a dipolar spinor Bose-Einstein condensate.* Phys. Rev. Lett. **100**, 170403 (2008).

[39] M. Vengalattore, J. Guzman, S. R. Leslie, F. Serwane, and D. M. Stamper-Kurn. *Periodic spin textures in a degenerate $F = 1$ ^{87}Rb spinor Bose gas.* Phys. Rev. A **81**, 053612 (2010).

[40] Y. Liu, E. Gomez, S. E. Maxwell, L. D. Turner, E. Tiesinga, and P. D. Lett. *Number fluctuations and energy dissipation in sodium spinor condensates.* Phys. Rev. Lett. **102**, 225301 (2009).

[41] L. E. Sadler, J. M. Higbie, S. R. Leslie, M. Vengalattore, and D. M. Stamper-Kurn. *Spontaneous symmetry breaking in a quenched ferromagnetic spinor boseÐeinstein condensate.* Nature **443**, 312 (2006).

[42] Y. Liu, S. Jung, S. E. Maxwell, L. D. Turner, E. Tiesinga, and P. D. Lett. *Quantum phase transitions and continuous observation of spinor dynamics in an antiferromagnetic condensate.* Phys. Rev. Lett. **102**, 125301 (2009).

[43] C.-L. Hung, X. Zhang, L.-C. Ha, S.-K. Tung, N. Gemelke, and C. Chin. *Extracting density-density correlations from in situ images of atomic quantum gases.* New J. Phys. **13**, 075019 (2011).

[44] T. Jacqmin, J. Armijo, T. Berrada, K. V. Kheruntsyan, and I. Bouchoule. *Sub-poissonian fluctuations in a 1d Bose gas: From the quantum quasicondensate to the strongly interacting regime.* Phys. Rev. Lett. **106**, 230405 (2011).

[45] J. Armijo. *Direct observation of quantum phonon fluctuations in a one-dimensional Bose gas.* Phys. Rev. Lett. **108**, 225306 (2012).

[46] F. Zambelli, L. Pitaevskii, D. M. Stamper-Kurn, and S. Stringari. *Dynamic structure factor and momentum distribution of a trapped Bose gas.* Phys. Rev. A **61**, 063608 (2000).

[47] M.-C. Chung and A. B. Bhattacherjee. *Dynamical structure factor and spin-density separation for a weakly interacting two-component Bose gas.* Phys. Rev. Lett. **101**, 070402 (2008).

[48] M. Abad and A. Recati. *A study of coherently coupled two-component Bose-Einstein condensates.* Eur. Phys. J. D **67**, 148 (2013).

[49] R. Barnett, A. Polkovnikov, and M. Vengalattore. *Prethermalization in quenched spinor condensates.* Phys. Rev. A **84**, 023606 (2011).

[50] C.-L. Hung, X. Zhang, N. Gemelke, and C. Chin. *Observation of scale invariance and universality in two-dimensional Bose gases.* Nature **470**, 236 (2011).

[51] A. Blumkin, S. Rinott, R. Schley, A. Berkovitz, I. Shammass, and J. Steinhauer. *Observing atom bunching by the Fourier slice theorem.* Phys. Rev. Lett. **110**, 265301 (2013).

[52] A. G. Sykes and R. J. Ballagh. *Probing the quantum state of a 1D Bose gas using off-resonant light scattering.* Phys. Rev. Lett. **107**, 270403 (2011).

[53] J. Steinhauer, R. Ozeri, N. Katz, and N. Davidson. *Excitation spectrum of a Bose-Einstein condensate.* Phys. Rev. Lett. **88**, 120407 (2002).

[54] E. D. Kuhnle, H. Hu, X.-J. Liu, P. Dyke, M. Mark, P. D. Drummond, P. Hannaford, and C. J. Vale. *Universal behavior of pair correlations in a strongly interacting fermi gas.* Phys. Rev. Lett. **105**, 070402 (2010).

[55] S. Hoinka, M. Lingham, M. Delehaye, and C. J. Vale. *Dynamic spin response of a strongly interacting fermi gas.* Phys. Rev. Lett. **109**, 050403 (2012).

[56] C. Sanner, E. J. Su, A. Keshet, W. Huang, J. Gillen, R. Gommers, and W. Ketterle. *Speckle imaging of spin fluctuations in a strongly interacting fermi gas.* Phys. Rev. Lett. **106**, 010402 (2011).

[57] J. Guzman, G.-B. Jo, A. N. Wenz, K. W. Murch, C. K. Thomas, and D. M. Stamper-Kurn. *Long-time-scale dynamics of spin textures in a degenerate $F = 1$ ^{87}Rb spinor Bose gas.* Phys. Rev. A **84**, 063625 (2011).

[58] E. M. Bookjans, C. D. Hamley, and M. S. Chapman. *Strong quantum spin correlations observed in atomic spin mixing.* Phys. Rev. Lett. **107**, 210406 (2011).

[59] C. D. Hamley, C. S. Gerving, T. M. Hoang, E. M. Bookjans, and M. S. Chapman. *Spin-nematic squeezed vacuum in a quantum gas.* Nature Physics **8**, 305 (2012).

[60] A. Tokuno and S. Uchino. *Magnetic resonance spectroscopy and characterization of magnetic phases for spinor Bose-Einstein condensates.* Phys. Rev. A **87**, 061604 (2013).

[61] B. Lücke, M. Scherer, J. Kruse, L. Pezzé, F. Deuretzbacher, P. Hyllus, O. Topic, J. Peise, W. Ertmer, J. Arlt, et al.. *Twin matter waves for interferometry beyond the classical limit.* Science **334**, 773 (2011).

[62] A. Vinit, E. M. Bookjans, C. A. R. Sá de Melo, and C. Raman. *Antiferromagnetic spatial ordering in a quenched one-dimensional spinor gas.* Phys. Rev. Lett. **110**, 165301 (2013).

[63] I. Carusotto and E. J. Mueller. *Imaging of spinor gases.* Journal of Physics B: Atomic, Molecular and Optical Physics **37**, S115 (2004).

[64] J. M. Higbie, L. E. Sadler, S. Inouye, A. P. Chikkatur, S. R. Leslie, K. L. Moore, V. Savalli, and D. M. Stamper-Kurn. *Direct nondestructive imaging of magnetization in a spin-1 Bose-Einstein gas.* Phys. Rev. Lett. **95**, 050401 (2005).

[65] K. Eckert, L. Zawitkowski, A. Sanpera, M. Lewenstein, and E. S. Polzik. *Quantum polarization spectroscopy of ultracold spinor gases.* Phys. Rev. Lett. **98**, 100404 (2007).

[66] S. Uchino, M. Kobayashi, and M. Ueda. *Bogoliubov theory and lee-huang-yang corrections in spin-1 and spin-2 Bose-Einstein condensates in the presence of the quadratic zeeman effect.* Phys. Rev. A **81**, 063632 (2010).

[67] L. M. Symes, D. Baillie, and P. B. Blakie. *Static structure factors for a spin-1 Bose-Einstein condensate.* Phys. Rev. A **89**, 053628 (2014).

[68] L. M. Symes, D. Baillie, and P. B. Blakie. *Fluctuations of spinor Bose-Einstein condensates.* ArXiv e-prints 1409.4513 (2014).

[69] F. Gerbier, A. Widera, S. Fölling, O. Mandel, and I. Bloch. *Resonant control of spin dynamics in ultracold quantum gases by microwave dressing.* Phys. Rev. A **73**, 041602 (2006).

[70] E. M. Bookjans, A. Vinit, and C. Raman. *Quantum phase transition in an antiferromagnetic spinor Bose-Einstein condensate.* Phys. Rev. Lett. **107**, 195306 (2011).

[71] D. R. Romano and E. J. V. de Passos. *Population and phase dynamics of $F = 1$ spinor condensates in an external magnetic field.* Physical Review A **70**, 043614 (2004).

[72] K. Murata, H. Saito, and M. Ueda. *Broken-axisymmetry phase of a spin-1 ferromagnetic Bose-Einstein condensate.* Phys. Rev. A **75**, 013607 (2007).

[73] E. Yukawa and M. Ueda. *Hydrodynamic description of spin-1 Bose-Einstein condensates.* Phys. Rev. A **86**, 063614 (2012).

[74] N. D. Mermin and H. Wagner. *Absence of ferromagnetism or antiferromagnetism in one- or two-dimensional isotropic heisenberg models.* Phys. Rev. Lett. **17**, 1133 (1966).

[75] P. C. Hohenberg. *Existence of long-range order in one and two dimensions.* Phys. Rev. **158**, 383 (1967).

[76] S. Giorgini, L. P. Pitaevskii, and S. Stringari. *Anomalous fluctuations of the condensate in interacting Bose gases.* Phys. Rev. Lett. **80**, 5040 (1998).

[77] G. E. Astrakharchik, R. Combescot, and L. P. Pitaevskii. *Fluctuations of the number of particles within a given volume in cold quantum gases.* Phys. Rev. A **76**, 063616 (2007).

[78] M. Klawunn, A. Recati, L. P. Pitaevskii, and S. Stringari. *Local atom-number fluctuations in quantum gases at finite temperature.* Phys. Rev. A **84**, 033612 (2011).

[79] R. N. Bisset and P. B. Blakie. *Fingerprinting rotons in a dipolar condensate: Super-poissonian peak in the atom-number fluctuations.* Phys. Rev. Lett. **110**, 265302 (2013).

[80] D. S. Petrov, M. Holzmann, and G. V. Shlyapnikov. *Bose-einstein condensation in quasi-2d trapped gases.* Phys. Rev. Lett. **84**, 2551 (2000).

[81] A. Recati and S. Stringari. *Spin fluctuations, susceptibility, and the dipole oscillation of a nearly ferromagnetic fermi gas.* Phys. Rev. Lett. **106**, 080402 (2011).

[82] G. E. Marti, A. MacRae, R. Olf, S. Lourette, F. Fang, and D. M. Stamper-Kurn. *Coherent magnon optics in a ferromagnetic spinor Bose-Einstein condensate.* ArXiv e-print 1404.5631 (2014).